Geodätisch-geophysikalische Arbeiten in der Schweiz

(Fortsetzung der Publikationsreihe
«Astronomisch-geodätische Arbeiten in der Schweiz»)

herausgegeben von der

Schweizerischen Geodätischen Kommission
(Organ der Akademie der Naturwissenschaften Schweiz)

Einhundertachter Band
Volume 108

GNSS/INS Kalman Filter Integrity Monitoring with Uncertain Time Correlated Error Processes

Omar García Crespillo

2022

Adresse der Schweizerischen Geodätischen Kommission:

ETH Zürich
Institut für Geodäsie und Photogrammetrie
Eidg. Technische Hochschule Zürich
8093 Zürich
Switzerland

Internet: http://www.sgc.ethz.ch

ISBN 978-3-908440-55-0

Redaktion des 108. Bandes:
Dr. O. García Crespillo, Dr. J. Skaloud, J. Müller-Gantenbein
Druck: Print-Atelier ADAG, Zürich

FOREWORD

The importance of reliable navigation goes hand in hand with the rise of systems operating (semi)autonomously in the air, on the road or on the water.
That translates to an urgency of correctly determining the level of trust of a navigation solution, especially that provided by the fusion of inertial and satellite observations. In aviation such measure of trust is related to an integrity, concept of which is applicable to a wide range of safety-critical application such as autonomous driving. Integrity is based on probabilistic measures that among other things account for imperfections in the predicted confidence levels in the estimated position. In turn, this is related to the shortcomings of observation stochastic models (e.g., noise of inertial, code or carrier-phase of GNSS signals, etc.). The dissertation of Omar García Crespillo offers a new view on how to deal with such "uncertainty of uncertainty" rigorously in the realm of an important class of time-correlated stochastic processes frequently used in the state-space estimators such as (Extended) Kalman Filters.

More particularly, special form of autoregressive processes such as Gauss Markov processes, or their linear combination, allow to capture complicated phenomena in sensor's behavior such as the noise encountered in oscillators or in inertial sensors of varying quality. The choice of model structure and its parameters is derived from the available information such as data or other knowledge that are both somewhat limited. Despite that, some newer methods of parameter identification allow quantifying such uncertainty precisely. However, how to reflect the uncertainty of stochastic parameters in the concept of "over-bounding" for the purpose of integrity was not completely clear for this type of processes. Although the presented work demonstrates how to correctly account for such uncertainty for one Gauss Markov process of the 1st order, the described path of analytical derivation can be extended for stochastic processes of a higher order, or their linear combination. In this perspective, the presented methodology is applicable beyond the exemplified case of INS/GNSS integration with inertial sensors of higher quality. As such, this study is filling an important gap of knowledge while having an immediate practical use within the integrated navigation.

The core of the dissertation has been published within several symposia of the Institute of Navigation (ION) and IEEE, such as ION-GNSS or PLANS, as well as in the well-respected ION journal of Navigation.

Prof. Dr. Jan Skaloud
EPF Lausanne
Thesis director

Prof. Dr. Markus Rothacher
ETH Zürich
President of SGK

PREFACE

L'importance d'une navigation fiable va de pair avec l'essor de systèmes fonctionnant de manière (semi-)autonome dans les airs, sur la route ou sur l'eau.
Cela se traduit par la nécessité de déterminer correctement le niveau de confiance de la solution de navigation, notamment celle obtenue par la fusion d'observations inertielles et satellitaires. Dans le domaine de l'aviation, cette mesure de confiance est liée à l'intégrité, dont le concept est applicable à un large éventail d'applications critiques pour la sécurité telles que la conduite autonome par exemple. Le concept d'intégrité est basé sur des mesures probabilistes qui, entre autres, tiennent compte des imperfections dans la prédiction des niveaux de confiance de la position estimée. Ces imperfections sont causées par des imprécisions dans les modèles d'erreurs stochastiques des observations (inertielles, de code, ou de phase des signaux GNSS, …).
La thèse d'Omar García Crespillo offre un nouveau point de vue sur la manière de traiter rigoureusement cette « incertitude de l'incertitude » dans le domaine d'une classe importante de processus stochastiques corrélés dans le temps et fréquemment utilisés dans les estimateurs tels que les filtres de Kalman (étendus).

Des variantes spéciales de processus autorégressifs tels que les processus de Gauss-Markov, ou des combinaisons linéaires de tels processus permettent de modéliser des phénomènes complexes dans le comportement des capteurs tels que le bruit dans les oscillateurs ou les capteurs inertiels. Le choix de la structure du modèle et de ses paramètres est dérivé d'informations disponibles telles que les données ou d'autres connaissances qui présentent souvent des incertitudes. Malgré cela, certaines méthodes d'identification des paramètres de processus stochastiques plus récent permettent de quantifier précisément cette incertitude. La manière de refléter l'incertitude des paramètres stochastiques dans le concept de « over-bounding » de l'estimation à des fins d'intégrité n'était cependant complètement claire pour ce type de processus. Bien que le travail présenté démontre comment tenir compte correctement d'une telle incertitude pour un processus de Markov de Gauss de 1er ordre, la procédure de dérivation analytique décrite dans cette thèse peut être étendue à des processus stochastiques d'ordre supérieur, ou à des combinaisons linéaires de tels processus. Dans cette perspective, la méthodologie présentée est applicable au-delà du cas étudié de l'intégration INS/GNSS avec des capteurs inertiels de qualité supérieure. En tant que telle, cette étude comble un manque important de connaissances tout en étant applicable en pratique dans le domaine de la navigation intégrée.

L'essentiel de la thèse a été publié dans plusieurs symposiums de l'Institute of Navigation (ION) et de l'IEEE, tels que ION-GNSS ou PLANS, ainsi que dans le très respecté journal ION de la navigation.

Prof. Dr. Jan Skaloud
EPF Lausanne
Directeur de thèse

Prof. Dr. Markus Rothacher
ETH Zürich
Président de la CGS

VORWORT

Die Bedeutung einer zuverlässigen Navigation geht Hand in Hand mit der Zunahme von (halb-)autonom operierenden Systemen in der Luft, auf der Straße oder auf dem Wasser.
Daraus ergibt sich die klare Notwendigkeit, den Grad der Zuverlässigkeit einer Navigationslösung korrekt zu bestimmen, insbesondere einer Lösung, die durch eine Kombination von Trägheits- und Satellitenbeobachtungen berechnet wird. In der Luftfahrt ist der Mass an Zuverlässigkeit mit dem Begriff Integrität verbunden, deren Konzept auf ein breites Spektrum sicherheitskritischer Anwendungen wie das autonome Fahren anwendbar ist. Die Integrität basiert auf probabilistischen Grössen, die unter anderem Unzulänglichkeiten in den vorhergesagten Zuverlässigkeitsniveaus der geschätzten Position berücksichtigen. Dies hängt wiederum mit den Unzulänglichkeiten stochastischer Beobachtungsmodelle zusammen (z.B. für die Trägheitsbeobachtungen oder für die Code- oder Trägerphasenmessungen von GNSS-Signalen). Die Dissertation von Omar García Crespillo eröffnet eine neue Sichtweise darauf, wie man mit einer solchen "Ungewissheit der Ungewissheit" im Bereich einer wichtigen Klasse von zeitkorrelierten stochastischen Prozessen, die häufig von Schätzern im Zustandsraum wie den (erweiterten) Kalman-Filtern verwendet werden, rigoros umgehen kann.

Insbesondere spezielle Formen von autoregressiven Prozessen wie die Gauß-Markov-Prozesse oder Linearkombination davon ermöglichen es, komplizierte Phänomene im Sensorverhalten zu erfassen, wie z.B. das Rauschen von Oszillatoren oder von Trägheitssensoren unterschiedlicher Qualität. Die Wahl der Modellstruktur und deren Parametrisierung ergibt sich aus den verfügbaren Informationen über die Daten oder aus anderem Wissen, wobei beide Quellen nur begrenzt Information enthalten. Dennoch ermöglichen einige neuere Methoden der Parameteridentifizierung eine genaue Quantifizierung dieser Unsicherheit. Allerdings war bei dieser Art von Prozessen nicht klar, wie die Unsicherheit der stochastischen Parameter im Konzept des "over-bounding" zum Zwecke der Integrität wiedergegeben werden kann. Obwohl die vorliegende Arbeit nur zeigt, wie diese Unsicherheit für einen Gauß-Markov-Prozess erster Ordnung korrekt berücksichtigt werden kann, lässt sich der beschriebene Weg der analytischen Herleitung auch auf stochastische Prozesse höherer Ordnung und Linearkombinationen davon ausdehnen. Unter diesem Gesichtspunkt ist die vorgestellte Methodik auch über den beispielhaften Fall der INS/GNSS-Integration hinaus auf Trägheitssensoren höherer Qualität anwendbar. Damit füllt diese Studie eine wichtige Wissenslücke und hat gleichzeitig einen unmittelbaren praktischen Nutzen für die auf einer Sensorintegration beruhenden Navigation.

Der Kern der Dissertation wurde auf mehreren Symposien des Institute of Navigation (ION) und des IEEE, wie z.B. ION-GNSS oder PLANS, sowie in der angesehenen ION-Zeitschrift für Navigation veröffentlicht.

Prof. Dr. Jan Skaloud
EPF Lausanne
Dissertationsleiter

Prof. Dr. Markus Rothacher
ETH Zürich
Präsident der SGK

Abstract

Safety-critical navigation applications require that estimation errors be reliably quantified and bounded. Over the last decade, significant effort has been put to guarantee a bounded position estimation by using Global Navigation Satellite Systems (GNSS) by means of satellite-based or ground-based augmentation systems (SBAS, GBAS) and Advanced Receiver Autonomous Integrity Monitoring (ARAIM) for aviation. This has been achieved by carefully designing models that overbound the different residual error components in range measurements (e.g., satellite clock and orbit, tropospheric and multipath among others). On the other hand, and as part of Aircraft-based Augmentation Systems (ABAS), the use of Inertial Reference Systems (IRS) has been traditionally included as additional source of redundant navigation information. More recently, the use of Inertial Navigation Systems (INS) with a wider spectrum of possible inertial sensor qualities in tighter integration with single-frequency GNSS has seen its way in a new Minimum Operational Performance Standard (MOPS). New GNSS/INS systems and standards could still benefit from the methodologies and aspects developed for future dual-frequency/multiconstellation GNSS standards. However, safety-related GNSS systems like ARAIM are snapshot-based, that is, the position estimation is performed independently at every epoch, whereas GNSS/INS systems are typically based on Kalman filtering (KF). Therefore, the existing error overbounding models and methodologies are not enough to produce a robust KF position estimation since the impact of time-correlation in measurements must also be accounted for. Moreover, it has been observed that the time-correlation of different GNSS errors presents also some level of uncertain behavior, which makes very challenging for linear dynamic systems to produce a guaranteed solution.

As proposed by GNSS Minimum Operational Performance Standards (MOPS), there are sources of time-correlated errors that can be well modelled using a first order Gauss-Markov process (GMP). Using this GMP parametric model, it is possible to capture the uncertain time-correlated nature of error processes by allowing the variance and time correlation constant of the GMP model to be in a bounded range. Under this situation, the first part of this thesis studies the propagation of the uncertain models through the Kalman filter estimation and provides new theoretical tools in time and frequency domain to bound the KF error estimation covariance. As a result, tight stationary bounding models on the GMP uncertain processes are derived in both continuous and discrete time domain. This is extended to non-stationary

models that provide tighter error bounding during an initial transient phase when measurements are first introduced (which will be relevant in scenarios with changing number of visible satellites). The new models can very easily be used during the KF implementation which might be very attractive by regulators and designers. In the second part of the thesis, the new overbounding GMP models are applied for a dual-frequency GPS-Galileo tightly-coupled GNSS/INS integration. The design of the filter and of error models is performed following compatibility with current aviation standards and ARAIM Working Group C results. The impact of the use of the new models is analysed in terms of conservativeness, integrity and continuity based on realistic operational simulations linked to airport runways. The benefit of an overbounded GNSS/INS solution is also compared with the current baseline ARAIM algorithm solution.
This thesis supports the evolution of safe GNSS-based positioning systems from only snapshot based to filtered solutions. Ensuring integrity for Kalman filter in general and for GNSS/INS systems in particular is a game changer to achieve higher performance levels for future dual-frequency multi-constellation aviation services and is of vital importance for new ground and air applications like autonomous vehicles or urban air mobility.

Key words: ABAS, GNSS/INS, Overbounding, ARAIM, Guaranteed estimation, Colored-noise

Zusammenfassung

Sicherheitskritische Navigationsanwendungen erfordern es, dass die Schätzfehler zuverlässig identifiziert, quantifiziert und begrenzt werden. In den letzten zehn Jahren wurden erhebliche Anstrengungen unternommen, eine Positionsschätzung mit beschränktem Fehler für die Luftfahrt zu gewährleisten. Dies wurde durch den Einsatz globaler Satellitennavigationssysteme (GNSS) und satellitengestützten oder bodengestützten Augmentierungssystemen (SBAS, GBAS) und Advanced Receiver Autonomous Integrity Monitoring (ARAIM) realisiert. Dafür war die sorgfältige Entwicklung von Fehlermodellen nötig, welche die verschiedenen Restfehlerkomponenten (z.B. in der Modellierung der Satellitenuhr und -orbit, Troposphäre und Mehrwegeffekte) der Entfernungsmessungen abdecken. Andererseits wurden im Rahmen von Avionik-basierten Augmentierungssystemen (ABAS) traditionell Trägheitsreferenzsysteme (IRS) als zusätzliche Quelle für redundante Navigationsinformationen eingesetzt. In jüngster Zeit hat die enge Integration von Trägheitsnavigationssystemen (INS) mit GNSS unter Berücksichtigung eines breiteren Spektrums an möglichen Trägheitssensoren verschieder Qualität ihren Weg in einen neuen Minimum Operational Performance Standard (MOPS) gefunden. Neue GNSS/INS-Systeme und -Normen könnten außerdem von den Methoden und Aspekten profitieren, welche für künftige GNSS-Normen unter Verwendung von Signalen in mehreren Frequenzenbändern und von mehreren Konstellationen entwickelt werden. Sicherheitsrelevante GNSS-Systeme wie ARAIM basieren jedoch auf einer Momentaufnahme des Systems, d. h. die Positionsschätzung wird in jedem Zeitschritt unabhängig von vorherigen durchgeführt. GNSS/INS-Systeme basieren in der Regel auf einer Kalman-Filterung (KF), welche eine zeitliche Korrelation des Systems berücksichtigt. Da die bestehenden Modelle und Methoden zur Fehlerbegrenzung die Auswirkung dieser Zeitkorrelation der Messungen aktuell nicht berücksichtigen, reichen diese nicht aus, um eine robuste KF-Positionsschätzung zu erzielen. Darüber hinaus wurde festgestellt, dass die Zeitkorrelation verschiedener GNSS-Fehler auch zusätzliche Unsicherheit birgt, was eine zuverlässige Fehlerbegrenzung darauf aufbauender Schätzungen in linearen dynamischen Systemen erheblich erschwert.

Wie in den GNSS MOPS vorgeschlagen, gibt es Arten von zeitkorrelierten Fehlern, die mit Hilfe von Gauß-Markov-Prozessen (GMP) gut modelliert werden können. Mit Hilfe dieses GMP-Parametermodells ist es möglich, die unsichere zeitkorrelierte Natur der Fehlerprozesse zu erfassen. Dies wird erreicht, indem man die Varianz und die Zeitkorrelationskonstante

des GMP-Modells in einem bestimmten, begrenzten Bereich zulässt. Der erste Teil dieser Arbeit untersucht für genau diesen Fall, die Ausbreitung der unsicheren Modelle durch die Kalman-Filter-Schätzung und liefert neue theoretische Werkzeuge im Zeit- und Frequenzbereich zur Begrenzung der Kovarianz der KF-Fehlerschätzung. Als Ergebnis werden enge stationäre Begrenzungsmodelle für die unsicheren GMP-Prozesse, sowohl im kontinuierlichen als auch im diskreten Zeitbereich, abgeleitet. Dies wird weiter auf nicht-stationären Modellen erweitert, welche eine engere Fehlerbegrenzung während einer anfänglichen Übergangsphase ermöglichen. Dies ist notwendig, wenn die Messungen zum ersten Mal eingeführt werden, z.B. in Szenarien mit einer wechselnden Anzahl von sichtbaren Satelliten. Die neuen Modelle können sehr einfach während der KF-Implementierung verwendet werden, was für Regulierungsbehörden und Designer sehr attraktiv sein könnte. Im zweiten Teil der Arbeit werden die neuen übergreifenden GMP-Modelle auf den Fall einer engen Kopplung zwischen GNSS und Trägheitsnavigation angewendet. Der Entwurf der Filter- und Fehlermodelle erfolgt unter Berücksichtigung der Kompatibilität mit aktuellen Luftfahrtstandards und den Ergebnissen der ARAIM Working Group C. Die Auswirkungen der Verwendung der neuen Modelle werden im Hinblick auf Konservativität, Integrität und Verfügbarkeit auf der Grundlage realistischer Flugbahnsimulationen analysiert. Der Vorteil einer überlagerten GNSS/INS-Lösung wird auch mit der aktuellen Basislösung des ARAIM-Algorithmus verglichen.
Diese Arbeit unterstützt die Evolution eines integritätsabgesicherten GNSS-basierten Positionierungssystemen von bisher schnappschussbasierter Verarbeitung hin zur Nutzung ganzer Zeitreihen von Messungen zur Positionsschätzung. Die Sicherstellung der Integrität von Kalman-Filtern im Allgemeinen und von GNSS/INS-Systemen im Besonderen ist ein entscheidender Faktor für das Erreichen höherer Leistungsniveaus in der Luftfahrt und von entscheidender Bedeutung für neue Anwendungen am Boden und in der Luft, wie z. B. autonome Fahrzeuge oder urbane Mobilität in der Luft.

Stichwörter: ABAS, GNSS/INS, Overbounding, ARAIM, Guaranteed estimation, Colored-noise

Contents

List of Figures

List of Tables

Acronyms

AAIM	Aircraft Autonomous Integrity Monitoring
ABAS	Aircraft based Augmentation System
ACF	Autocovariance Function
ACM	Autocovariance Matrix
ADIRS	Air Data Inertial Reference System
AHRS	Attitude and Heading Reference System
AL	Alert Limit
APV	Approach with Vertical Guidance
ARAIM	Advanced Receiver Autonomous Integrity Monitoring
ARAIM ADD	ARAIM Algorithm Design Document
ARNS	Aeronautical Radionavigation Service
AV	Allan Variance
CAT	Category (airport)
CDF	Cumulative Density Function
CDMA	Code-Division Multiple Access
CMC	Code-minus-Carrier
CN0	Carrier to Noise ratio
DFDC	Dual-Frequency Dual-Constellation
DFMC	Dual-Frequency Multi-Constellation
DLR	Deutsches Zentrum für Lüft- und Raumfahrt (German Aerospace Center)
DME	Distance Measurement Equipment
DO	Document (RTCA standard)
ECEF	Earth-Centered Earth-Fixed
EKF	Extended Kalman Filter

EU	European Union
EUROCAE	European Organisation for Civil Aviation Equipment
FAF	Final Approach Fix
FDE	Fault Detection and Exclusion
FMS	Flight Management System
GBAS	Ground based Augmentation System
GMP	Gauss-Markov Process
GMWM	Generalized Method of Wavelet Moments
GNSS	Global Navigation Satellite System
GPS	Global Positioning System
H-ARAIM	Horizontal ARAIM
HAL	Horizontal Alert Limit
HMI	Hazardous Misleading Information
HPL	Horizontal Protection Level
ICAO	International Civil Aviation Organization
IF	Ionosphere Free
IMU	Inertial Measurement Unit
INS	Inertial Navigation System
IR	Integrity Risk
IRS	Inertial Reference System
ISM	Integrity Support Message
KF	Kalman filter
LDS	Linear Dynamic System
LPV	Localizer Performance with Vertical guidance
LS	Least-Squares
MAAST	Matlab Algorithm Availability Simulation Tool
MFMC	Multi-Frequency Multi-Constellation
MHSS	Multiple Hypothesis Solution Separation
MOPS	Minimum Operational Performance Standard
N/A	Non Applicable
NPA	Non-Precision Approach
PDF	Probability Density Function

PHMI	Probability of Hazardous Misleading Information
PL	Protection Level
PPP	Precise Point Positioning
PSD	Power Spectral Density
PVT	Position Velocity and Time
RAIM	Receiver Autonomous Integrity Monitoring
RINEX	Receiver Independent Exchange Format
RNP	Required Navigation Performance
RTCA	Radio Technical Commission for Aeronautics
SARPs	Standards and Recommended Practices
SBAS	Satellite based Augmentation System
SFSC	Single-Frequency Single-Constellation
SIS	Signal-in-Space
SISA	Signal-in-Space Accuracy
SISRE	Signal-in-Space Range Error
SS	Solution Separation
STD, std	Standard deviation
TTA	Time-To-Alert
URA	User Range Accuracy
URE	User Range Error
US	United States
V-ARAIM	Vertical ARAIM
VAL	Vertical Alert Limit
VOR	VHF Omnidirectional Range
VPL	Vertical Protection Level
WAAS	Wide Area Augmentation System
WGN	White Gaussian Noise
WLS	Weighted Least-Squares
WV	Wavelet Variance

Notation and Nomenclature

Conventions

$\mathbf{A}$	Matrix
$\mathbf{A}_i$	Matrix indexed for some purpose
$\mathbf{A}_{ij}$	Matrix indexed for some purpose
$\mathbf{A}_k$	Matrix indexed with time index k
$\mathbf{A}_{0:k}$	Matrix of accumulated matrices from 0 to time index k,i.e., $\mathbf{A}_{0:k} = \begin{bmatrix} \mathbf{A}_0 & \mathbf{A}_1 & \cdots & \mathbf{A}_k \end{bmatrix}$
$\mathbf{A}_\mathrm{K}$	Matrix of accumulated matrices from 0 to time index k
$\mathbf{A}^{-1}$	The inverse matrix of the matrix $\mathbf{A}$
$\mathbf{A}^\mathrm{T}$	Transposed matrix
$\mathbf{A}^{a\times b}$	Matrix of size $a \times b$
a_{ij}	The (i,j)th entry of the matrix $\mathbf{A}$
a	Scalar
$\mathbf{a}$	Vector (column-wise)
$\mathbf{a}_i$	Vector indexed for some purpose
$\mathbf{a}_k$	Vector indexed with time index k
$\mathbf{a}_{0:k}$	Column vector of accumulated vectors from 0 to time index k
$\mathbf{a}_\mathrm{K}$	Column vector of accumulated vectors from 0 to time index k
a_i	The ith element of the vector $\mathbf{a}$
$\mathbf{a}^\mathrm{T}$	Transposed vector
$\mathbf{I}$	Identity matrix
$\mathbf{0}$	The null matrix. Zero in all entries
$\mathbf{1}$	Matrix or vector with one in all entries
$\lvert a\rvert$	Absolute value of a
$\lvert\mathbf{A}\rvert$	Matrix with element-wise absolute value of elements of $\mathbf{A}$
$\mathrm{diag}(\mathbf{A})$	Vector with the diagonal elements of $\mathbf{A}$
$\mathrm{diag}(\mathbf{a})$	Diagonal matrix with the elements of vector $\mathbf{a}$
a_min	Minimum value of a from a certain range. Assuming $a \in [a_\mathrm{min}, a_\mathrm{max}]$
a_max	Maximum value of a from a certain range. Assuming $a \in [a_\mathrm{min}, a_\mathrm{max}]$

$[\mathbf{a}\times]$	Skew-symmetric matrix of $\mathbf{a}$, such that $[\mathbf{a}\times] = \begin{bmatrix} 0 & -a_3 & a_2 \\ a_3 & 0 & -a_1 \\ -a_2 & a_1 & 0 \end{bmatrix}$
$\mathbf{A}-\mathbf{B} \geq \mathbf{0}$	The matrix resulting from the difference between $\mathbf{A}$ and $\mathbf{B}$ is a positive semidefinite matrix.
$\mathbf{A} \geq \mathbf{B}$	The matrix resulting from the difference between $\mathbf{A}$ and $\mathbf{B}$ is a positive semidefinite matrix. This is equivalent to $\mathbf{A}-\mathbf{B} \geq 0$
$\mathbb{R}$	Real numbers
$\mathbb{Z}$	Integer numbers
$\mathbb{N}_0$	Natural numbers set including zero

Operators

$\mathrm{E}[\cdot]$	Expectation operator
$\mathrm{Var}[\cdot]$	Variance operator
$\mathrm{Cov}[\cdot]$	Covariance
$\mathbf{T}$	This matrix contains ones and zeros and it is used in the thesis as a multiplicative operator to modify the order of the elements in a different matrix or to change the original size of it by including new rows or columns with zeros
$\boldsymbol{\varepsilon}$	Vector of zeros and ones used to extract certain elements or dimensions of interest from a vector or matrix

Constants and Physical Magnitudes

f	Frequency	
ω	Angular frequency, such that $\omega = 2\pi f$	
λ	Signal wavelength	
c	Speed of light in vacuum	$299\,792\,458\,\mathrm{m\,s^{-1}}$
ω_{ie}	Earth's angular rate	$7.292\,115\,9 \times 10^{-5}\,\mathrm{rad\,s^{-1}}$
$\mathrm{R_N}$	Meridian radius of curvature (Earth ellipsoid)	
$\mathrm{R_E}$	Transverse radius of curvature (Earth ellipsoid)	
g_0	Surface gravity	
$f_{\mathrm{L1}}, f_{\mathrm{E1}}$	GPS L1 and Galileo E1 frequency	1575.42 MHz
$f_{\mathrm{L5}}, f_{\mathrm{E5a}}$	GPS L5 and Galileo E5a frequency	1176.45 MHz
Δt	Time interval	
k	Time index, $k \in \mathbb{N}_0$	

GNSS Measurements

ρ	Code measurement
ϕ	Carrier-phase measurement

ρ_{IF}	Ionospheric-free code measurement
ϕ_{IF}	Ionospheric-free carrier-phase measurement
$\tilde{\rho}(\mathbf{x}_0)$	Predicted code range measurement based on linearization point $\mathbf{x}_0$
$\tilde{\phi}(\mathbf{x}_0)$	Predicted phase range measurement based on linearization point $\mathbf{x}_0$
dt_{u}	Receiver clock bias in seconds
b_{u}	Receiver clock bias in meters
dt	Satellite clock bias
$\Delta\mathrm{S}$	Residual clock and ephemeris error after using broadcast navigation message for satellite position and clock error computation
dI	Ionospheric delay
dT	Tropospheric delay
B_{u}	Receiver instrumental (hardware) delay
B	Satellite instrumental (hardware) delay
mp	Multipath delay
N_ϕ	Carrier-phase ambiguity term
β	Travel time
ϵ	Residual Gaussian noise
$\mathbf{u}$	Normalized line of sight vector from user to satellite
θ	Satellite elevation

Inertial Navigation

i	It refers to the inertial frame
e	It refers to the ECEF frame
n	It refers to the local-level navigation frame
b	It refers to the body frame
$\mathbf{f}^b$	Specific force measurement in b-frame
$\mathbf{w}^b$	Turn rate measurement in b-frame
$\boldsymbol{\psi}$	Attitude (roll, pitch, yaw)
$\mathbf{C}_b^n$	Direction Cosine Matrix (DCM) representing the rotation from body to local-level navigation frame.
$\delta\boldsymbol{\psi}$	Error in attitude
$\mathbf{v}$	Velocity
$\delta\mathbf{v}$	Error in velocity
v_{N}	North component of the velocity vector
v_{E}	East component of the velocity vector
v_{D}	Down component of the velocity vector
$\mathbf{p}$	Position (latitude, longitude, altitude)
$\delta\mathbf{p}$	Error in position
$\mathbf{b}_f$	Accelerometer biases

$\mathbf{b}_w$	Gyroscope biases
φ	Latitude
λ	Longitude
h	Altitude

Estimation and Kalman filter

$\mathbf{x}$	Parameter or state vector (physical quantity)
$\hat{\mathbf{x}}$	Estimated parameter vector (e.g., via least-squares)
$\mathbf{x}_0$	Linearization point of $\mathbf{x}$ for non-linear estimation
$\Delta\mathbf{x}$	Increment from the linearization point to total magnitude, such that $\mathbf{x} = \mathbf{x}_0 + \Delta\mathbf{x}$
$\mathbf{P}$	Covariance matrix of state or parameter vector $\mathbf{x}$
$\mathbf{P_y}$	Covariance matrix of vector $\mathbf{y}$
$\mathbf{z}$	Measurement vector
$\mathbf{R}$	Covariance of a stochastic process or measurement error
$\mathbf{H}$	Measurement matrix
$\mathbf{W}$	Estimator weighting matrix
$\mathbf{S}$	Estimator matrix
$\mathbf{r}$	Residual vector
$\dot{\mathbf{x}}$	Time differential state (continuous-time)
$\dot{\mathbf{P}}$	Time differential covariance matrix (continuous-time)
$\mathbf{F}$	Dynamic propagation matrix
$\mathbf{Q}$	Process noise covariance
$\mathbf{G}$	Process noise to state projection matrix
$\mathbf{J}$	Measurement noise projection matrix
$\mathbf{K}$	Kalman gain matrix
$\mathbf{x}_{k\|k-1}$	KF predicted mean value of the states at time k (discrete-time)
$\mathbf{P}_{k\|k-1}$	KF predicted covariance of the states at time k (discrete-time)
$\mathbf{x}_{k\|k}$	KF aposteriori mean estimation of the states at time k (discrete-time)
$\mathbf{P}_{k\|k}$	KF aposteriori covariance estimation of the states at time k (discrete-time)
$\boldsymbol{\Phi}$	Dynamic propagation matrix (discrete-time)
$\boldsymbol{\gamma}$	KF innovation vector
$\boldsymbol{\xi}$	KF main states of interest (e.g., position, velocity, etc.)
$\mathbf{a}$	KF augmented states (in this thesis mainly referring to time-correlated bias errors modelled as Gauss-Markov processes)
$\mathbf{e}$	Error vector of an estimated parameter or state, such that $\mathbf{e} \triangleq \hat{\mathbf{x}} - \mathbf{x}$ or $\mathbf{e} \triangleq \hat{\mathbf{x}}_{k\|k} - \mathbf{x}_k$
$\boldsymbol{\zeta}$	Vector containing the error $\mathbf{e}$ of an estimator expanded with a complete or partial vector of the true parameters, such that $\boldsymbol{\zeta} = \begin{bmatrix} \mathbf{e}^{\mathrm{T}} & \mathbf{x}^{\mathrm{T}} \end{bmatrix}^{\mathrm{T}}$. This is used for the sensitivity analysis in Chapter 4

$\hat{\mathbf{A}}$	Chosen, designed or modeled matrix $\mathbf{A}$ in the estimator
$\Delta\mathbf{A}$	Difference between modeled and true matrix $\mathbf{A}$, such that $\Delta\mathbf{A} \triangleq \hat{\mathbf{A}} - \mathbf{A}$

Error Models

σ_{URA}	Integrity bound (standard deviation) for GPS ephemeris and clock residual error
σ_{URE}	Accuracy bound (standard deviation) for GPS ephemeris and clock residual error
σ_{SISA}	Integrity bound (standard deviation) for Galileo ephemeris and clock residual error
σ_{SISRE}	Accuracy bound (standard deviation) for Galileo ephemeris and clock residual error
m_{tropo}	Elevation dependent wet tropospheric mapping function
σ_{tropo}	Residual tropospheric uncertainty at zenith
$\sigma_{mp,\rho,sm}$	Residual uncertainty in ionospheric-free smoothed code measurements due to multipath contribution
$\sigma_{mp,\rho}$	Residual uncertainty in ionospheric-free raw code measurements due to multipath contribution
$\sigma_{mp,\phi}$	Residual uncertainty in ionospheric-free raw carrier-phase measurements due to multipath contribution
σ_{ϵ_ρ}	Residual uncertainty in ionospheric-free raw code measurements due to noise contribution
σ_{ϵ_ϕ}	Residual uncertainty in ionospheric-free raw carrier-phase measurements due to noise contribution
σ_{clk}	Uncertainty of receiver clock bias dynamic model
$\hat{\sigma}^2_{\Delta\text{S}}$	Variance of GMP modeling residual ephemeris and satellite clock error
$\hat{\tau}_{\Delta\text{S}}$	Time-correlation constant of GMP modeling residual ephemeris and satellite clock error
$\hat{\sigma}^2_{\text{tropo}}$	Variance of GMP modeling residual tropospheric error
$\hat{\tau}_{\text{tropo}}$	Time-correlation constant of GMP modeling residual tropospheric error
$\hat{\sigma}^2_{mp,\rho}$	Variance of GMP modeling multipath error in code measurement
$\hat{\tau}_{mp,\rho}$	Time-correlation constant of GMP modeling multipath error in code measurement
$\hat{\sigma}^2_{mp,\phi}$	Variance of GMP modeling multipath error in carrier-phase measurement
$\hat{\tau}_{mp,\phi}$	Time-correlation constant of GMP modeling multipath error in carrier-phase measurement

Stochastic Processes and Error Bounding

$\mathcal{N}(\mu,\sigma^2)$	Normal distribution with mean μ and variance σ^2
$\chi^2(n,\lambda^2)$	Chi-square distribution with n degrees of freedom and λ^2 non-central parameter
$\mathcal{GM}(\sigma^2,\tau)$	First-order Gauss-Markov model with variance σ^2 and time-correlation τ

$R(\Delta t)$	Autocovariance function for time interval Δt
$\bar{R}(\Delta t)$	Autocorrelation function for time interval Δt. Definition in Section 3.1
$S_{\mathrm{c}}(\omega)$	Power spectral density (continuous-time)
$S_{\mathrm{d}}(\omega)$	Power spectral density (discrete-time)
$\hat{S}(\omega)$	Bounding power spectral density
$\hat{\tau}$	Time-correlation constant of GMP chosen by designer. In the thesis it is used to describe the parameter that guarantee bounding conditions. It can contain the subscript c or d to refer to continuous-time or discrete-time, respectively
$\hat{\sigma}^2$	Variance of Gauss-Markov model chosen by designer. In the thesis it is used to describe the parameter that guarantee bounding conditions. It can contain the subscript c or d to refer to continuous-time or discrete-time, respectively
α	Gauss-Markov correlation decay (discrete-time), such that $\alpha = e^{-\frac{\Delta_t}{\tau}}$
q	Used in this context to expressed the variance of the white noise in GMP

Integrity Monitoring and MHSS Parameters

q_r	Test statistic based on normalized residuals squared
q_Υ	Test statistic based on normalized innovation squared
q_{ss}	Test statistic based on solution separation
T	Test statistic threshold
AL	Position error alert limit
H0	Fault-free (nominal) hypothesis
H1	Faulty (alternate) hypothesis
h	Hypothesis index
N_h	Number of fault hypothesis
P_h	Probability of fault hypothesis h
P_{NM}	Total probability of non-monitored hypothesis
P_{fa}	Probability of false alarm
$\mathrm{P}_{\mathrm{HMI}}$	Probability of hazardous misleading information (integrity risk)
$\mathrm{IR}_{\mathrm{req}}$	Integrity risk requirement
^{0}	It refers to the all-in-view solution
^{h}	It refers to the fault-tolerant hypothesis h
$\mathrm{Q}(\cdot)$	Tail distribution function of the standard normal distribution
$\mathrm{Q}^{-1}(\cdot)$	Inverse of tail distribution function
$\mathrm{P}_{\mathrm{sat}}$	prior probability of satellite fault
$\mathrm{P}_{\mathrm{const}}$	prior probability of constellation fault
b_{nom}	Nominal bias (range)
b_l	Nominal bias projected in coordinate l
$\mathrm{P}_{\mathrm{LOC}}$	Probability of loss of continuity

1 Introduction

1.1 Background

Navigation systems in safety-critical transportation applications must meet different levels of requirements in terms of accuracy, integrity, availability and continuity in order to reach the required level of maturity and trust. Over the last decades, satellite navigation has position itself as the primary positioning system in aviation as it is envisioned for other future land and air autonomous applications. In aviation, Global Navigation Satellite Systems (GNSS) is augmented with other systems in order to achieve the safety required for certification. The current augmentation systems are Satellite based Augmentation System (SBAS), Ground based Augmentation Systems (GBAS) and Aircraft based Augmentation System (ABAS). SBAS and GBAS rely on the transmission of corrections to the user GNSS receiver to correct for large portion of *Signal-in-Space* (SiS) errors in transmitted GNSS signals affecting positioning and its integrity. ABAS, on the other side, relies on onboard redundancy either between satellite measurements or between GNSS receiver and other sensors to protect against system or observation faults. The first type of ABAS based on GNSS onboard redundancy is Receiver Autonomous Integrity Monitoring (RAIM) and it is used for flight predictive monitoring and fault detection during non-critical flight phases. Its evolution is called Advanced RAIM (ARAIM) and it is based on the availability of multiple GNSS frequencies and constellations. Significant effort has been put by regulators and the scientific community to develop ARAIM for this purpose. This included on one side the development of positioning, fault detection and integrity risk quantification algorithms and, on the other side, the development of specific methodologies and error models that guarantee a safe positioning information. ARAIM is based on snapshot estimators, in the sense that a position solution at one epoch is computed independently of past. This has the advantage that the integrity assessment can be done to some extent separately for each epoch.

The other type of ABAS systems are generally named Aircraft Autonomous Integrity Moni-

toring (AAIM). Among them, the most important one includes the use of single or multiple Inertial Reference System (IRS) onboard the aircraft. The position solution from high grade inertial units can be used as consistency check with satellite positioning or other systems. Traditionally IRS is initiated at the gate and it drifts over time due to residual errors in initial attitude and the accumulation of errors from its accelerometers and gyroscopes as they are integrated into velocity and then position. In order to bound the IRS error growth, avionics systems might correct periodically their position with other radionavigation systems like DME or GNSS. The most common algorithm to combine GNSS with IRS is the Kalman filter, which is a sequential estimator. In future avionic systems targeting stringent operations and possibly using inertial systems with higher error drift rate, a tighter GNSS/INS integration must be considered together with dedicated fault detection and integrity monitoring functions. Although ARAIM and AAIM development have recently grown to some extent in parallel, they share the same fundamentals. However, there are still some challenges to be overcome within GNSS/INS integrated navigation so that it can adopt some of the recent developments in multi-frequency, multi-constellation GNSS positioning and integrity monitoring. Safe error modelling and especially accounting in error model uncertainties is one of such aspects.
Indeed, correlated errors affect GNSS code and carrier phase measurements as well as observations of inertial sensors. If not properly modelled, a GNSS/INS Kalman filter estimator would provide misleading information on the estimated confidence. This is challenging as some parameters related to the time-correlated error model might be difficult to obtain accurately. Model uncertainty has been well treated for GBAS and ARAIM by using dedicated overbounding methodologies. However these methods were developed to cover the proper integrity risk quantification only for snapshot estimators like the classical GNSS only least-squares. Answer how to better handle the possible error model uncertainty for time correlated errors and their impact on GNSS/INS position estimation is the main driver of this thesis.

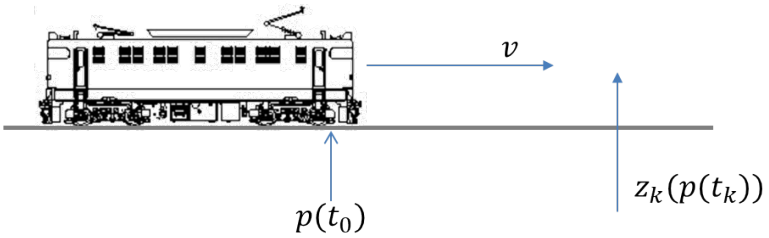

Figure 1.1: Train localization problem

1.2 Problem Statement and Example

In order to understand the problem with linear dynamic estimators under the limited knowledge of time-correlated processes, a simple example is first presented. Consider the localization of a train that is travelling along a straight track as depicted in Fig. 1.1. The goal is to estimate the position of the train at the start of mission at a certain time t_0, such that $p_0 = p(t_0)$ along with its constant speed v. Direct observation of the current position of the train at discrete times t_k is available with the measurement z_k. However, let us assume that this measurement contains both a white noise error ν and a varying bias a that can be modelled by a Gauss-Markov process. Modeling the GMP as an augmented state, the problem can be summarized by the following set of dynamic and measurement equations:

$$\begin{bmatrix} p_{0,k} \\ v_k \\ a_k \end{bmatrix} = \begin{bmatrix} 1 & 0 & 0 \\ 0 & 1 & 0 \\ 0 & 0 & \alpha \end{bmatrix} \begin{bmatrix} p_{0,k-1} \\ v_{k-1} \\ a_{k-1} \end{bmatrix} + \begin{bmatrix} 0 \\ 0 \\ \sqrt{q_a} w_k \end{bmatrix}, \tag{1.1}$$

$$z_k = \begin{bmatrix} 1 & k\Delta t & 1 \end{bmatrix} \begin{bmatrix} p_{0,k} \\ v_k \\ a_k \end{bmatrix} + \nu_k, \tag{1.2}$$

with

$$\begin{aligned} &\alpha = e^{\frac{-\Delta_t}{\tau}}, \\ &q_a = \sigma_a^2(1 - e^{\frac{-2\Delta_t}{\tau}}), \end{aligned} \quad \text{and} \quad \begin{aligned} &w_k = \mathcal{N}(0,1), \\ &\nu_k = \mathcal{N}\left(0, \sigma_\nu^2\right), \end{aligned} \tag{1.3}$$

where a is the augmented GMP state related to the measurement z, w is a white Gaussian noise and ν is the measurement noise. The GMP parameters are its variance σ_a^2 and its time correlation constant τ. Finally Δt the time interval between measurements and $k \in \mathbb{N}_0$ is the time index. Assuming that the parameters of the time correlated GMP can not be determined exactly and can only be known within a certain range, such that $\sigma_a^2 \in [\sigma_{\text{min}}^2, \sigma_{\text{max}}^2]$ and $\tau \in [\tau_{\text{min}}, \tau_{\text{min}}]$, the following question is asked:

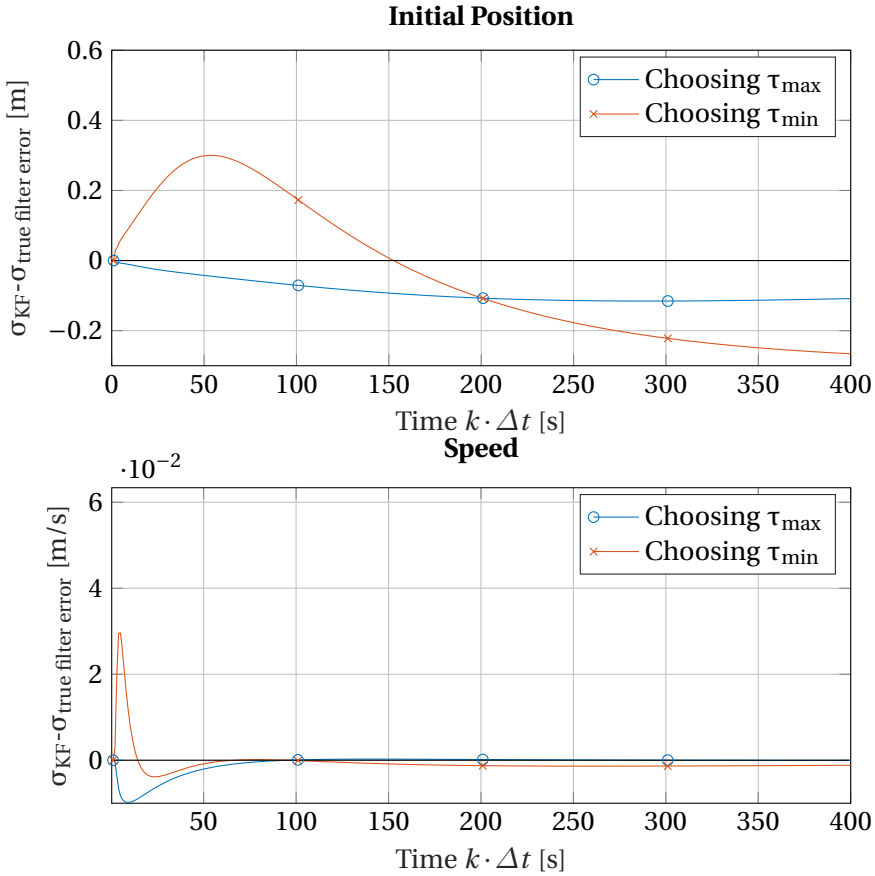

Figure 1.2: Difference between KF estimated error standard deviation (σ_{KF}) and true KF error standard deviation ($\sigma_{\text{true filter error}}$) for $\sigma^2_{min} = \sigma^2_{max} = 1\,m^2$, $\tau_{min} = 10$ s, $\tau_{max} = 100$ s and $\tau_{true} = 50$ s

> ❓ *Under the presence of Gauss-Markov processes with uncertain but bounded parameters, which model or values of variance and time correlation constant should be used so that the estimated error covariance of a Kalman filter estimator properly overbounds the true error?*

For many years, it has been assumed that the largest possible value of the time correlation constant would produce the safest estimation. This can be easily shown wrong within the given example. Figure 1.2 shows for the estimated initial position and constant velocity the difference between the estimated standard deviation from the Kalman filter covariance and the true error standard deviation over time for two cases: one designing the KF with the minimum value of the time constant (i.e., $\tau = \tau_{min}$) and the other one choosing the maximum value τ_{max}. For both limiting values, there are time intervals when the difference is negative. This means that the estimated standard deviation (or variance) via KF does not upper bound the true estimated error.

The plots were obtained by choosing an arbitrary value for the true time constant (that is normally not known) in the middle of the range of possible error parameters values. The true estimated error variance can be obtained in this case either via Monte Carlo simulation or via sensitivity analysis as shown in Appendix A.1.

The main contribution of this thesis is in the development of theoretical approaches that allows to properly account for parameter uncertainty of an error model as GMP so that the predicted covariance of the KF estimator safely (yet tightly) overbounds the true error over the whole interval.

1.3 Thesis Outline

This work is organized in three main parts preceded by this introductory chapter:

Part I contains preliminary information relevant for the main research subject. In particular, Chapter 2 provides an introduction to Aircraft based Augmentation Systems (ABAS) in relation to main safety and integrity requirements. The chapter discusses the most important elements of GNSS navigation and integrity monitoring as well as the fundamentals of GNSS/INS integration. Chapter 3 discusses essential risk and error bounding elements related to stochastic error models and their propagation within linear dynamic systems.

The second part of the thesis provides theoretical development for considering uncertainty in parameters describing time-correlated errors. Different techniques and criteria are presented to derive bounding conditions in time and frequency domain. As a result new Gauss-Markov error parameters are derived in continuous time in Chapter 4 and in discrete-time in Chapter 5.

The last part of the thesis applies the newly derived error parameters in the design of a safe GNSS/INS algorithm with integrity monitoring in Chapter 6. Chapter 7 presents a simulation framework to study the performance of the algorithms and the achievable results in terms of accuracy, integrity and continuity.

Finally, Chapter 8 closes this document with the main achievements and future research recommendations.

1.4 Main Original Contributions

The main contributions of this thesis are :

1. **Development of new theoretical tools in time and frequency domain to bound uncertain time-correlated errors in linear dynamic systems:** The traditional use of Kalman filter sensitivity analysis is extended and particularized to consider a specific situation of uncertain error parameters within Gauss-Markov structure. With this method new conditions are obtained that allow for the explicit check of bounding conditions on aposteriori Kalman filter covariance. In parallel, the use of frequency domain analysis is presented and linked with the KF estimated error covariance, which allows to translate KF covariance bounding conditions to the frequency domain.

2. **Rigorous derivation of stationary Gauss-Markov bound model in continuous and discrete-time with new tight bounding:** Based on the sensitivity analysis tool and the frequency domain framework, new conditions and models are derived for bounding stationary Gauss-Markov processes with uncertain time-correlation constant and uncertain variance. The new models are rigorously proved in the continuous-time and discrete-time domain. Furthermore, it is proven that model parameters derived in the continuous time can also be used in discrete-time to provide bounding conditions.

3. **Rigorous derivation of non-stationary Gauss-Markov tight bounding model in continuous and discrete-time:** The Gauss-Markov stationary bounding models are further made tighter by the derivation of a non-stationary GMP model with a transient phase. This can allow to avoid conservatism once a measurement is started to be used in an estimator. Rigorous proofs are provided for both the continuous time and the discrete time domain.

4. **Robust design of dual-frequency, GPS-Galileo GNSS/INS integration and integrity monitoring with uncertain GNSS time-correlated Errors:** Under the presence of uncertain parameters in time-correlated error models describing uncertainties in GNSS satellite ephemeris and clocks, tropospheric delays, code and carrier-phase multipath, a new GNSS/INS Kalman filter is designed that considers augmented states for every correlated process. The augmented states use the GMP model parameters that guarantee bounding conditions. In parallel, a full integrity monitoring architecture is presented based on a Multiple Hypothesis Solution Separation (MHSS) algorithm similar to ARAIM.

5. **New methodology for the assessment of loss of continuity of GNSS and GNSS/INS due to manoeuvres:** A new method for procedure-based evaluation and simulation is presented. It links certain aircraft trajectories with airports locations and runways

directions. This allows for a more realistic evaluation of GNSS/INS and ARAIM performance when satellites appear and disappear from receiver tracking due to orientation and antenna mask.

This thesis partially stems from author's contribution to many publications, list of which is given on page 139.

Part I Preliminaries

2 Aircraft-based Augmentation Systems

In order to achieve the navigation system requirements in terms of accuracy, integrity, availability and continuity, positioning based on GNSS must be augmented. According to the International Civil Aviation Organization (ICAO) GNSS Standards and Recommended Practices (SARPs) [1], there are three different augmentation systems:

1. Satellite-based Augmentation System (SBAS) that guarantees signal integrity by broadcasting from geostationary satellites pseudorange corrections and other information on satellite health.
2. Ground-based Augmentation System (GBAS) is designed for CAT I and in the future CAT II/III precision approaches and landing. GBAS relies on corrections sent to the aircraft based on a network of ground stations at airport location.
3. The third type of augmentation is Aircraft-based Augmentation System (ABAS). Contrary to SBAS and GBAS that relies on additional infrastructure, ABAS relies only on information onboard the aircraft. In principle ABAS relies either on cross-checks between GNSS observations (called Receiver Autonomous Integrity Monitoring) or on coherence with additional aircraft sensor information such as barometric altimetry or Inertial Reference System (IRS). The latter is called Aircraft Autonomous Integrity Monitoring (AAIM).

This chapter provides more insights about the important navigation operational requirements for aircraft and then focuses on ABAS in relation to the topic of this thesis.

2.1 Navigation System Requirements

Each aircraft operation needs to satisfy a certain level of different navigation requirements. The main important requirements are defined by ICAO as [1]:

- **Accuracy**: *The accuracy of an estimated or measured position of a craft (vehicle, aircraft, or vessel) at a given time is the degree of conformance of that position with the true position of the craft at that time. Since accuracy is a statistical measure of performance, a statement of navigation system accuracy is meaningless unless it includes a statement of the uncertainty in position that applies.*

- **Integrity**: *A measure of the trust that can be placed in the correctness of the information supplied by the total system. Integrity includes the ability of a system to provide timely and valid warnings to the user (alerts).*

- **Time-To-Alert (TTA)**: *The maximum allowable time elapsed from the onset of the navigation system being out of tolerance until the equipment enunciates the alert.*

- **Continuity**: *The continuity of a system is the ability of the total system (comprising all elements necessary to maintain craft position within the defined area) to perform its function without interruption during the intended operation. More specifically, continuity is the probability that the specified system performance will be maintained for the duration of a phase of operation, presuming that the system was available at the beginning of that phase of operation.*

- **Availability**: *The portion of time during which the system is simultaneously delivering the required accuracy and integrity.*

The necessary level of integrity that a navigation system must fulfill for each operation is normally established by an horizontal or vertical position alert limit (HAL, VAL) and an associated integrity risk (IR) to overpass it. The integrity risk, also called probability of Hazardous Misleading Information (P_{HMI}) can be therefore defined as the following probability:

$$P_{HMI} = P\left(|e| > AL\right), \tag{2.1}$$

where AL is the alert limit and e is the position error in a given dimension. Since the actual error of the navigation system is in principle unknown, navigation systems usually compute a bound of it called protection level (PL). By comparing the computed PL with the AL, the navigation system an integrity violation can be declared. Protection levels are separated into horizontal and vertical domain in order to support specific operational requirements. This situation is depicted in Fig. 2.1. Table 2.1 provides a summary of the main navigation performance requirements for aircraft operations up to CAT I precision approach.

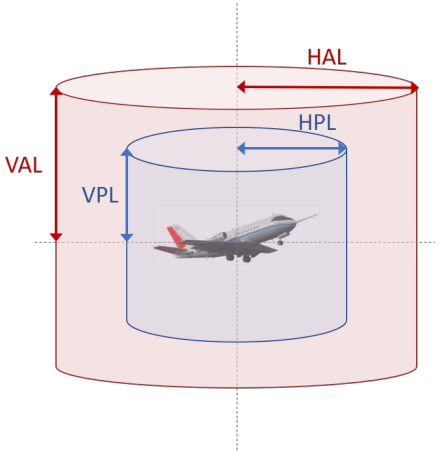

Figure 2.1: Alert limits and Protection Levels illustration

2.2 Current ABAS Standards

ABAS systems are already considered in aircraft avionics standards to support some of the operations in Table 2.1. Figure 2.2 shows an applicability map of existing GNSS ABAS and inertial-related Minimum Operational Performance Standards (MOPS) depending on the level of GNSS use (single-frequency, single constellation or dual-frequency, multi-constellation) and the inertial system performance (navigation-grade IRS, Attitude and Heading Reference System (AHRS) grade with gyrocompassing capability or AHRS with limited gyrocompassing capability). In the following, more details are listed about the coverage of such technologies in the US Radio Technical Commission for Aeronautics (RTCA) documents (DO) and the European Organisation for Civil Aviation Equipment (EUROCAE) documents (ED) with respect to where the research subject is positioned:

- **RTCA DO-334,** ***MOPS for Strapdown Attitude and Heading Reference Systems (AHRS) [5]***: The purposed of this MOPS is mainly related to the provision of AHRS functionality in particular for pitch and roll outputs, but also heading. It also considers possible GNSS aiding to augment the AHRS. Although this MOPS does not provide navigation capability, other ABAS navigation systems using inertial systems must first comply with it.

- **RTCA DO-316,** ***MOPS for Global Positioning System/Aircraft Based Augmentation System Airborne Equipment [6]***: This is the main current GNSS ABAS standard. It covers the use of RAIM and other Fault Detection and Exclusion (FDE) functions. In its Appendix R, it provides guidance for the tight integration of single-frequency GPS/Inertial system. Its intended use is to enhanced en-route operations.

Table 2.1: Navigation Performance Requirements [1]–[4]

Operation	**Accuracy** (Horizontal, Vertical) (Equiv. 1-σ)	**Integrity Risk**	**HAL, VAL**	**Time to Alert**	**Continuity**	**Availability**
Oceanic en-route	3.7 km, N/A	10^{-7}/h	7.4 km, N/A	5 min	10^{-4}/h to 10^{-8}/h	0.99 to 0.99999
Continental en-route	1.85 km, N/A	10^{-7}/h	3.7 km, N/A	5 min	10^{-4}/h to 10^{-8}/h	0.99 to 0.99999
Terminal	370 m, N/A	10^{-7}/h	1.85 km, N/A	15 s	10^{-4}/h to 10^{-8}/h	0.99 to 0.99999
NPA	110 m, N/A	10^{-7}/h	556 m, N/A	10 s	10^{-4}/h to 10^{-8}/h	0.99 to 0.99999
APV-I	8 m, 10 m	$1...2\times10^{-7}$/ approach	40 m, 50 m	10 s	$1...8\times10^{-6}$/ 15 s	0.99 to 0.99999
LPV-200	8 m, 2 m (1.87 m fault-free)	$1...2\times10^{-7}$/ 150 s	40 m, 35 m	6 s	$1...8\times10^{-6}$/ 15 s	0.99 to 0.99999
CAT I Autoland	8 m, 2 m	$1...2\times10^{-7}$/ 150 s	40 m, 10 m	6 s	$1...8\times10^{-6}$/ 15 s	0.99 to 0.99999

- **RTCA DO-229 Appendix R,** ***Requirements and Test Procedures for Tightly Integrated GPS/Inertial Systems [7]***: Although RTCA DO-229 is an SBAS/WAAS standard, in its Appendix R, it provides guidance for GPS/Inertial Systems when SBAS corrections are not available. It complements or extends the information in RTCA DO-316.

- **RTCA DO-384,** ***MOPS for GNSS Aided Inertial Systems [8]***: This is the first dedicated standard for GPS/Inertial Systems. It extends the applicability of Appendix R in RTCA DO-316 and RTCA DO-229 to AHRS-grade inertial units and other operation apart from en-route. For the GNSS sensor it follows the GNSS standards and it considers only single-frequency GPS signals.

- **EUROCAE ED-259,** ***MOPS for Galileo / Global Positioning Sytem / SBAS Airborne Equipment [9]***: It is an initial issue of a dual-frequency multi-constellation GNSS standard. Since GNSS SBAS equipment will also be able to operate without SBAS corrections by using ABAS, this standards also contains guidance for RAIM and H-ARAIM.

Thanks to the GNSS modernization plans, dual frequency multi-constellation ARAIM is being proposed for future LPV-200 (Localizer Performance with Vertical guidance) operations. Extension of current single frequency Inertial-based ABAS standards to dual frequency, multi-

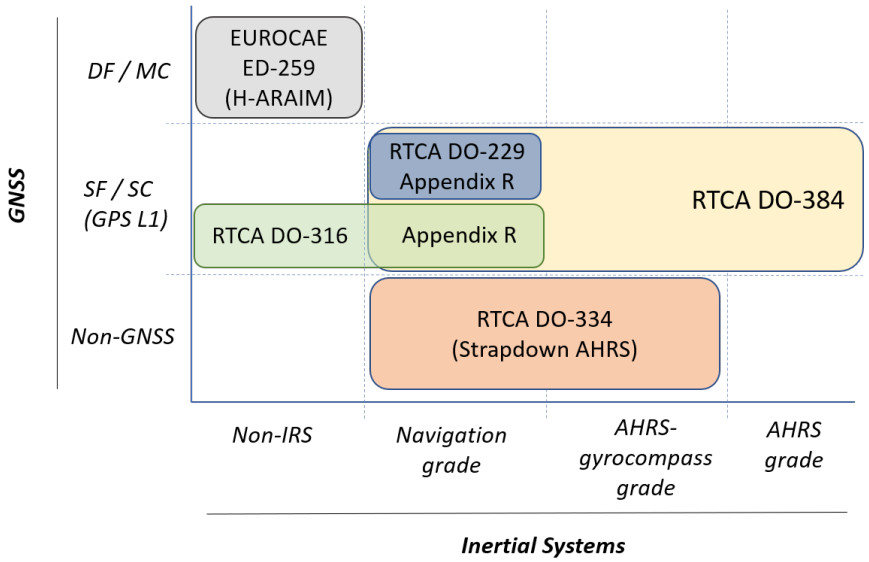

Figure 2.2: Current ABAS and inertial systems related MOPS

constellation is also expected to be included in the future to guarantee continuity and possibly achieve higher performance levels.

This thesis supports the design of Dual Frequency, Multi-Constellation GNSS/INS Integrity monitoring by accounting for the impact of uncertainties in error modeling (specifically time-correlation) in the design of an algorithm that guarantees integrity.

2.3 (Advanced) Receiver Autonomous Integrity Monitoring

2.3.1 GNSS Measurements

Nowadays, receivers of satellite-based navigation can rely in different constellations, signals and services. Modernized Global Positioning System (GPS) transmits three signals: L1/L1C on 1575.42 MHz frequency, L2/L2C on 1227.6 MHz and L5 on 1176.45 MHz. The European Galileo system provides with its Open Service (OS) signals on the E1 band centered on 1575.42 MHz, E5a on 1176.45 MHz and E5b on 1207.14 MHz. Civil aviation uses only protected frequency bands by the Aeronautical Radionavigation Service (ARNS) [10]. For the consideration on this thesis dual-frequency multi-constellation GPS and Galileo are considered with their interoperable frequencies L1/E1 and L5/E5a. At these frequencies GNSS receivers are able to compute for each of the satellites by CDMA multiplexing a code-phase measurement (also called pseudorange) and carrier-phase measurement. Due to the Signal-in-Space (SiS) transmission and de-synchronization of receiver, satellite and system, the code ρ and carrier-

phase ϕ measurements can be modelled for satellite i, constellation j at frequency f and time t as:

$$\rho_t^{i,j,f} = ||\mathbf{x}_{t-\beta}^i - \mathbf{x}_{u,t}|| + c\left(dt_{u,t}^j - dt_{t-\beta}^i\right) + dI_t^{i,f} + dT_t^i + B_{u,\rho}^{j,f} - B_\rho^{i,f} + mp_{\rho,t}^{i,f} + \epsilon_{\rho,t}^i, \tag{2.2}$$

$$\phi_t^{i,j,f} = ||\mathbf{x}_{t-\beta}^i - \mathbf{x}_{u,t}|| + c\left(dt_{u,t}^j - dt_{t-\beta}^i\right) - dI_t^{i,f} + dT_t^i + B_{u,\phi}^{j,f} - B_\phi^{i,f} + N_\phi^i + mp_{\phi,t}^{i,f} + \epsilon_{\phi,t}^i. \tag{2.3}$$

where:

$\|\|\mathbf{x}^i - \mathbf{x}_u\|\|$	True range satellite-user [m],
$\mathbf{x}^i$	Vector of satellite position in ECEF [m],
$\mathbf{x}_u$	Vector of user position in ECEF [m],
c	Speed of light [m/s],
dt^i	Satellite clock offset [s],
dt_u	Clock bias of the receiver [s],
dI	Ionospheric delay [m],
dT	Tropospheric delay [m],
B_u	Receiver instrumental (hardware) delay [m],
B^i	Satellite instrumental (hardware) delay [m],
N_ϕ	Carrier-phase ambiguity term [m],
mp	Multipath [m]
β	Signal travel time (different for each satellite i) [s],
ϵ	residual Gaussian noise [m].

Satellite positions and clock offsets are computed based on the broadcast navigation message. Tropospheric errors can be partially corrected by standard models [7]. For single-frequency users, ionospheric errors can be partly compensated with atmospheric models and based on parameters in the navigation message (e.g. Klobuchar [11] or NeQuick [12], [13] model). The instrumental errors on the satellite can be considered when computing the satellite clock offset and the receiver instrumental errors can be incorporated as part of the (unknown) user clock bias. The residual error after correction of these errors and computation of satellite position and clock as well as the rest of uncorrected residual errors must be accounted for as error model uncertainty.

Because ionospheric errors are potentially large, the most difficult to predict and because these errors are frequency dependent, multi-frequency users can compensate for them by creating the so called *ionospheric-free* combination of two measurements from two frequencies f_1 and

f_2 [14]:

$$\rho_{\mathrm{IF}}^{f_1} = \frac{f_1^2}{f_1^2 - f_2^2}\rho^{f_1} - \frac{f_2^2}{f_1^2 - f_2^2}\rho^{f_2}, \tag{2.4}$$

$$\phi_{\mathrm{IF}}^{f_1} = \frac{f_1^2}{f_1^2 - f_2^2}\phi^{f_1} - \frac{f_2^2}{f_1^2 - f_2^2}\phi^{f_2}. \tag{2.5}$$

The resulting code and phase measurements contains however larger noise levels due to the combination of the original measurement noises and the factors $\frac{f_1^2}{f_1^2-f_2^2}$ and $\frac{f_2^2}{f_1^2-f_2^2}$. For instance, for a E1/E5a ionospheric-free combination, these factors are approximately 2.26 and 1.26 respectively. In order to mitigate this additional level of noise ARAIM use the carrier-phase to smooth the ionospheric-free code measurement with a carrier-smoothing filter, also known as *Hatch filter* (named after R. Hatch) [15].

2.3.2 Multi-Constellation Positioning

In multi-constellation positioning, the GNSS receiver typically needs to solve for unknowns in the 3D position as well as for receiver clock offsets for each of the employed GNSS constellations. For positioning with Galileo and GPS, the parameter vector is:

$$\mathbf{x} = \begin{bmatrix} x & y & z & b_{\mathrm{u}}^{\mathrm{Gal}} & b_{\mathrm{u}}^{\mathrm{GPS}} \end{bmatrix}^{\mathrm{T}}, \tag{2.6}$$

where x, y, z are the position coordinates in the Earth-Centered, Earth-Fixed (ECEF) coordinate frame and $b_{\mathrm{u}}^{\mathrm{Gal}}$, $b_{\mathrm{u}}^{\mathrm{GPS}}$ are the receiver clock bias in meters with respect to the Galileo and GPS constellations respectively. The pseudorange (or carrier-smoothed pseudorange) is nonlinear with respect to the user position and a linearization step is normally necessary. The linearized measurement model can be described as:

$$\mathbf{z} = \mathbf{H}\Delta\mathbf{x} + \boldsymbol{\epsilon}, \tag{2.7}$$

where $\mathbf{z}$ is the vector of linearized pseudorange measurements for all satellites in view, $\mathbf{H}$ is the geometry matrix containing the line-of-sight vectors for each of the satellites, $\Delta\mathbf{x}$ is the parameter difference with respect to the linearization point and $\boldsymbol{\epsilon}$ contains all the errors which

are not corrected. The geometric matrix can be expressed as:

$$\mathbf{H} = \begin{bmatrix} \mathbf{u}^{1,\mathrm{Gal}} & 1 & 0 \\ \mathbf{u}^{2,\mathrm{Gal}} & 1 & 0 \\ \vdots & \vdots & \vdots \\ \mathbf{u}^{n_{\mathrm{Gal}},\mathrm{Gal}} & 1 & 0 \\ \mathbf{u}^{1,\mathrm{GPS}} & 0 & 1 \\ \mathbf{u}^{2,\mathrm{GPS}} & 0 & 1 \\ \vdots & \vdots & \vdots \\ \mathbf{u}^{n_{\mathrm{GPS}},\mathrm{GPS}} & 0 & 1 \end{bmatrix}, \tag{2.8}$$

where $\mathbf{u}^{i,j}$ is the unit line of sight vector pointing from the user to satellite i of constellation j and here n_{Gal} and n_{GPS} are the number of visible Galileo and GPS satellites respectively. The linearized measurement equation is solved via least-squares as [16]:

$$\Delta\hat{\mathbf{x}} = (\mathbf{H}^{\mathrm{T}}\mathbf{H})^{-1}\mathbf{H}^{\mathrm{T}} \cdot \mathbf{z}. \tag{2.9}$$

The vector of corrected measurements follows a non standard Gaussian distribution with a diagonal covariance $\mathbf{R}$ described by the residual error model uncertainties. This is typically taken into account to weight the measurements in a weighted least-squares (WLS) [17]:

$$\Delta\hat{\mathbf{x}} = \underbrace{(\mathbf{H}^{\mathrm{T}}\mathbf{W}\mathbf{H})^{-1}\mathbf{H}^{\mathrm{T}}\mathbf{W}}_{\mathbf{S}_{\mathrm{LS}}}\mathbf{z}, \tag{2.10}$$

where the weight matrix is obtained normally from the covariance matrix as $\mathbf{W} = \mathbf{R}^{-1}$. For the estimator $\mathbf{S}_{\mathrm{LS}}$ the expected error covariance $\mathbf{P}_{\mathrm{LS}}$ of the computed position and clock biases can be obtained with:

$$\mathbf{P}_{\mathrm{LS}} = \mathbf{S}_{\mathrm{LS}}\mathbf{R}\mathbf{S}_{\mathrm{LS}}^{\mathrm{T}} = (\mathbf{H}^{\mathrm{T}}\mathbf{R}^{-1}\mathbf{H})^{-1}. \tag{2.11}$$

2.3.3 Integrity Monitoring Fundamentals

The integrity of the GNSS system could be guaranteed in the absence of faults by evaluating the expression in Equation (2.1) with the estimated covariance matrix in Equation (2.11). In this situation, if the residual error models (i.e. variances) considered in the measurements covariance $\mathbf{R}$ overbounds the underlying real error covariance, integrity can be properly quantified. Unfortunately, in reality, the presence of faults breaks this previous error assessment assumptions. Moreover, error models might be difficult to be obtained precisely or be too conservative

to be considered as constant for all situations. Because of these reasons, GNSS positioning is augmented with Receiver Autonomous Integrity Monitoring (RAIM) or Advanced RAIM. These algorithms consider possible faults and implement mechanisms for their detection (and exclusion). The integrity risk expression in Equation (2.1) can be modified to take into account the presence of monitors in the following general way:

$$P_{HMI} = P\left(|e| > AL, q < T\right). \tag{2.12}$$

where here q is the test statistic of a monitor and T its associated threshold. The probability of hazardous misleading information is the probability of the error being larger than the alert limit while the monitors have not detected a fault. In the case of a detected fault, if the system is declared unavailable, this does not affect integrity. The design of GNSS ABAS contains therefore two important aspects: a set of error model parameters and a fault detection (and exclusion) mechanism. The legacy RAIM is widely used for predicted availability and monitoring based on single frequency, GPS constellation. Because of the single frequency operation, GPS error models consider a relatively large variance model to cover for ionospheric residual error [18]. Moreover, since only one constellation is considered, larger errors are expected due to limited geometric (dilution of precision) aspects. For fault detection and exclusion, RAIM implements a χ^2 test based on pseudorange residuals [19]:

$$\mathbf{r} = \mathbf{z} - \mathbf{H}\hat{\mathbf{x}} = (\mathbf{I} - \mathbf{H}\mathbf{S}_{LS})\mathbf{z}. \tag{2.13}$$

The test is built as a quadratic test on the residuals $\mathbf{r}$:

$$q_r = \mathbf{r}^T\mathbf{R}^{-1}\mathbf{r}. \tag{2.14}$$

In the fault-free case (H0 hypothesis), the test q_r follows a central χ^2 distribution with $n-m$ degrees of freedom $q_{r,H0} \sim \chi^2(n-m,0)$, where n is the number of visible satellites and m the number of unknowns. In the case of fault, the test follows a non-central χ^2 distribution with λ^2 non-central parameter $q_{r,H1} \sim \chi^2(n-m,\lambda^2)$ [19]. A suitable threshold for the test can be obtained from the continuity requirement imposing a certain probability of false alarm to the test:

$$P(q_r \geq T|H_0) \leq P_{fa}. \tag{2.15}$$

RAIM assumes fault in single satellite and supports non-precision approaches. The operation of RAIM includes pre-flight availability prediction [20] and onboard fault monitoring.

ARAIM takes benefits of the GNSS modernisation programs that include the use of new frequencies and new constellations for the use in aviation. ARAIM is designed as a first step to

support en-route down to non-precision approaches including RNP 0.1 capability by means of Horizontal ARAIM (H-ARAIM). As a next goal ARAIM targets LPV-200. This will be achieved with Vertical ARAIM (V-ARAIM) [21]. In the case of ARAIM, contrary to RAIM, the error and threat model is provided to the airborne receiver via the Integrity Support Message (ISM) [4]. This allows to achieve better performance and to adapt in case it is determined necessary. The ISM parameters are computed by a ground infrastructure that monitors the constellation performance and satellite signals [22]. In particular, ISM provides information about the probability of satellite and constellation faults and the error model for the signal in space. Based on those parameters, the integrity evaluation can be done by defining a set of fault hypothesis, their probability and using the law of total probability [23]:

$$\mathrm{P_{HMI}} = \sum_{h=0}^{\mathrm{N}_h} \mathrm{P}(|e^h| > \mathrm{AL}, |q^h| < \mathrm{T}^h | \mathrm{H}_h) \mathrm{P}_h \leq \mathrm{IR_{req}} - \mathrm{P_{NM}}, \tag{2.16}$$

where P_h is the prior probability of a fault hypothesis, $\mathrm{IR_{req}}$ is the integrity requirement and $\mathrm{P_{NM}}$ is the total probability of non-monitored hypothesis (typically residually small). The monitoring in ARAIM is based on a batch of solution separation (SS) test statistics, which are specifically tailored to specific fault mode hypothesis h. The SS test is performed at the position level in a desired dimension l (i.e. vertical, horizontal) by comparing a position solution with the available satellites in view with one obtained with a subset of them:

$$q_l^h = |\hat{x}_l^0 - \hat{x}_l^h|, \tag{2.17}$$

where $\hat{x}^0$ indicates the full-in-view solution. The threshold can be obtained from the significance level of a cumulative Gaussian distribution for the assigned probability of false alarm $\mathrm{P_{fa}}$ and the associated solution separation uncertainty:

$$\mathrm{T}_l^h = \mathrm{Q}^{-1}\left(\frac{\mathrm{P_{fa}}}{2\mathrm{N}_h}\right)\sigma_{ss,l}^h \tag{2.18}$$

where $\sigma_{ss,l}^{h^2} = \boldsymbol{\varepsilon}_l^{\mathrm{T}}(\mathbf{P}^h - \mathbf{P}^0)\boldsymbol{\varepsilon}_l$. The matrix $\mathbf{P}^h$ is the covariance matrix of each of the subset solutions and $\boldsymbol{\varepsilon}_l$ is used to extract the variance in the desired dimension l. The multiple hypothesis solution separation (MHSS) algorithm is the basis for the protection level computation used in this thesis for the GNSS/INS integrity monitoring.

2.4 Aircraft Autonomous Integrity Monitoring

The second type of ABAS system makes use of additional sensors (other than GNSS) that are available onboard an aircraft. Typical sensors include altimeters (barometric or radar), magnetometer-compass and inertial systems. For instance, barometric altimeters are widely

used to support flight level aircraft separation and to enable certain Baro-VNAV operations [24]. They are also typically coupled with an Inertial Reference System (IRS) in to the so called Air Data Inertial Reference System (ADIRS). This section focuses on the inertial systems and its use for navigation integrity.

2.4.1 Inertial Navigation System

An Inertial Navigation System (INS) is composed of an Inertial Measurement Unit (IMU) measuring 3D specific forces and 3D angular velocities and a strapdown computer that integrates those measurements to obtain attitude, velocity and position. Due to the imperfection of initial attitude and the error processes in the IMU sensors, the integrated solution will experience an accumulated or growing error over time. The differential equations that drive the strapdown inertial navigation system can be summarized for a local navigation frame n as:

$$\begin{bmatrix} \dot{\mathbf{p}}^n \\ \dot{\mathbf{v}}^n \\ \dot{\mathbf{C}}_b^n \end{bmatrix} = \begin{bmatrix} \mathbf{D}^{-1}\mathbf{v}^n \\ \mathbf{C}_b^n\mathbf{f}^b - (2\boldsymbol{\Omega}_{ie}^n + \boldsymbol{\Omega}_{el}^n)\mathbf{v}^n + \mathbf{g}^n \\ \mathbf{C}_b^n(\boldsymbol{\Omega}_{ib}^b - \boldsymbol{\Omega}_{in}^b) \end{bmatrix}, \tag{2.19}$$

where $\mathbf{p}^n$, $\mathbf{v}^n$ and $\mathbf{C}_b^n$ stands for position, velocity and the rotation matrix between body and local frame respectively. $\mathbf{D}$ converts from curvilinear (i.e., latitude, longitude, altitude) to cartesian distances. Its inverse $\mathbf{D}^{-1}$ is used therefore to convert from cartesian to curvilinear distances and is defined as:

$$\mathbf{D}^{-1} = \begin{bmatrix} \frac{1}{\mathrm{R_N}+h} & 0 & 0 \\ 0 & \frac{1}{(\mathrm{R_E}+h)\cos(\varphi)} & 0 \\ 0 & 0 & -1 \end{bmatrix}, \tag{2.20}$$

where $\mathrm{R_N}$ is the meridian radius of curvature, $\mathrm{R_E}$ the transverse radius of curvature at a given latitude on the local ellipsoid, φ is the latitude and h is altitude. The vector $\mathbf{f}^b$ contains the measured specific force in the body frame and $\boldsymbol{\Omega}_{ib}^b$ is the skew-symmetric matrix based on the measured angular velocities from the gyroscope, i.e., $\boldsymbol{\Omega}_{ib}^b = [\mathbf{w}_{ib}^b \times]$. The matrix $\boldsymbol{\Omega}_{in}^n = \boldsymbol{\Omega}_{ie}^n + \boldsymbol{\Omega}_{en}^n$ accounts for Earth rotation and transport rate and $\mathbf{g}^n$ is the gravity vector in the local-level frame. The strapdown inertial navigation algorithm that implements Equation (2.19) to compute attitude, velocity and position over time based on the discrete inertial measurements is well known and can be found for instance in [25]–[27].

In civil aviation, aircraft are equipped with single or redundant Inertial Reference System (IRS). IRS refers here to a aviation-grade INS together with the necessary packaging and interfaces for the rest of the aircraft subsystems and able to provide a self-content solution. Thanks to

the low noise levels of accelerometers and especially gyroscopes, the IRS can be initiated on ground while the plane is not moving. The initialization process involves the estimation of biases as well as the attitude and heading of the sensor. Attitude components can be partially estimated using accelerometers by projecting the gravity vector, also known as leveling, while the heading is estimated by sensing the Earth rotation signal in the gyroscopes, which is known as gyrocompassing [28]. The IRS could be also updated with ranging sources or other information during flight to correct the drift over time. The aircraft normally uses different sources of information in its Flight Management System (FMS) and integrates them to finally provide other subsystems and the pilots with the required navigation information. Air Data System (ADS) or a compass magnetic heading are examples of aiding system that can help stabilize the vertical channel and the heading drift.

2.4.2 GNSS/INS Integration

In order to reduce the accumulated error in the INS over time due to residual initialization and sensor errors, the inertial navigation solution is typically combined with measurements from radio-navigation signals. Examples of these are terrestrial signals like Distance Measurement Equipment (DME) [29] or VHF Omnidirectional Range (VOR) [30] and satellite positioning like GNSS.

The combination of INS with GNSS can be done at different integration levels with the following architectures:

- **Uncoupled**: This is the simplest way to combine the INS solution and GNSS information. The two systems are running in parallel and the position and velocity from a GNSS receiver is used to *reset or calibrate* the position and velocity of the INS system [31]. This option is especially suitable for strategical inertial sensors with stable gyroscopes and low time varying biases since these are not estimated online. This integration level offers very limited fault detection and integrity monitoring capability. The system mainly relies on the stability of the INS and the correctness of the GNSS.

- **Loosely-coupled:** In this integration design the solution of the INS is coupled with the position, velocity (and possibly attitude) solution computed by GNSS receivers. The biases of the inertial sensor are estimated which improves the long-term performance of the system. In this level of integration the complexity is relatively low. One disadvantage is that this option offers limited fault-detection capabilities since the GNSS information can only be cross-checked with the INS information at the position level and therefore specific satellites faults cannot be detected within the integrated system.

- **Tightly-coupled:** In this design, the INS solution is integrated directly with raw GNSS

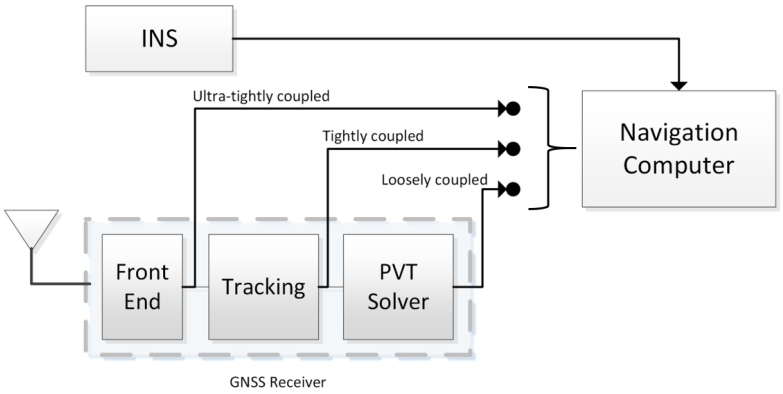

Figure 2.3: GNSS/INS integration levels

observation such as pseudorange, carrier-phase (and eventually Doppler) measurements. The complexity level is higher as compared to the loosely-coupled alternative since GNSS satellite positions, clock corrections and error models for pseudoranges must be taken into account. The main advantage is that, by having access to individual satellite observations, fault detection (and exclusion) mechanisms as well as integrity monitoring strategies can exploit the explicit redundancy between measurements from individual satellites and INS solution.

- **Ultra tightly or deeply-coupled:** This integration level is the most complex one. In this case, the INS solution is combined directly with the raw binary signals of the GNSS receiver (such as I/Q samples). This increment in complexity is normally justified only for high dynamic vehicles where GNSS tracking loops may have difficulties to follow properly the signals or in situations with high level of multipath or interference, where the combination of INS can increase the Carrier-To-Noise (CN0) ratio of the received signals and provide guidance to their tracking. Integrity assessment is quite challenging since it is more difficult to separate the error and risk contributions between systems and signals.

Except for the *uncoupled* option, the integration is often performed by using an Extended Kalman filter (EKF). The different integration levels are also depicted in Fig. 2.3 with respect to the information obtained from the GNSS receiver for the navigation filter. In aircraft, this is traditionally done by the FMS, but possibly also directly in the IRS system [32].

An EKF is a sequential estimator for nonlinear systems that propagates over time the desired states of interest along with their estimated covariances. Let us take a general nonlinear

discrete-time system:

$$\mathbf{x}_k = f(\mathbf{x}_{k-1}) + \mathbf{G}_k \mathbf{w}_k, \tag{2.21}$$

$$\mathbf{z}_k = h(\mathbf{x}_k) + \mathbf{J}_k \mathbf{v}_k, \tag{2.22}$$

where $\mathbf{x}$ is the state vector, $\mathbf{w}$ the process noise, $\mathbf{v}$ measurement noise, $f()$ is the nonlinear propagation function, $h()$ is the nonlinear measurement function and $\mathbf{G}$ and $\mathbf{J}$ projects the process or measurement noise into the states or measurements, respectively. The EKF equations are well known and are here presented for convenience [33]:

Prediction :

$$\mathbf{x}_{k|k-1} = f(\mathbf{x}_{k-1|k-1}), \tag{2.23}$$

$$\mathbf{P}_{k|k-1} = \mathbf{F}_k \mathbf{P}_{k-1|k-1} \mathbf{F}_k^{\mathrm{T}} + \mathbf{G}_k \mathbf{Q}_k \mathbf{G}_k^{\mathrm{T}}, \tag{2.24}$$

Update :

$$\mathbf{K}_k = \mathbf{P}_{k|k-1} \mathbf{H}_k^{\mathrm{T}} \left(\mathbf{H}_k \mathbf{P}_{k|k-1} \mathbf{H}_k^{\mathrm{T}} + \mathbf{J}_k \mathbf{R}_k \mathbf{J}_k^{\mathrm{T}} \right)^{-1}, \tag{2.25}$$

$$\mathbf{x}_{k|k} = \mathbf{x}_{k|k-1} + \mathbf{K}_k \left(\mathbf{z}_k - h(\mathbf{x}_{k|k-1}) \right), \tag{2.26}$$

$$\mathbf{P}_{k|k} = (\mathbf{I} - \mathbf{K}_k \mathbf{H}_k) \mathbf{P}_{k|k-1}, \tag{2.27}$$

where $\mathbf{x}_{k|k-1}, \mathbf{P}_{k|k-1}$ are the predicted mean and covariance of the states, $\mathbf{Q}$ is the process noise covariance, $\mathbf{R}$ is the measurement noise covariance, $\mathbf{K}$ is the Kalman gain and $\mathbf{x}_{k|k}, \mathbf{P}_{k|k}$ are the aposteriori mean and covariance values of the states. The state transition and observation matrices $\mathbf{F}$ and $\mathbf{H}$ respectively, are defined as the following Jacobians:

$$\mathbf{F} = \frac{\partial f(\mathbf{x}_{k-1|k-1})}{\partial \mathbf{x}}, \text{ and } \mathbf{H} = \frac{\partial h(\mathbf{x}_{k|k-1})}{\partial \mathbf{x}}. \tag{2.28}$$

As it can be seen in the previous equations, the EKF is divided in two main steps, *prediction*, where dynamic error models are applied to propagate the states in time and *update*, where new observations are included into the estimation process.

From different Kalman filter implementations, the most common one employed in the GNSS/INS integration is the so called error-state (also known as indirect) Kalman filter. Within this scheme, instead of determining directly the absolute position, velocity and attitude of the vehicle, the KF estimates the error contained in the INS system. The full integrated solution is then extracted from the INS corrected by the KF states.This minimizes linearization errors and achieves better estimation of state and covariance [34]. In fact, this design allows to work mainly in the linear domain of the system. This is used to simplify the assessment of the error propagation within the estimator in Chapter 4 and 5. Based on that, a general linear dynamic system (LDS) is considered in Chapter 4 and Chapter 5 and the Kalman filter will be mentioned instead of Extended Kalman filter.

Within the error-state EKF approach, there are two possible choices for architecture design. Since the EKF estimates the error of the INS, the final integrated solution must consider the total magnitude corrected by the estimated error. Depending on the strategy to correct this error, two alternatives exists:

- **Open-loop**: It is also known as *feed-forward* filter. The INS solution is corrected by the error estimated by the EKF before providing the final integrated solution but is not feed-back to the strapdown inertial navigator. This approach has the advantage that INS, GNSS and EKF propagate information only in a forward direction, making the INS system independent from the EKF. Since the EKF contains the accumlated errors of the INS, this architecture is suitable only for inertial sensors of good quality and over a certain operation time. If the error states in the EKF become too large, the linearization errors are no longer negligible and can make the filter diverge.
- **Close-loop**: It is also known as *feed-backwards* filter. In this architecture design the error states are used to *calibrate* the INS position, velocity and attitude periodically. The main advantage is that the error states are always kept close to zero within the EKF, and therefore in a linear domain. The disadvantage is that a connection from the EKF to the INS is necessary, increasing potentially the complexity and interdependence within the system.

In this research, the integration level and architecture design that is considered is the tightly-coupled close-loop error state. From the different strategies, this configuration provides on one hand best situation for error propagation assessment, fault-detection and integrity monitoring. On the other hand, it guarantees good linearization performance and it can be applied over a wider range of inertial sensors and operational times. The specific implementation for GNSS/INS integration is revisited in detail in Chapter 6.

2.4.3 Kalman filter Fault Detection and Integrity Monitoring

The Kalman filter is minimum variance (unbiased) estimator and therefore, in the presence of measurement faults it does not provide any integrity assurance by itself. Therefore, as it was the case for (A)RAIM, KF must be accompanied by some monitors to protect against fault modes. Appendix R in [6], [7] and [8] provide some typical algorithms that can achieve the monitoring of faults in tightly-coupled GPS/INS systems. Most approaches are based on the following main methods for KF fault detection:

- **Innovation-based**: The KF innovation sequence can be used to detect either sudden changes in the measurements and possibly also slowly growing errors [35]–[38]. The

innovation vector is obtained at each update step from the difference between real and predicted measurement as in Equation (2.26):

$$\boldsymbol{\gamma}_k = \mathbf{z}_k - \mathbf{H}_k \mathbf{x}_{k|k-1}, \tag{2.29}$$

with an associated covariance matrix:

$$\mathbf{P}_\gamma = \mathbf{H}_k \mathbf{P}_{k|k-1} \mathbf{H}_k^{\mathrm{T}} + \mathbf{R}_k. \tag{2.30}$$

This vector can be used to screen for possible large deviations of measurement with respect to predictions before the actual update is performed. It can also be used as a quadratic test, similar to RAIM to detect faults:

$$q_\gamma = \boldsymbol{\gamma}^{\mathrm{T}} \mathbf{P}_\gamma^{-1} \boldsymbol{\gamma}. \tag{2.31}$$

The test follows a central or non-central χ^2 distribution with n degrees of freedom in the fault-free or faulty situation, respectively. This can be extended to consider multiple epochs by summing the different tests over time. Although this provides sensitivity to ramp-type faults, over time the detection capability also decreases if large time spans are considered. Methods to evaluate integrity risk for the sum of innovation squared tests has been proposed by the authors in [35], [36] which involve the parallel calculation of worst-case fault profiles.

- **KF aposteriori residuals**: It is also possible to build a quadratic test with the aposteriori residuals of the KF to evaluate integrity [39]:

$$\mathbf{r}_k = \mathbf{z}_k - \mathbf{H}_k \mathbf{x}_{k|k}. \tag{2.32}$$

  However, the test statistics are more difficult to handle since they follow a generalized χ^2 distribution which does not have analytical solutions to evaluate its Cumulative Density Function (CDF). In some situations it could nevertheless provide better fault detectability for a GNSS/INS system [37].

- **Solution Separation**: By considering a bank of Kalman filters with different fault hypothesis each of them, solution separation test can be performed similarly as in ARAIM. This was introduced by [40], [41] and they are included in different practical solutions [32], [42].

Table 2.2 summarizes the main fault detection approaches. Other approaches to perform monitoring of the GNSS/INS exist, in same cases by modifying or combining some of the previous ones or by extending them to perform exclusion [43]–[48].

	KF Innovation-based	**Residual-based**	**Solution Separation**
Domain	Range	Range	Position
Base Magnitude	Innovation vector: $\boldsymbol{\gamma}_k = \mathbf{z}_k - \mathbf{H}_k \mathbf{x}_{k\|k-1}$	Residual vector: $\mathbf{r}_k = \mathbf{z}_k - \mathbf{H}_k \mathbf{x}_{k\|k}$	Position subsets: $\hat{x}^h$
Test Statistic	$q_\gamma = \boldsymbol{\gamma}^{\mathrm{T}} \mathbf{P}_\gamma^{-1} \boldsymbol{\gamma}$	$q_r = \mathbf{r}^{\mathrm{T}} \mathbf{R}^{-1} \mathbf{r}$	$q_{ss}^h = \lvert \hat{x}^0 - \hat{x}^h \rvert$
Test Statistic Distribution	Chi-Squared: $q_\gamma \sim \chi^2 \left(\lambda^2, n \right)$	Generalized Chi-Squared [49]: $q_r = \sum_i \alpha_i^2 \chi_i^2$	Gaussian: $q_{ss}^h = \mathcal{N}(\mu, \sigma_{ss}^{h^2})$

Table 2.2: Kalman Filter Fault Detection Approaches

3 Stochastic Error Modeling and Bounding

This chapter provides additional background on the time-correlated stochastic processes used for modeling sensor noise in Linear Dynamic Systems (LDS) estimators and in particular the Kalman filter. Then, it states the problematic of bounding estimation errors so that it can account for uncertainties of stochastic parameters describing these models by reviewing the current state of the art in this field.

3.1 Stochastic Error Identification and Modeling Techniques

Stochastic errors in navigation sensor measurements can be considered as a time series. Their stochastic nature may be caused by different factors. Although different models exist that can be associated to specific (and empirically observed) physical processes, the total error of a certain measurement normally contains the additive contribution of multiple process models. As an example, Fig. 3.1 shows time series realizations of stochastic observation errors modeled as a different combination of Gaussian noise (WGN) and Gauss-Markov Processes (GMP).

Therefore, in order to model the stochastic behaviour of a certain observation, there are typically 3 necessary steps: isolation, identification and model-parameter determination. First, it is necessary to isolate the error signal (i.e., time series) from the information part of the measurement (and possibly from other errors or factors). Then, it is important to identify which type of stochastic processes might be present in the error signal (i.e., structure). Once those processes are identified, model-parameters needs to be found.

The error isolation process highly depends on the sensor or technology under consideration. For instance, in order to isolate GNSS local multipath, Code-minus-Carrier (CMC) technique can be used [50]. Isolating satellite clock and ephemeris errors may require processing information from multiple ground stations [23], similarly to isolating tropospheric errors [51]. Isolating the error signals in inertial sensors can be done by recording measurements in a

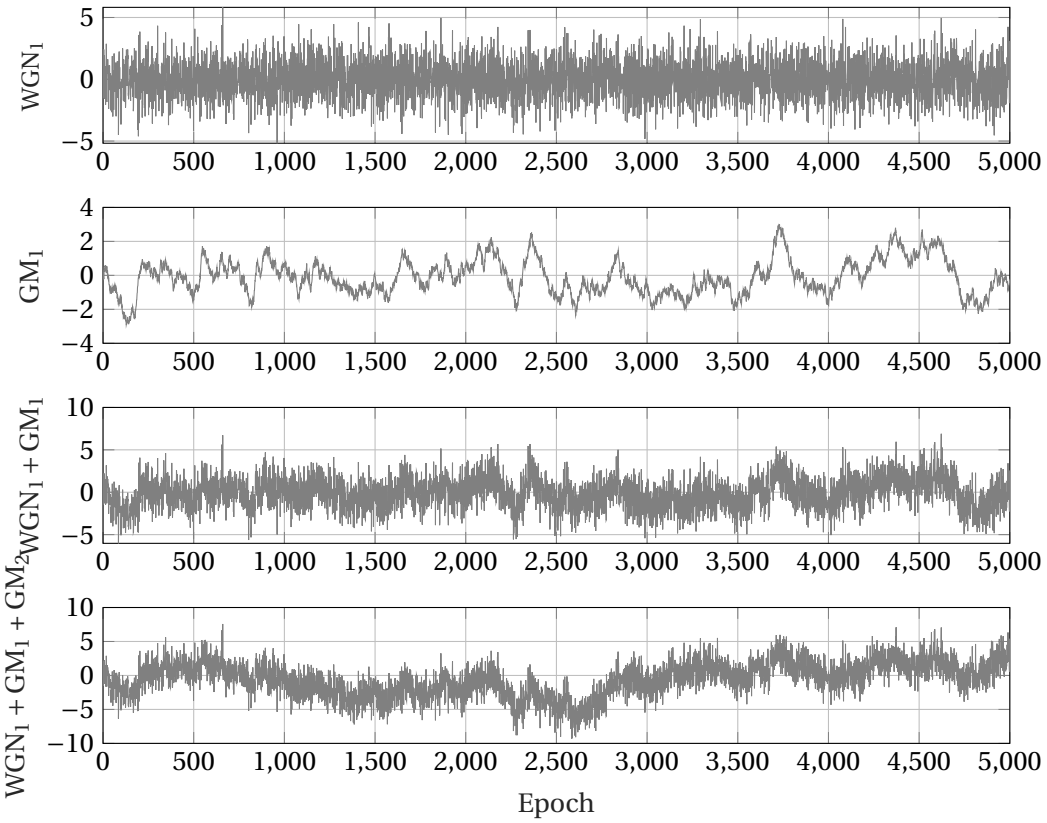

Figure 3.1: Example of different stochastic processes. $\mathrm{WGN}_1 \sim \mathcal{N}(0, 1.5^2)$, $\mathrm{GM}_1 \sim \mathcal{GM}(1,100)$, $\mathrm{GM}_2 \sim \mathcal{GM}(4,1000)$ and their combination.

controlled (e.g., static) scenario [52]. For the identification and modeling, different techniques or domains exist that can be used to analyse the time series signals. The most used ones are presented in the following.

3.1.1 Autocovariance Function

The autocovariance of a certain signal R_a is a function that provides the covariance of a process with itself at two different time instants expressed as:

$$R_a(t_1, t_2) = \mathrm{Cov}[a_{t_1}, a_{t_2}] = \mathrm{E}\left[(a_{t_1} - \mathrm{E}[a_{t_1}])(a_{t_2} - \mathrm{E}[a_{t_2})\right], \tag{3.1}$$

where E is the expectation operator and t_1, t_2 are arbitrary sampling times. If the process a is stationary, its probability density function is invariant with time and the autocovariance matrix only depends on the time differences $\Delta t = t_2 - t_1$ [53]. Equation (3.1) can be thus

written as:

$$R_a(t_1, t_2) = R_a(t_1, t_1 + \Delta t) = R_a(0, \Delta t) = R_a(\Delta t) \tag{3.2}$$

which results in:

$$R_a(\Delta t) = \mathrm{E}\left[a_0 a_{\Delta_t}\right] - \mathrm{E}[a]^2 \tag{3.3}$$

In some situations, a normalized version of the autocovariance is used to analyse purely the correlation level of the signal. The normalized autocovariance function is called *autocorrelation* function and it is defined for an stationary process as:

$$\bar{R}_a(\Delta t) = \frac{R_a(\Delta t)}{\sigma_a^2} = \frac{\mathrm{E}\left[a_0 a_{\Delta_t}\right] - \mathrm{E}[a]^2}{\sigma_a^2}, \tag{3.4}$$

where σ_a^2 is the variance of the signal. Please note that in some literature the nomenclature autocorrelation and autocovariance are used interchangeably or the term autocorrelation is used to refer to the autocovariance (without normalization). In this research, the term autocovariance is preferred to keep explicitly in mind that the variance levels are included, being an essential factor when talking about error bounding.

For a time series vector **a**, it is useful to define the autocovariance matrix (ACM), which is a square matrix with the autocovariance function of the signal at the different time interval lags:

$$\mathbf{R}_\mathrm{a} = \mathrm{E}\left[(\mathbf{a} - \mathrm{E}[\mathbf{a}])(\mathbf{a} - \mathrm{E}[\mathbf{a}])^\mathrm{T}\right]. \tag{3.5}$$

The ACM is a symmetric and positive semidefinite matrix. Illustratively, Fig. 3.2 provides the theoretical autocovariance functions of the examples processes in Fig. 3.1.

3.1.2 Power Spectral Density

Instead of analysing a signal in the time domain with the autocovariance function, the frequency behaviour of a process provides important information about its characteristics. In fact, for stationary processes there is an important relationship between the autocovariance function and its Fourier transform [53]:

$$S_a(j\omega) = \int_{-\infty}^{\infty} R_a(\tau) e^{-j\omega\tau} d\tau. \tag{3.6}$$

$S_a(j\omega)$ is known as the power spectral density (PSD) of the process. When a process is composed of different types of noises, it may be difficult to identify them with their parameters in the time domain or via the empirical autocovariance function. Instead, the noise com-

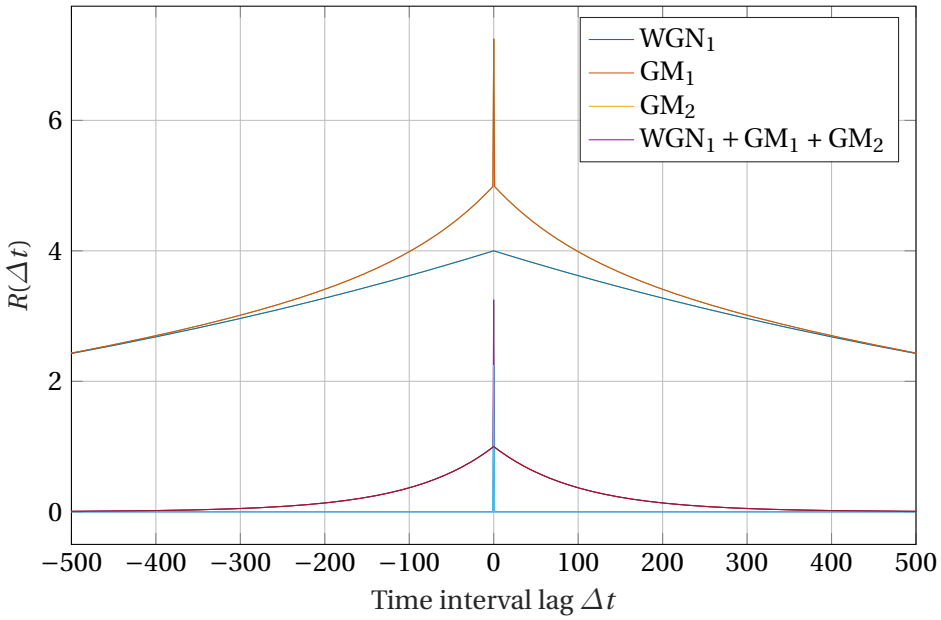

Figure 3.2: Example of theoretical autocovariance functions for different stochastic processes. WGN$_1 \sim \mathcal{N}(0, 1.5^2)$, GM$_1 \sim \mathcal{GM}(1, 100)$, GM$_2 \sim \mathcal{GM}(4, 1000)$

ponents may have different frequency behaviour and the PSD can be used to identify them easier [54]. In practice, PSD are represented by a discrete Fourier Transform (DFT) which is estimated from discrete samples of signals with some type of fast Fourier Transform (FFT) like periodograms, Barnett's or Welch's method for instance [55]. The frequency domain analysis is exploited in Chapter 4 and 5 to derive new tight bounds for Gauss-Markov models with uncertain parameters.

3.1.3 Allan Variance

The Allan Variance (AV) is a mathematical tool widely used for the identification and modelling of stochastic error processes in different electrical systems like atomic clocks [56] or inertial sensors [52], [54]. It is a two sample variance and provides information about the variance level of the process at different averaged time intervals. It is very helpful for the identification of different types of noises when the shape and slope each of them are distinct within AV plot. Fig. 3.3 depicts the representation of different processes in the Allan deviation (squared-root of Allan variance) as taken from IEEE standards [54]. The Allan variance is related to the PSD by the integral:

$$\sigma^2_{\mathrm{AV}}(\Delta t) = 2\int_0^\infty S(f)\frac{\sin^4(\pi f \Delta t)}{(\pi f \Delta t)^2}df. \tag{3.7}$$

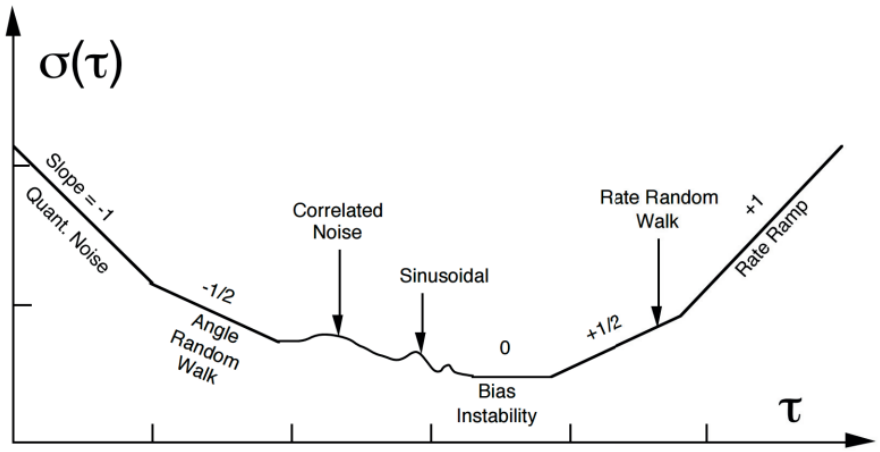

Figure 3.3: Stochastic processes representation in Allan Variance domain. Source: IEEE [54]

Although the AV is quite useful for the identification of processes, inferring the model parameters from AV plots via regression is problematic for composed stochastic processes (i.e., processes with partially overlapping spectrum). This is because there is not in general an unique solution for the inverse function of Equation (3.7), which leads to spectral ambiguity [57].

3.1.4 Wavelet Variance

The Wavelet Variance (WV) can be interpreted as the variance of a process after it has been subject to an approximate bandpass filter [58]. For a Haar wavelet, the WV is proportional to the Allan variance up to a constant scale factor while much faster to evaluate [59]. The identification of processes is therefore similar as with the AV but with additional advantage in process parameter determination. Notably, a framework based on the Generalized Method of Wavelet Moments (GMWM) has been developed that support an efficient, optimal and stable parameter estimation for composed stochastic processes [58] and it has been used for the identification of noise structure in inertial sensors [60]. The impact of parameter estimation with GMWM on navigation has also been investigated [61]. Its open-source implementation is freely available to the navigation community.

3.2 Uncertainty in Error Modeling

In the previous section different techniques to identify and determine model-parameters of a certain process were presented. However, it is normally impossible to find models and related parameters that would fit perfectly the real physical process at all times. There are

many different reasons for the limitation on the use of models. In the following, the most relevant ones related to this research are listed:

1. **Models are incomplete:** It might not be possible to find a model or combination of models that represent the same behaviour as the empirical data. In some situations, a simple model might be desirable for a certain application even if it does not follow perfectly the physical data to maintain the complexity of the system low. For instance, one might be interested in modelling an error as white Gaussian noise (WGN) although the signal present some level of time-correlation.

2. **Domain of validity:** Models are typically derived from historical data, and therefore it is assumed that the processes will behave similarly in the future, which might not be the case. Other aspect is that the historical data may cover different environment or seasonal conditions, recorded in different time series, which are not possible (or too complex) to be parametrized. The data therefore is not completely stationary or cover different statistical realizations. Moreover, the available data may not cover every single possible future conditions of the data. In this situation, the model must be careful to provide a proper generalization for the intended purpose. For instance, GNSS tropospheric error depends on complex atmospheric conditions with yearly variation.

3. **Data limitations:** Models are obtained with finite number of sample data or time series. This limits the statistical significance of the results depending on the sample size. Also, one is normally interested in building probability densities functions which can only be done based on independent samples, but data may contain partly unmodelled correlation between samples because of the acquisition process. Finally, the error analysis quality may also be limited by measuring equipment. For example, Fig. 3.4 shows the empirical autocovariance function of 50 time series realizations with 5.000 samples of a first-order Gauss-Markov process (GMP) as the one shown in Fig. 3.1, along with its theoretical autocovariance function. In this figure, we can see that modeling different realizations would result in a range of possible parameters associated with GMP.

Independently of the technique that is used to identify suitable models and estimate their parameters from data, it is expected to have some level of uncertainty associated with the estimated parameters caused by incompleteness or fidelity of selected models, range of environment of conditions, dynamics, etc. and limitation in data length and number of realizations.

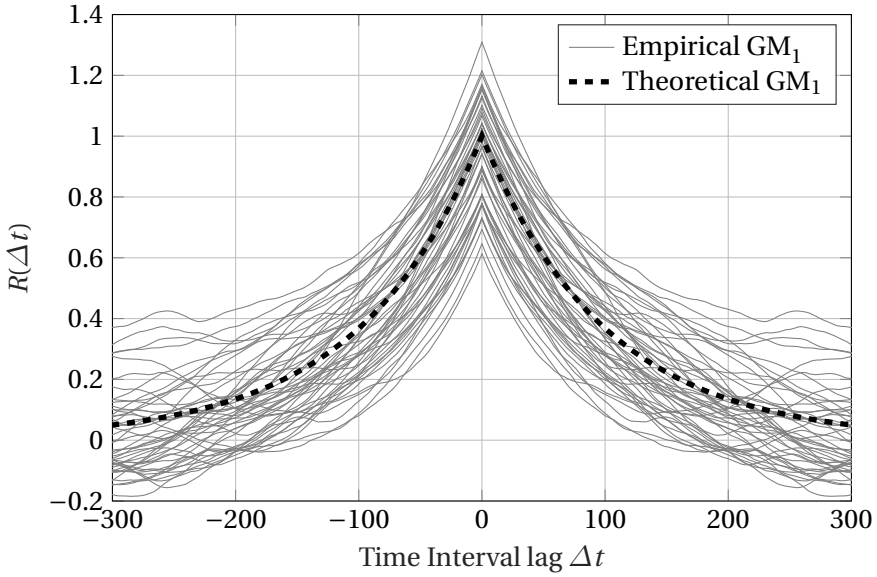

Figure 3.4: Theoretical and 50 empirical autocovariance realizations with 5e3 samples of a Gauss-Markov process. GM$_1 \sim \mathscr{GM}(1,100)$.

3.3 Integrity Risk Bounding and Related Work

Safety-related applications like civil aviation require that navigation system accuracy and integrity risk level are properly quantified. However, as it was introduced in the previous section, it is not possible to derive *exact* models for sensor errors, which makes the quantification of accuracy and integrity risk also uncertain. Therefore, in navigation, the actual error models and distributions are replaced by a (simplified) conservative error model. This process is known as overbounding [62]. For this task, Gaussian distributions are typically chosen due to its simplicity and its properties of being invariant over convolution. For overbounding Gaussian distributions, guaranteeing both accuracy (95% of the error) or evaluating integrity risk (e.g., 10^{-7} for LPV-200) can be done by satisfying bounding conditions of the equivalent standard deviation. Since navigation output is normally provided for several dimensions (e.g., vertical or horizontal), the estimated error joint PDF follows the PDF of a multidimensional Gaussian distribution. Under fault-free conditions, the error covariance matrix of the multidimensional Gaussian error distribution represents the full PDF under linear and unbiased estimators such as the ones considered in this research.

The variance of the error in a certain dimension of interest l can be extracted from the error covariance matrix $\mathbf{P}$ with $\sigma_l^2 = \boldsymbol{\varepsilon}_l^{\mathrm{T}} \mathbf{P} \boldsymbol{\varepsilon}_l$, where $\boldsymbol{\varepsilon}$ is a zero vector with ones only on the indexes positions of interest. Defining $\hat{\sigma}_l^2$ as the estimated variance of the error, the goal to guaranteed that integrity risk is satisfied is that it is larger than the true error variance, that is, $\hat{\sigma}_l^2 \geq \sigma_l^2$.

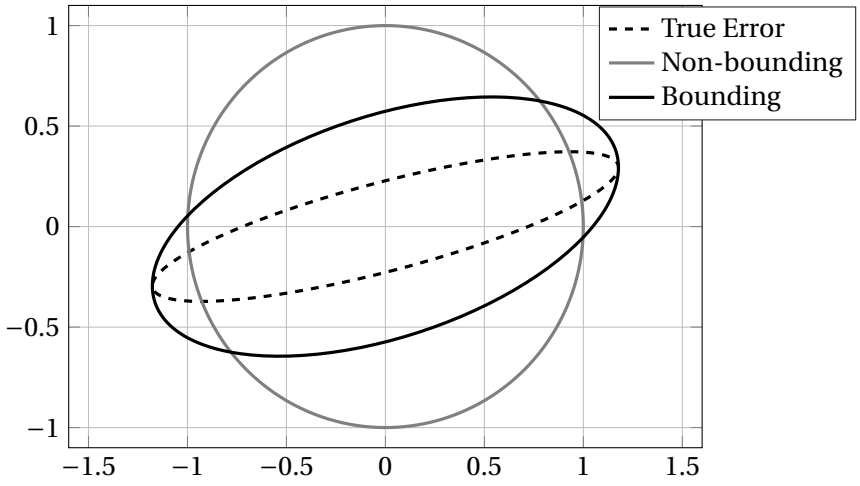

Figure 3.5: Illustration of Covariance Bounding

When it is not practical to evaluate the bounding condition for every dimension separately, the criteria can be generalized to the full covariance matrix, such that $\hat{\mathbf{P}} \geq \mathbf{P}$. The inequality of covariance matrix being *greater or equal* than other is understood as that the difference $\hat{\mathbf{P}} - \mathbf{P}$ being *positive semidefinite*. Figure 3.5 illustrates the bounding/non-bounding criteria for covariance matrices for an example in 2D. Notice that one of the covariances is not bounding the error even though the variances in the main plotting axes (diagonal elements of the covariance) are larger than the true error covariance.

In navigation systems, different concepts to overbound the error estimation with linear estimators have been developed. In [63] an overbounding process to model non-Gaussian error distributions was first proposed. Then, the concept of cumulative distribution function (CDF) overbounding was proposed and revisited by [64], [65]. Further developments included the consideration of asymmetric distributions and possible biases [66], [67]. In most cases, conservative error Gaussian distribution models have to be obtained from empirical distributions with limited and possibly not fully independent sample data. New concepts are developed to account for this aspect by increasing the estimated model variance by an inflation factor based on the so called *number of effective samples* [23]. This has been used to derive conservative models for residual GNSS orbit and clock errors as well as airborne multipath [68]. These methods are however limited to snapshot estimators (like the least-square method used in GNSS point positioning) since the final goal is to obtain a single overbounding probability distribution.

The authors in [69], [70] extended the applicability of overbounding to linear dynamic systems with the concept of spherically symmetric overbounding. This method could theoretically

account for time correlated measurement errors, but its practical usage in Kalman filtering is not clear. Other authors proposed to bound the empirical error time series in the Allan variance domain [71] and the PSD domain [72]. However no proof was given that this process would guarantee correct bounding result. Moreover, in case of spectral ambiguity within AV [57], a general bound likely cannot be guaranteed. Bounding criteria in the frequency domain was recently proven in [73] and [51], and it is also provided in Appendix B and discussed in Chapter 4 and 5. Generally, obtaining conservative models from empirical data is still an open field of research. Most of the error modeling techniques for time series introduced in Section 3.1 are able to provide approximate confidence intervals of model parameters [74]–[76]. However, it is still unclear how a *conservative model* could be obtained taking into account the limitations discussed in Section 3.2. Some recent research in this direction for PSD estimators is [77], [78].

In overbounding approaches frequently used in GNSS, a more conservative model is typically obtained with a larger or inflated variance of the empirical Gaussian distribution. However, for other time correlated models, as it was shown in Section 1.2, a larger value of all the parameters (e.g., time-correlation constant) do not a priori guarantee a conservative model. Instead, a possible range of values in the form of a lower and upper bounds may allow for the derivation of conservative models. This motivates the assumptions and derivations of conservative models in Chapter 4 and 5. Parameter uncertainty has already been considered as assumption in the literature.

In [79], [80] a full summation expression for the Kalman filter was derived as a function of the autocovariance functions (ACF) of the error processes. Based on that the authors were able to select the worst-case ACF value for each of the terms to obtain an estimation bound in case of uncertain but bounded ACFs. The method requires, however, the evaluation of the full time history and becomes unfeasible for real-time systems due to computational and memory limitations. In [81] an approximate bound to the previous approach is proposed with less computational requirements.

Outside the navigation community, the problem of risk/uncertainty quantification under large unaccounted or unclear errors has been also addressed within the robust Kalman filtering literature [82] and the guaranteed cost filtering approach [83]. One example of the last is [84], that provided a solution for GMP with uncertain time correlation for continuous-time filtering. This approach is considered a starting point for the derivation of new bounds in this thesis.

3.4 Kalman filter with Time-Correlated Error Models

The different errors in the GNSS measurements (e.g., code-phase and carrier-phase) and in the Inertial Measurement Unit (IMU) are correlated in time [51], [52], [54], [72], [85]. Navigation computers that aim to estimate position, velocity and time (PVT) by leveraging multiple epochs information at the same time need to account for this fact. Otherwise, the result of neglecting the time-correlation and for instance modelling all the errors as White Gaussian Noise (WGN) would result in wrong estimation [86]. Different type of estimators use multi-epoch measurements, examples of them are state-space estimators like Kalman filters [87], batch least-squares [88], dynamic networks [89] or bundle adjustments [90] also called factor graphs [91]. Without a loss of generality this research focus primary on the use of time-correlated error models within Kalman filter estimation, but this problematic, as well as the solutions provided in this thesis in Chapter 4 and Chapter 5 are applicable to other estimators.

There exist different methods to account for the time-correlation nature of stochastic process or measurement noise in Kalman filtering [92]. The most common approach is based on *state augmentation*, where the state vector is expanded with the correlated time-varying components of such noise, value of which is estimated together with other states. An important pre-requisite for that is the existence of a differential equation (i.e., dynamic model) describing the noise evolution. Based on a state augmented dynamic model a *Schmidt-Kalman* filter provides an alternative implementation that estimates the non-augmented states while still accounting for the effect of the time-correlation (augmented states) [93]. Another approach applicable to correlated observations is to avoid the estimation of several augmented states by *measurement differencing*. This is developed in [94] and revised with application to GNSS in [86]. From the listed approaches, state augmentation provides the most intuitive interpretation since the states are explicitly considered throughout the estimation process. Because of that, this study uses this approach to understand the impact of parameter uncertainties describing time-correlated noise and derives new bounding conditions accounting for such uncertainty. The disadvantages of state augmentation comes when a large number of augmented states are necessary to capture the time correlation, which increments the computational requirements. Another possible problem appears when many of states become totally observable, which can lead to ill-condition matrices used in computing the Kalman gain. In such situation, regularization could be used.

State augmentation can be formulated in the following way. Consider a continuous-time LDS described by a differential equation:

$$\dot{\boldsymbol{\xi}}(t) = \mathbf{F}(t)\boldsymbol{\xi}(t) + \mathbf{w}(t), \tag{3.8}$$

where $\boldsymbol{\xi}$ is a physical magnitude, $\mathbf{F}$ is the time propagation (dynamic) matrix and $\mathbf{w}$ is a

time-correlated process such that:

$$\mathbf{w}(t) = \mathbf{E_w}\mathbf{a}(t) + \boldsymbol{\eta}(t). \tag{3.9}$$

The noise $\boldsymbol{\eta}$ is a White Gaussian Noise (WGN), $\mathbf{a}(t)$ is a correlated noise and $\mathbf{E_w}$ projects the correlated noise into the noise vector $\mathbf{w}$. The time dynamics of $\mathbf{a}$ are assumed to follow the structure:

$$\dot{\mathbf{a}}(t) = \mathbf{L}\mathbf{a}(t) + \mathbf{u}(t), \tag{3.10}$$

where $\mathbf{L}$ is the dynamic matrix and $\mathbf{u}$ is WGN. The state augmented model of the LDS in Equation (3.8) is in this case:

$$\begin{bmatrix} \dot{\boldsymbol{\xi}}(t) \\ \dot{\mathbf{a}}(t) \end{bmatrix} = \begin{bmatrix} \mathbf{F}(t) & \mathbf{E_w} \\ \mathbf{0} & \mathbf{L} \end{bmatrix} \begin{bmatrix} \boldsymbol{\xi}(t) \\ \mathbf{a}(t) \end{bmatrix} + \begin{bmatrix} \boldsymbol{\eta}(t) \\ \mathbf{u}(t) \end{bmatrix}. \tag{3.11}$$

3.5 First-Order Gauss-Markov Process

The error model structure from Equation (3.10) can be easily integrated in a state augmented LDS model as shown in Equation (3.11). Similarly, it can be easily considered in a Kalman filter estimator, making it quite suitable for practical applications. One error model that responds to the same structure and is widely used in practice to model many different physical error process is the first-order Gauss-Markov Process (GMP) [95].In fact, first-order GMP are proposed to model residual errors in MOPS [8] and in other GNSS literature [72], [96]. The are also widely used to model inertial sensors accelerometers and gyroscope biases [97]. Furthermore, a combination of first-order Gauss-Markov processes can be used to model more difficult error characteristics, such as bias instability in inertial sensors or rate random walk processes [98]. In this sense, this model can be considered to characterize more complex structures while still being able to include easily each of them as augmented states in a Kalman filter estimator. In Chapter 6, the total residual pseudorange and carrier-phase time-correlated error will be decomposed in several GMPs, each of them representing one of the error contributions. For the rest of the thesis when referring to GMP, it will always be a first-order GMP.

For snapshot GNSS estimator, overbounding pseudorange models are built based on Gaussian distribution because of its simplicity and special properties. The first-order Gauss-Markov model is therefore a natural choice when choosing conservative models bounding the empirical error processes as it can be considered an extension of the Gaussian model for time-correlated processes. It has a simple structure with only two parameters and it can be easily

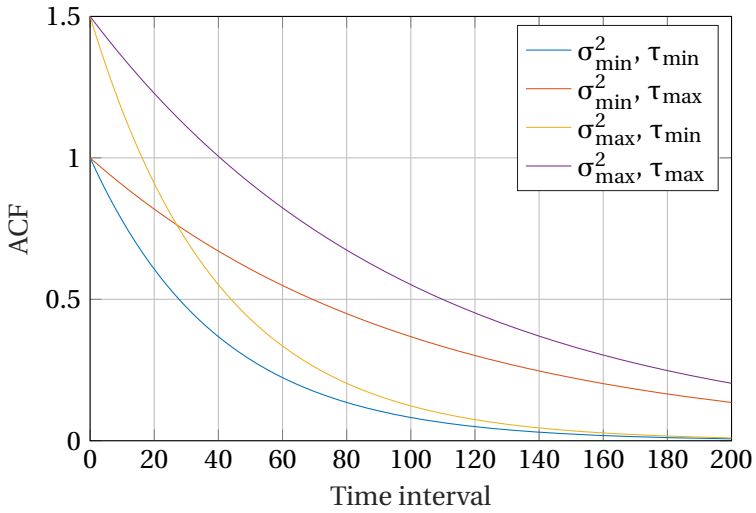

Figure 3.6: Autocovariance function (ACF) of different GMPs with $\sigma^2 \in \{1, 1.5\}$ and $\tau \in \{40, 100\}$

incorporated in linear estimators like Kalman filters.

A continuous-time stationary GMP model, also known as Ornstein-Uhlenbeck process [53], can be particularized from Equation (3.10) as:

$$\dot{a}(t) = \frac{1}{\tau} a(t) + u(t) \tag{3.12}$$

where $u(t)$ is a WGN with variance $\mathrm{Var}(u) = \frac{2\sigma^2}{\tau}$. The GMP model is therefore a parametric model with two parameters, a time-correlation constant τ and variance σ^2. By considering this model as a representation of the real process, the uncertain nature of a certain time-correlated process can be captured by considering both parameters uncertain. The main assumption in this thesis is that the GMP parameters are uncertain but bounded such that $\tau \in [\tau_{min}, \tau_{max}]$ and $\sigma^2 \in [\sigma^2_{min}, \sigma^2_{max}]$ due to unavoidable uncertainty in the error modeling process as discussed in Section 3.2.

Gauss-Markov processes are exponentially correlated with autocovariance function given by:

$$R_a(\mathrm{T}) = \sigma^2 e^{-\frac{\Delta_t}{\tau}}. \tag{3.13}$$

An autocovariance function example for the extreme parameters of an uncertain GMP with bounded parameters is depicted in Fig. 3.6. For example, as a result of empirically autocovariance functions from data as shown in Fig. 3.4. The autocorrelation function gives an intuitive representation of the degree of correlation of the process over time. However, it is difficult to interpret how the representation of an uncertain process in the autocorrelation domain can be linked with the error estimation in Kalman filtering of states affected by this process.

Table 3.1: Continuous-time and Discrete-time GMP models

	Continuous-time	Discrete-time
Model	$\dot{a}(t) = \frac{1}{\tau} a(t) + u(t)$	$a_k = e^{-\frac{\Delta_t}{\tau}} a_{k-1} + u_k$
Var(u)	$\frac{2\sigma^2}{\tau}$	$\sigma^2(1 - e^{-\frac{2\Delta_t}{\tau}})$

For instance, one may be misled by looking at Fig. 3.6 to think that a process with $\sigma^2 = \sigma^2_{\max}$ and $\tau = \tau_{\max}$ may provide an over bound in the error estimation of a Kalman filter estimation, which was already proven wrong in Section 1.2.

A stationary discrete-time first-order GMP model can be obtained, for instance, from Equation (3.12) by using standard continuous to discrete transformations [53]. In discrete-time, this GMP is also a first-order autoregressive model with Gaussian noise and exponential decay. Table 3.1 provides a summary of the continuous-time and discrete-time first-order stationary GMPs.

Part II
Bounding Kalman Filter with Uncertain Error Processes

4 Continuous-time Kalman Filter Bounding Models

This chapter studies the impact of uncertain parameters of Gauss-Markov processes in Kalman filtering and derives new stationary and non-stationary continuous-time GMP models that ensure tight bounding conditions for KF error covariance.

4.1 Bound Derivation via Advanced Sensitivity Analysis

4.1.1 KF Sensitivity Analysis

Consider a general linear dynamic system (LDS) described in the continuous-time domain:

$$\dot{\mathbf{x}}(t) = \mathbf{F}(t)\mathbf{x}(t) + \mathbf{G}(t)\mathbf{w}(t), \tag{4.1}$$

$$\mathbf{z}(t) = \mathbf{H}(t)\mathbf{x}(t) + \mathbf{J}(t)\mathbf{v}(t), \tag{4.2}$$

where $\mathbf{x} \in \mathbb{R}^s$ is the state vector, $\mathbf{F} \in \mathbb{R}^{s\times s}$ is the state dynamic matrix, $\mathbf{G} \in \mathbb{R}^{s\times p}$ is the process noise projection matrix, $\mathbf{z} \in \mathbb{R}^m$ is the observation or measurement vector, $\mathbf{J} \in \mathbb{R}^{m\times l}$ is the measurement noise projection matrix and $\mathbf{w} \in \mathbb{R}^p$ and $\mathbf{v} \in \mathbb{R}^l$ are the process and measurement noises with associated covariances matrix $\mathbf{Q}(t) = \mathrm{E}[\mathbf{w}(t)\mathbf{w}(t)^{\mathrm{T}}] \in \mathbb{R}^{p\times p}$ and $\mathbf{R}(t) = \mathrm{E}[\mathbf{v}(t)\mathbf{v}(t)^{\mathrm{T}}] \in \mathbb{R}^{l\times l}$ respectively. A Kalman filter (KF) estimator for Equation (4.1) and Equation (4.2) can be written as:

$$\dot{\hat{\mathbf{x}}} = \mathbf{F}\hat{\mathbf{x}} + \mathbf{K}\left(\mathbf{z} - \mathbf{H}\hat{\mathbf{x}}\right), \tag{4.3}$$

with an associated error covariance $\mathbf{P} \in \mathbb{R}^{s\times s}$ in the form of a Riccati equation:

$$\dot{\mathbf{P}} = \mathbf{F}\mathbf{P} + \mathbf{P}\mathbf{F}^{\mathrm{T}} - \mathbf{K}\mathbf{J}\mathbf{R}^{-1}\mathbf{J}^{\mathrm{T}}\mathbf{K}^{\mathrm{T}} + \mathbf{G}\mathbf{Q}\mathbf{G}^{\mathrm{T}}, \tag{4.4}$$

where the time arguments have been removed for clarity and $\mathbf{K} \in \mathbb{R}^{s\times m}$ is the Kalman gain. If the filter is designed with the true values of $\mathbf{F},\mathbf{H},\mathbf{G},\mathbf{J},\mathbf{Q},\mathbf{R}$, Equation (4.4) represents both the estimated covariance of the KF and the covariance of the error in $\hat{\mathbf{x}}$. In general, the matrix used to design the KF are imperfectly modeled $\hat{\mathbf{F}},\hat{\mathbf{H}},\hat{\mathbf{G}},\hat{\mathbf{J}},\hat{\mathbf{Q}},\hat{\mathbf{R}}$. The KF estimator will produce in this situation a covariance matrix $\hat{\mathbf{P}} \in \mathbb{R}^{s\times s}$ that is in general different from the true error covariance $\hat{\mathbf{P}} \neq \mathbf{P}$.

In [33] a methodology is presented to study the sensitivity of the imperfect design of $\hat{\mathbf{F}}$ and $\hat{\mathbf{H}}$ on the Kalman filter estimator. Define the estimation error vector $\mathbf{e} \triangleq \hat{\mathbf{x}} - \mathbf{x}$. Using Equation (4.3) with $\hat{\mathbf{F}}$ and $\hat{\mathbf{H}}$, Equation (4.1) and Equation (4.2), it can be shown that the error propagation satisfies the following differential equation:

$$\dot{\mathbf{e}} = \left(\hat{\mathbf{F}} - \hat{\mathbf{K}}\hat{\mathbf{H}}\right)\mathbf{e} + \left(\Delta\mathbf{F} - \hat{\mathbf{K}}\Delta\mathbf{H}\right)\mathbf{x} - \mathbf{G}\mathbf{w} + \hat{\mathbf{K}}\mathbf{J}\mathbf{v}, \tag{4.5}$$

where $\Delta\mathbf{F} \triangleq \hat{\mathbf{F}} - \mathbf{F}$, and $\Delta\mathbf{H} \triangleq \hat{\mathbf{H}} - \mathbf{H}$. The Kalman gain is computed from the Kalman filter processing as $\hat{\mathbf{K}} = \hat{\mathbf{P}}\hat{\mathbf{H}}^{\mathrm{T}}\mathbf{J}\hat{\mathbf{R}}^{-1}$ where $\hat{\mathbf{P}}$ satisfies the Riccati Equation (4.4) with the designed matrices:

$$\dot{\hat{\mathbf{P}}} = \hat{\mathbf{F}}\hat{\mathbf{P}} + \hat{\mathbf{P}}\hat{\mathbf{F}}^{\mathrm{T}} - \hat{\mathbf{P}}\hat{\mathbf{H}}^{\mathrm{T}}\mathbf{J}^{\mathrm{T}}\mathbf{R}^{-1}\mathbf{J}\hat{\mathbf{H}}\hat{\mathbf{P}} + \mathbf{G}\mathbf{Q}\mathbf{G}^{\mathrm{T}}. \tag{4.6}$$

Since $\dot{\mathbf{e}}$ also depends on the true state $\mathbf{x}$, Equation (4.5) can be translated to a matrix expression by considering the augmented vector $\boldsymbol{\zeta} = \begin{bmatrix} \mathbf{e}^{\mathrm{T}} & \mathbf{x}^{\mathrm{T}} \end{bmatrix}^{\mathrm{T}}$:

$$\begin{bmatrix} \dot{\mathbf{e}} \\ \dot{\mathbf{x}} \end{bmatrix} = \begin{bmatrix} \hat{\mathbf{F}} - \hat{\mathbf{K}}\hat{\mathbf{H}} & \Delta\mathbf{F} - \hat{\mathbf{K}}\Delta\mathbf{H} \\ \mathbf{0} & \mathbf{F} \end{bmatrix} \begin{bmatrix} \mathbf{e} \\ \mathbf{x} \end{bmatrix} + \begin{bmatrix} \hat{\mathbf{K}}\mathbf{J}\mathbf{v} \\ \mathbf{0} \end{bmatrix} + \begin{bmatrix} -\mathbf{G}\mathbf{w} \\ \mathbf{G}\mathbf{w} \end{bmatrix}. \tag{4.7}$$

The associated covariance matrix of Equation (4.7) is:

$$\begin{aligned} \dot{\mathbf{P}}_{\zeta} = &\begin{bmatrix} \hat{\mathbf{F}} - \hat{\mathbf{K}}\hat{\mathbf{H}} & \Delta\mathbf{F} - \hat{\mathbf{K}}\Delta\mathbf{H} \\ \mathbf{0} & \mathbf{F} \end{bmatrix} \mathbf{P}_{\zeta} + \mathbf{P}_{\zeta} \begin{bmatrix} \hat{\mathbf{F}} - \hat{\mathbf{K}}\hat{\mathbf{H}} & \Delta\mathbf{F} - \hat{\mathbf{K}}\Delta\mathbf{H} \\ \mathbf{0} & \mathbf{F} \end{bmatrix}^{\mathrm{T}} \\ &+ \begin{bmatrix} \hat{\mathbf{K}}\mathbf{J}\mathbf{R}\mathbf{J}^{\mathrm{T}}\hat{\mathbf{K}}^{\mathrm{T}} & \mathbf{0} \\ \mathbf{0} & \mathbf{0} \end{bmatrix} + \begin{bmatrix} \mathbf{G}\mathbf{Q}\mathbf{G}^{\mathrm{T}} & -\mathbf{G}\mathbf{Q}\mathbf{G}^{\mathrm{T}} \\ -\mathbf{G}\mathbf{Q}\mathbf{G}^{\mathrm{T}} & \mathbf{G}\mathbf{Q}\mathbf{G}^{\mathrm{T}} \end{bmatrix}. \end{aligned} \tag{4.8}$$

Since the covariance of the augmented vector $\boldsymbol{\zeta}$ can be expressed in four different blocks:

$$\mathbf{P}_{\zeta} = \begin{bmatrix} \mathbf{P}_{\mathrm{e}} & \mathbf{P}_{\mathrm{ex}} \\ \mathbf{P}_{\mathrm{ex}}^{\mathrm{T}} & \mathbf{P}_{\mathrm{x}} \end{bmatrix}, \tag{4.9}$$

Equation (4.8) provides a general expression to obtain the true error estimation covariance

$\mathbf{P} = \mathbf{P}_e$, when designing the KF with imperfect $\hat{\mathbf{F}}$ and $\hat{\mathbf{H}}$ (provided that we know the actual matrix). A similar analysis can be done for discrete-time KF as shown in Appendix A.1 or hybrid Kalman filter [99].

4.1.2 Conditions for Uncertain Gauss-Markov Processes

If the original noise processes considered in the linear dynamic system of Equation (4.1) and Equation (4.2) have time-correlated processes with Gauss-Markov structure, the common approach to decorrelate them consist of augmenting the KF state vector with the correlated processes as introduced in Section 3.4. The new augmented KF state vector can be therefore split into the *main* states of interest and the *augmented* states as:

$$\mathbf{x} = \begin{bmatrix} \boldsymbol{\xi} \\ \mathbf{a} \end{bmatrix}, \tag{4.10}$$

where the different GMP in $\mathbf{a} \in \mathbb{R}^{n\times 1}$ can be expressed as:

$$\dot{a}_i(t) = -\frac{1}{\tau_i} a_i(t) + \sqrt{\frac{2\sigma_i^2}{\tau_i}} \eta_i(t), \text{ with } \eta_i(t) \sim \mathcal{N}(0,1),\ \forall i \in [1,2,...,n], \tag{4.11}$$

where $\tau \in \mathbb{R} > 0$ is the GMP correlation time constant and $\sigma_i^2 \in \mathbb{R} \geq 0$ is the stationary process variance. The augmented state dynamics system is now [100]:

$$\begin{bmatrix} \dot{\boldsymbol{\xi}} \\ \dot{\mathbf{a}} \end{bmatrix} = \begin{bmatrix} \mathbf{F} & \mathbf{F}_{\xi\mathbf{a}} \\ \mathbf{0} & \mathbf{F}_a \end{bmatrix} \begin{bmatrix} \boldsymbol{\xi} \\ \mathbf{a} \end{bmatrix} + \begin{bmatrix} \mathbf{G} & \mathbf{0} \\ \mathbf{0} & \mathbf{I} \end{bmatrix} \begin{bmatrix} \mathbf{w} \\ \sqrt{\mathbf{q}}\boldsymbol{\eta} \end{bmatrix}, \tag{4.12}$$

where

$$\mathbf{F}_a = \begin{bmatrix} -\frac{1}{\tau_1} & \mathbf{0} & \cdots & \mathbf{0} \\ \mathbf{0} & -\frac{1}{\tau_2} & \cdots & \mathbf{0} \\ \vdots & \vdots & \ddots & \vdots \\ \mathbf{0} & \cdots & \cdots & -\frac{1}{\tau_n} \end{bmatrix}, \text{ and } \mathbf{q} = \begin{bmatrix} \frac{2\sigma_1^2}{\tau_1} \\ \frac{2\sigma_2^2}{\tau_2} \\ \vdots \\ \frac{2\sigma_n^2}{\tau_n} \end{bmatrix}. \tag{4.13}$$

The design of the KF is done with a $\hat{\mathbf{F}}_a$ (i.e. $\hat{\tau}_i, \forall i \in [1,n]$) that in general would not match the true one due to the limitations that are described in Chapter 3. The error due to the imperfect design of $\mathbf{F}_a$ can be obtained from Equation (4.8), where in this case some simplifications can be done: First, the imperfect design of the augmented states does not affect the measurement matrix nor the measurement noise and therefore $\Delta\mathbf{H} = \mathbf{0}$ and $\hat{\mathbf{R}} = \mathbf{R}$. Second, since the imperfect design only affects the augmented states, it is only needed to consider with the extended

vector for sensitivity analysis these states within the vector $\boldsymbol{\zeta}$, such that now $\boldsymbol{\zeta} = \left[\mathbf{e}^{\mathrm{T}}\ \mathbf{a}^{\mathrm{T}}\right]^{\mathrm{T}}$, in for instance Equation (4.7). Equation (4.8) can be then rewritten to:

$$\dot{\mathbf{P}}_{\zeta} = \begin{bmatrix} \hat{\mathbf{F}} - \hat{\mathbf{K}}\mathbf{H} & \Delta\mathbf{F} \\ \mathbf{0} & \mathbf{F}_{\mathrm{a}} \end{bmatrix} \mathbf{P}_{\zeta} + \mathbf{P}_{\zeta} \begin{bmatrix} \hat{\mathbf{F}} - \hat{\mathbf{K}}\mathbf{H} & \Delta\mathbf{F} \\ \mathbf{0} & \mathbf{F}_{\mathrm{a}} \end{bmatrix}^{\mathrm{T}} + \begin{bmatrix} \hat{\mathbf{K}}\mathbf{J}\mathbf{R}\mathbf{J}^{\mathrm{T}}\hat{\mathbf{K}}^{\mathrm{T}} & \mathbf{0} \\ \mathbf{0} & \mathbf{0} \end{bmatrix} + \begin{bmatrix} \mathbf{G}\mathbf{Q}_{\xi}\mathbf{G}^{\mathrm{T}} & \mathbf{0} & \mathbf{0} \\ \mathbf{0} & \mathbf{Q}_{\mathrm{a}} & -\mathbf{Q}_{\mathrm{a}} \\ \mathbf{0} & -\mathbf{Q}_{\mathrm{a}} & \mathbf{Q}_{\mathrm{a}} \end{bmatrix}, \tag{4.14}$$

where

$$\Delta\mathbf{F} = \begin{bmatrix} \mathbf{0} \\ \Delta\mathbf{F}_{\mathrm{a}} \end{bmatrix},\ \Delta\mathbf{F}_{\mathrm{a}} \triangleq \hat{\mathbf{F}}_{\mathrm{a}} - \mathbf{F}_{\mathrm{a}},\ \text{and}\ \mathbf{Q}_{\mathrm{a}} = \mathrm{E}[\mathbf{q}\mathbf{q}^{\mathrm{T}}]. \tag{4.15}$$

Equation (4.14) provides the true error covariance matrix under the wrongly designed KF matrices (i.e., $\mathbf{F}$ and $\mathbf{Q}$). The main goal is to design the filter in such a way so that the KF estimated covariance is greater than the true error covariance, that is $\hat{\mathbf{P}} \geq \mathbf{P}$. However, it is not clear how to use Equation (4.14) to derive suitable conditions, since it depends on the true noise errors and matrices which are unknown. For this purpose the use of an auxiliary Riccati equation is introduced:

$$\dot{\boldsymbol{\Sigma}} = \begin{bmatrix} \hat{\mathbf{F}} - \hat{\mathbf{K}}\mathbf{H} & \mathbf{0} \\ \mathbf{0} & \mathbf{F}_{\mathrm{a}} \end{bmatrix} \boldsymbol{\Sigma} + \boldsymbol{\Sigma} \begin{bmatrix} \hat{\mathbf{F}} - \hat{\mathbf{K}}\mathbf{H} & \mathbf{0} \\ \mathbf{0} & \mathbf{F}_{\mathrm{a}} \end{bmatrix}^{\mathrm{T}} + \begin{bmatrix} \hat{\mathbf{K}}\mathbf{J}\mathbf{R}\mathbf{J}^{\mathrm{T}}\hat{\mathbf{K}}^{\mathrm{T}} & \mathbf{0} \\ \mathbf{0} & \mathbf{0} \end{bmatrix} + \begin{bmatrix} \mathbf{G}\hat{\mathbf{Q}}_{\mathrm{x}}\mathbf{G}^{\mathrm{T}} & \mathbf{0} \\ \mathbf{0} & \bar{\mathbf{Q}}_{\mathrm{a}} \end{bmatrix}. \tag{4.16}$$

where an auxiliary process with covariance $\bar{\mathbf{Q}}_{\mathrm{a}}$ is introduced and will be designed later. The matrix $\boldsymbol{\Sigma}$ is a block diagonal matrix:

$$\boldsymbol{\Sigma} = \begin{bmatrix} \boldsymbol{\Sigma}_{\mathrm{x}} & \mathbf{0} \\ \mathbf{0} & \boldsymbol{\Sigma}_{\mathrm{a}} \end{bmatrix} \tag{4.17}$$

In Equation (4.16) the reader can find a Riccati expression of a designed KF, similarly to Equation (4.6) that is therefore propagated independently from the introduced auxiliary process $\boldsymbol{\Sigma}_{\mathrm{a}}$. The auxiliary process $\boldsymbol{\Sigma}_{\mathrm{a}}$ is chosen to share the propagation matrix $\mathbf{F}_{\mathrm{a}}$ of the true process and a process covariance matrix $\bar{\mathbf{Q}}_{\mathrm{a}}$ that only needs to satisfy $\bar{\mathbf{Q}}_{\mathrm{a}} \geq \mathbf{Q}_{\mathrm{a}}$ as it will be shown later. The covariance of the designed KF will bound the true error covariance if and

only if $\boldsymbol{\Sigma} - \mathbf{P}_\zeta \geq 0$, which is equivalent to guaranteeing that the two inequalities:

$$\dot{\boldsymbol{\Sigma}} - \dot{\mathbf{P}}_\zeta \geq 0, \text{ and } \boldsymbol{\Sigma}(0) - \mathbf{P}_\zeta(0) \geq 0. \tag{4.18}$$

In order to find suitable values for $\hat{\mathbf{F}}$ and $\hat{\mathbf{Q}}_\mathrm{x}$ that guarantee bounding conditions, Equation (4.16) must be therefore compared with Equation (4.14). However, these do not share completely the same elements of the propagation matrices yet. Equation (4.16) is then rewritten to include the terms $\Delta\mathbf{F}$ by summing and substracting them as:

$$\begin{aligned}\dot{\boldsymbol{\Sigma}} = &\begin{bmatrix} \hat{\mathbf{F}} - \hat{\mathbf{K}}\mathbf{H} & \Delta\mathbf{F} \\ \mathbf{0} & \mathbf{F}_\mathrm{a} \end{bmatrix} \boldsymbol{\Sigma} + \boldsymbol{\Sigma} \begin{bmatrix} \hat{\mathbf{F}} - \hat{\mathbf{K}}\mathbf{H} & \Delta\mathbf{F} \\ \mathbf{0} & \mathbf{F}_\mathrm{a} \end{bmatrix}^\mathrm{T} + \begin{bmatrix} \hat{\mathbf{K}}\mathbf{J}\mathbf{R}\mathbf{J}^\mathrm{T}\hat{\mathbf{K}}^\mathrm{T} & \mathbf{0} \\ \mathbf{0} & \mathbf{0} \end{bmatrix} \\ &+ \begin{bmatrix} \mathbf{G}\hat{\mathbf{Q}}_\mathrm{x}\mathbf{G}^\mathrm{T} & -\Delta\mathbf{F}\boldsymbol{\Sigma}_\mathrm{a} \\ -\Delta\mathbf{F}\boldsymbol{\Sigma}_\mathrm{a} & \bar{\mathbf{Q}}_\mathrm{a} \end{bmatrix}.\end{aligned} \tag{4.19}$$

The difference between true error covariance in Equation (4.14) and designed KF error covariance can be now evaluated using the transformation $\Delta = \boldsymbol{\Sigma} - \mathbf{P}_\zeta$:

$$\begin{aligned}\dot{\boldsymbol{\Delta}} = &\begin{bmatrix} \hat{\mathbf{F}} - \hat{\mathbf{K}}\mathbf{H} & \Delta\mathbf{F} \\ \mathbf{0} & \mathbf{F}_\mathrm{a} \end{bmatrix} \boldsymbol{\Delta} + \boldsymbol{\Delta} \begin{bmatrix} \hat{\mathbf{F}} - \hat{\mathbf{K}}\mathbf{H} & \Delta\mathbf{F} \\ \mathbf{0} & \mathbf{F}_\mathrm{a} \end{bmatrix}^\mathrm{T} \\ &+ \begin{bmatrix} \hat{\mathbf{Q}}_\xi - \mathbf{Q}_\xi & \mathbf{0} & \mathbf{0} \\ \mathbf{0} & \hat{\mathbf{Q}}_\mathrm{a} - \mathbf{Q}_\mathrm{a} & -\Delta\mathbf{F}_\mathrm{a}\boldsymbol{\Sigma}_\mathrm{a} + \mathbf{Q}_\mathrm{a} \\ \mathbf{0} & -\boldsymbol{\Sigma}_\mathrm{a}\Delta\mathbf{F}_\mathrm{a}^\mathrm{T} + \mathbf{Q}_\mathrm{a} & \bar{\mathbf{Q}}_\mathrm{a} - \mathbf{Q}_\mathrm{a} \end{bmatrix}.\end{aligned} \tag{4.20}$$

The conditions in Equation (4.18) are satisfied if $\Delta(0) \geq \mathbf{0}$ and the last matrix term in Equation (4.20) is positive semidefinite. The process noise of the unaugmented states can be assumed to be properly designed so that $\hat{\mathbf{Q}}_\xi - \mathbf{Q}_\xi \geq 0$. Therefore, ensuring semidefiniteness in Equation (4.20) reduces to the lower right 2x2 block elements to satisfy:

$$\begin{bmatrix} \hat{\mathbf{Q}}_\mathrm{a} - \mathbf{Q}_\mathrm{a} & -\Delta\mathbf{F}_\mathrm{a}\boldsymbol{\Sigma}_\mathrm{a} + \mathbf{Q}_\mathrm{a} \\ -\boldsymbol{\Sigma}_\mathrm{a}\Delta\mathbf{F}_\mathrm{a}^\mathrm{T} + \mathbf{Q}_\mathrm{a} & \bar{\mathbf{Q}}_\mathrm{a} - \mathbf{Q}_\mathrm{a} \end{bmatrix} \geq 0. \tag{4.21}$$

The condition in Equation (4.21) will be exploited to derive GMP model parameters that guarantee KF covariance bounding condition in the next section. On the other side, the

second condition in Equation (4.18) is:

$$\begin{bmatrix} \boldsymbol{\Sigma}_{\xi}(0) & \mathbf{0} & \mathbf{0} \\ \mathbf{0} & \hat{\boldsymbol{\Sigma}}_{\mathrm{a}}(0) & \mathbf{0} \\ \mathbf{0} & \mathbf{0} & \bar{\boldsymbol{\Sigma}}_{\mathrm{a}}(0) \end{bmatrix} - \begin{bmatrix} \mathbf{P}(0) & \mathbf{0} & \mathbf{0} \\ \mathbf{0} & \mathbf{P}_{\mathrm{a}}(0) & -\mathbf{P}_{\mathrm{a}}(0) \\ \mathbf{0} & -\mathbf{P}_{\mathrm{a}}(0) & \mathbf{P}_{\mathrm{a}}(0) \end{bmatrix} \geq \mathbf{0}, \tag{4.22}$$

Since we recall that the auxiliary matrix $\boldsymbol{\Sigma}$ is block diagonal. For stationary processes, this condition is satisfied if Equation (4.21) is satisfied [73]. Equation (4.22) will be used later to derive conditions for non-stationary models.

4.1.3 Conservative Stationary Bound

In general, one is free to design the process $\boldsymbol{\Sigma}_{\mathrm{a}}$ as far as the condition in Equation (4.21) is satisfied. A way to derive simplified conditions for $\hat{\mathbf{Q}}_{\mathrm{a}}$ and $\hat{\mathbf{F}}_{\mathrm{a}}$ is to impose:

$$-\Delta\mathbf{F}_{\mathrm{a}}\boldsymbol{\Sigma}_{\mathrm{a}} + \mathbf{Q}_{\mathrm{a}} = \mathbf{0}. \tag{4.23}$$

In this case, the matrix in Equation (4.21) is a diagonal matrix leading to the simplified conditions $\hat{\mathbf{Q}}_{\mathrm{a}} \geq \mathbf{Q}_{\mathrm{a}}$ and $\bar{\mathbf{Q}}_{\mathrm{a}} \geq \mathbf{Q}_{\mathrm{a}}$. Since all the matrices in Equation (4.21) are diagonal matrices representing the individual correlated processes that are assumed to be independent among each other, it is sufficient to work with one arbitrary process in a scalar fashion. Under that, using Equation (4.13) and Equation (4.15), Equation (4.23) simplifies for a single diagonal element to:

$$\left(\frac{1}{\tau} - \frac{1}{\hat{\tau}}\right)\sigma_{\mathrm{a}}^2 - \frac{2\sigma^2}{\tau} = 0 \longrightarrow \sigma_{\mathrm{a}}^2 = 2\sigma^2\left(1 - \frac{\tau}{\hat{\tau}}\right)^{-1}. \tag{4.24}$$

For a single GMP process, $\bar{\mathbf{Q}}_{\mathrm{a}}$ is:

$$\bar{q}_{\mathrm{a}} = \frac{2\sigma_{\mathrm{a}}^2}{\tau} = \frac{4\sigma^2}{\tau}\left(\frac{\hat{\tau}}{\hat{\tau} - \tau}\right). \tag{4.25}$$

Since $\bar{q}_a$ is a variance element and therefore non-negative and it must be greater than q_a, the only way to satisfy it is by making Equation (4.25) non-negative. This can only happen if $\hat{\tau} \geq \tau$ and therefore it must be chosen from the possible range of τ to be $\hat{\tau} = \tau_{\max}$.

The other condition that must be satisfied is $\hat{\mathbf{Q}}_{\mathrm{a}} \geq \mathbf{Q}_{\mathrm{a}}$, which for a specific noise component translates to:

$$\hat{q}_{\mathrm{a}} \geq q_{\mathrm{a}}, \tag{4.26}$$

$$\frac{2\hat{\sigma}^2}{\hat{\tau}} \geq \frac{2\sigma^2}{\tau} \longrightarrow \hat{\sigma}^2 \geq \frac{\sigma^2\hat{\tau}}{\tau}. \tag{4.27}$$

Since $\hat{\tau}$ has been already selected to be τ_{max}, it is obvious that the inequality is more restrictive when $\sigma^2 = \sigma^2_{max}$ and when $\tau = \tau_{min}$, giving finally the condition for $\hat{\sigma}^2$:

$$\hat{\sigma}^2 \geq \sigma^2_{max} \frac{\tau_{max}}{\tau_{min}}, \tag{4.28}$$

which would be typically chosen at the equality point to avoid extra conservatism. It can be shown that the GMP with $\tau = \tau_{max}$ and $\hat{\sigma}^2$ in Equation (4.28) produces the same bound as in [84]. However, the formulation presented here preserves the structure of a GMP and offers clear interpretation.

Theorem 4.1.1 (Gauss-Markov Conservative Model)**.**

The estimation of error covariance by a Kalman filter estimator with uncertain time-correlated Gauss-Markov parameters in the range $\sigma^2 \in [\sigma^2_{min}, \sigma^2_{max}]$ and $\tau \in [\tau_{min}, \tau_{max}]$ can be bounded if the filter is designed with augmented stationary Gauss-Markov states and following parameters:

$$\hat{\tau} = \tau_{max} \quad \text{and} \quad \hat{\sigma}^2 = \sigma^2_{max} \frac{\tau_{max}}{\tau_{min}}. \tag{4.29}$$

4.2 Derivation via Spectral Density Bounding

Frequency domain analysis has been widely used to model signals and error processes [55] and they are considered when designing Kalman filter covariance matrices [28]. More recently, Power Spectral Densities (PSD) can be also considered when designing safety related estimators when considering Theorem 4.2.1.

Theorem 4.2.1 (Frequency Domain Bounding in Continuous-time)**.**

The covariance matrix of the error of a Kalman filter estimation $\mathbf{P}$ can be upper bounded with the estimated KF covariance $\hat{\mathbf{P}}$, i.e., $\hat{\mathbf{P}} \geq \mathbf{P}$, when designing each of the measurement and process noises i with Power Spectral Densities (PSD) $\hat{S}_i(\omega)$ such that they bound the actual error PSD $S_i(\omega)$, i.e., $\hat{S}_i(\omega) \geq S_i(\omega), \forall \omega \in [0, \infty]$.

Proof of Theorem 4.2.1 can be found in Appendix B.1, which is here adapted from [51].

Frequency domain analysis with Power Spectral Density (PSD) is in the following then used to find new conditions for uncertain GMP in order to bound linear dynamic system estimators.

4.2.1 Stationary Continuous-Time GMP Model

Problem Formulation

In order to derive GMP model conditions for the KF process and measurement noise, bounding conditions on the PSDs of the uncertain GMPs are investigated. The spectral density of a GMP in the continuous-time domain S_c can be expressed as [53]:

$$S_c(\omega) = \frac{2\sigma^2/\tau}{\omega^2 + (1/\tau)^2}, \tag{4.30}$$

where $\omega = 2\pi f$ is the angular frequency in radians per seconds, with f being the linear frequency in Herz and the subscript c is used to refer to the continuous-time domain. Exemplary, Figure (4.1) shows different PSD curves for GMPs with time constants ranging from 10 to 100 seconds. In Figure (4.1), the lines corresponding to GMPs with different time constants cross with the others at different frequencies. As explained in Section 5.3, this illustrates the fact that a KF designed by taking the maximum value of GMP time correlation constant does not necessarily bound the actual true covariance at any time (or at any frequency).

Since the spectrum of a real process is an even function, it is only needed to bound the PSD over $[0,\infty)$ following Theorem 4.2.1:

$$\hat{S}_c(\omega) \geq S_c(\omega), \forall \omega \in [0,\infty), \tag{4.31}$$

where $\hat{S}_c$ is the bounding PSD of the continuous-time GMP model to be determined. Furthermore, in order to find the tightest possible bound, the total net power of each of the process models must be minimized. This can be expressed therefore as the following minimization problem:

$$\begin{aligned} &\min_{\hat{\sigma}_c,\hat{\tau}_c} \frac{1}{\pi}\int_0^\infty \hat{S}_c(\omega)d\omega = \min_{\hat{\sigma}_c,\hat{\tau}_c} \hat{\sigma}_c^2, \\ &\text{such that } \hat{S}_c(\omega) \geq S_c(\omega), \\ &\forall\, \omega \in [0,\infty), \forall\, \tau \in [\tau_{min},\tau_{max}] \text{ and } \forall \sigma^2 \in [\sigma^2_{min},\sigma^2_{max}]. \end{aligned} \tag{4.32}$$

where $\hat{\sigma}_c$ and $\hat{\tau}_c$ are, respectively, the variance and time-correlation constant parameters of the continuous-time GMP model that guarantees bounding conditions.

Continuous-Time Model Derivation

The derivation of a GMP model solution starts by using Equation (4.30) to express Equation (4.31) as:

$$\frac{2\hat{\sigma}_c^2/\hat{\tau}_c}{\omega^2+1/\hat{\tau}_c^2} \geq \frac{2\sigma^2/\tau}{\omega^2+1/\tau^2},\ \forall\omega\in[0,\infty). \tag{4.33}$$

Subtracting the right-hand-side term from both sides of the inequality, writing the resulting fraction with a common denominator, and factoring out ω^2 in the terms where it appears in the numerator, Equation (4.33) becomes:

$$\frac{\omega^2(2\hat{\sigma}_c^2\tau-2\sigma^2\hat{\tau}_c)+\frac{2\hat{\sigma}_c^2\hat{\tau}_c-2\sigma^2\tau}{\tau\hat{\tau}_c}}{\tau\hat{\tau}_c(\omega^2+1/\hat{\tau}_c^2)(\omega^2+1/\tau^2)} \geq 0,\forall\omega\in[0,\infty). \tag{4.34}$$

Since ω, τ and $\hat{\tau}_c$ are positive, the denominator in Equation (4.34) is always positive. Therefore, the numerator must also be non-negative:

$$\omega^2(\hat{\sigma}_c^2\tau-\sigma^2\hat{\tau}_c)+\frac{\hat{\sigma}_c^2\hat{\tau}_c-\sigma^2\tau}{\tau\hat{\tau}_c} \geq 0,\forall\omega\in[0,\infty). \tag{4.35}$$

Equation (4.35) is linear in ω^2, i.e., monotonically increasing or decreasing with $\omega \geq 0$. Thus, a necessary and sufficient condition for Equation (4.35) to be satisfied $\forall\,\omega\in[0,\infty)$ is that it must hold true for the two limit values of ω. At the limit when $\omega\to\infty$ and $\omega = 0$, the following two conditions are derived:

$$\hat{\sigma}_c^2\tau-\sigma^2\hat{\tau}_c \geq 0, \tag{4.36}$$

$$\hat{\sigma}_c^2\hat{\tau}_c-\sigma^2\tau \geq 0, \tag{4.37}$$

which can be rewritten as:

$$\hat{\sigma}_c^2 \geq \frac{\sigma^2\tau}{\hat{\tau}_c},\quad \hat{\sigma}_c^2 \geq \frac{\sigma^2\hat{\tau}_c}{\tau}. \tag{4.38}$$

These expressions must be satisfied $\forall\,\tau\in[\tau_{min},\tau_{max}]$ and $\forall\sigma^2\in[\sigma^2_{min},\sigma^2_{max}]$. Both conditions are clearly more restrictive when $\sigma^2=\sigma^2_{max}$. The first one is also more restrictive when $\tau=\tau_{max}$, whereas the second one is more restrictive when $\tau=\tau_{min}$. Thus, when considering the entire range of possible GMP model parameter values, Equation (4.38) becomes:

$$\hat{\sigma}_c^2 \geq \frac{\sigma^2_{max}\tau_{max}}{\hat{\tau}_c},\quad \hat{\sigma}_c^2 \geq \frac{\sigma^2_{max}\hat{\tau}_c}{\tau_{min}}. \tag{4.39}$$

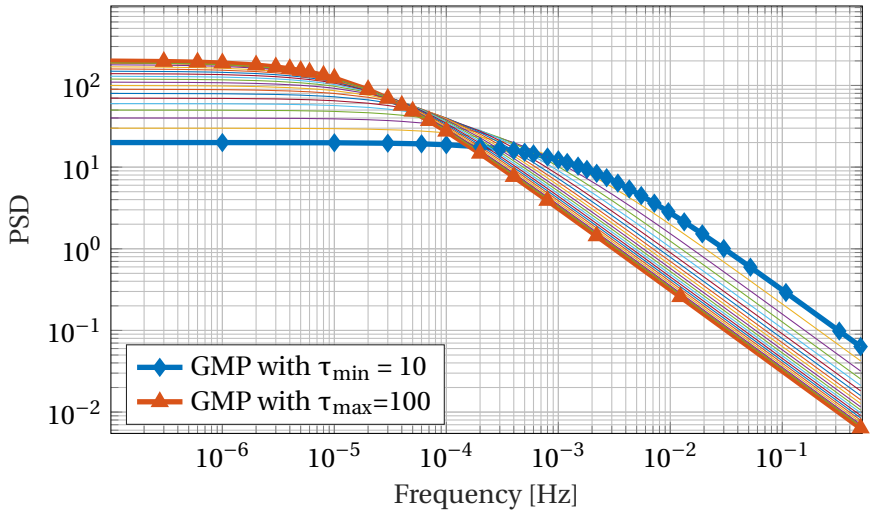

Figure 4.1: Power Spectral Density (PSD) of GM processes with with $\sigma^2 = 1$ and different values of $\tau \in [10, 100]s$.

The tightest GMP bound is the one that minimizes $\hat{\sigma}_c^2$ according to Equation (4.32). In Equation (4.39), this is achieved at equality, i.e., for the following equations:

$$\hat{\sigma}_c^2 = \frac{\sigma_{max}^2 \tau_{max}}{\hat{\tau}_c}, \quad \hat{\sigma}_c^2 = \frac{\sigma_{max}^2 \hat{\tau}_c}{\tau_{min}}. \tag{4.40}$$

Solving Equation (4.40) for $\hat{\sigma}_c^2$ and $\hat{\tau}_c$ gives the solution in Equation (4.41).

Theorem 4.2.2 (Continuous-time Gauss-Markov Tight Model)**.**

The stationary continuous-time GMP model that provides the tightest bound on an actual GMP with uncertain but bounded variance $\sigma^2 \in [\sigma_{min}^2, \sigma_{max}^2]$ and time constant $\tau \in [\tau_{min}, \tau_{max}]$ is determined by the following time correlation constant and variance:

$$\hat{\tau}_c = \sqrt{\tau_{min}\tau_{max}}, \qquad \hat{\sigma}_c^2 = \sigma_{max}^2 \sqrt{\frac{\tau_{max}}{\tau_{min}}}. \tag{4.41}$$

The solution in Equation (4.41) provides not only a tight bound at the PSD domain, but it also ensures the choice of parameters for uncertain augmented states noises as a bounding condition for Kalman filter or other LDS estimator in continuous-time domain.

Stationary Bounds Evaluation

Figure (4.2) presents the tight stationary GMP bound derived in the continuous-time domain, the stationary conservative bound derived in Section 4.1.3 and possible realizations of the actual GMP with unit variance and time constants varying from 10 to 100 seconds (differently

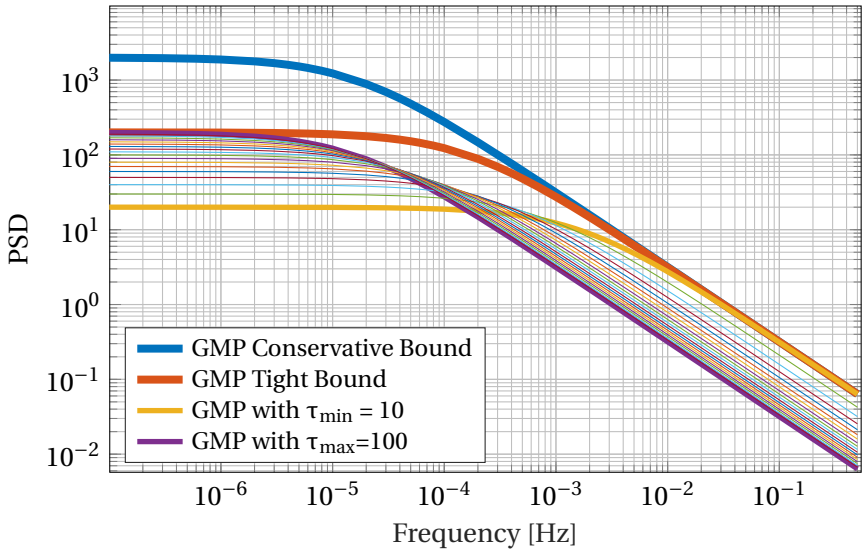

Figure 4.2: Power Spectral Density (PSD) of GMP with $\sigma^2 = 1$ and different values of $\tau \in [10, 100]s$; Conservative bound in Theorem 4.1.1 and tight bound in Theorem 4.2.2.

color-coded). Figure (4.2) illustrates the fact that the bound in Section 4.1.3 is looser at low frequencies than the one obtained via spectral bounding, and that this bound is the tightest possible stationary bound with a GMP structure.

4.3 Non-Stationary Bounds

Previous sections derived stationary models to bound uncertain GMP in continuous-time domain. As a consequence of accounting for the range of possible time correlation constant values within the GMP parameter uncertainty, one interpretation indicates that the variance of the bounding process model need to consider the maximum possible variance inflated by factor depending on the ratio between the maximum and minimum time correlation constant as seen in Equation (4.29) and Equation (4.41). This can become unnecessary conservative at the start of operation when the process has not experience any time propagation yet. A way to make the GMP model tighter is by considering a non-stationary GMP model that presents a transient phase at the beginning of its inclusion in the linear dynamic estimator. The new model will match the stationary one at steady state, but will provide a tighter estimation error variance bound during the transient period.

4.3.1 Derivation using Sensitivity Analysis

Section 4.1 detailed a methodology to derive conditions on the GMP model uncertainty as such these are reflected in the KF error covariance. One of the conditions in Equation (4.22)

was that the initial covariance of the auxiliary matrix $\boldsymbol{\Sigma}(0)$ had to be greater or equal to the initial true error covariance $\mathbf{P}_\zeta(0)$. Equation (4.22) can be rewriting recalling Equation (4.10) in the following way:

$$\begin{bmatrix} \boldsymbol{\Sigma}_\xi(0) - \mathbf{P}_\xi(0) & \mathbf{0} & \mathbf{0} \\ \mathbf{0} & \hat{\boldsymbol{\Sigma}}_a(0) - \mathbf{P}_a(0) & \mathbf{P}_a(0) \\ \mathbf{0} & \mathbf{P}_a(0) & \bar{\boldsymbol{\Sigma}}_a(0) - \mathbf{P}_a(0) \end{bmatrix} \geq \mathbf{0}, \tag{4.42}$$

The true GMP processes are assumed to be stationary and therefore $\mathbf{P}_a(0) = \mathbf{P}_a$. This was also considered for the auxiliary process introduced in Equation (4.16) which simplifies $\bar{\boldsymbol{\Sigma}}_a(0) = \bar{\boldsymbol{\Sigma}}_a$. The initialization of the states of interest is assumed to be done in such a way that $\boldsymbol{\Sigma}_\xi(0) \geq \mathbf{P}(0)$. Therefore it is only necessary to further consider the condition:

$$\begin{bmatrix} \hat{\boldsymbol{\Sigma}}_a(0) - \mathbf{P}_a & \mathbf{P}_a \\ \mathbf{P}_a & \bar{\boldsymbol{\Sigma}}_a - \mathbf{P}_a \end{bmatrix} \geq \mathbf{0}. \tag{4.43}$$

Notice that all the matrices in Equation (4.43) are diagonal since they contain parameters of the different independent time-correlated GMP processes. Therefore, the condition in Equation (4.43) can be ensured by ensuring it is true for each of the process parameters. Consider the 2x2 submatrix of an arbitrary process:

$$\begin{bmatrix} \hat{\sigma}^2_{c,0} - \sigma^2 & -\sigma^2 \\ -\sigma^2 & \bar{\sigma}^2 - \sigma^2 \end{bmatrix} \geq \mathbf{0}, \tag{4.44}$$

which leads finally to the following important condition on $\hat{\sigma}^2_{c,0}$ [99]:

$$\hat{\sigma}^2_{c,0} \geq \sigma^2 + \frac{\sigma^4}{\bar{\sigma}^2 - \sigma^2}. \tag{4.45}$$

Initial Variance for conservative bound

For the situation of the conservative bound shown in Section 4.1.3, and using Equation (4.25), the value of $\bar{\sigma}^2$ can be shown to be [73]:

$$\bar{\sigma}^2 = 2\sigma^2 \left(\frac{\tau_{max}}{\tau_{max} - \tau} \right). \tag{4.46}$$

Equation (4.45) is then equal to:

$$\hat{\sigma}^2_{c,0} \geq \sigma^2 \frac{2}{1 + \frac{\tau}{\tau_{max}}}, \tag{4.47}$$

which is more restrictive when $\tau = \tau_{min}$ and $\sigma^2 = \sigma^2_{max}$. Finally and in order to avoid extra conservatism, $\hat{\sigma}^2_{c,0}$ can be chosen at the equality to build the conservative non-stationary model with:

$$\hat{\sigma}^2_{c,0} = \sigma^2_{max} \frac{2}{1 + \frac{\tau_{min}}{\tau_{max}}}. \tag{4.48}$$

Theorem 4.3.1 (Non-stationary Gauss-Markov Conservative Model)**.**

The estimation of error covariance by a Kalman filter estimator with uncertain time-correlated Gauss-Markov parameters in the range $\sigma^2 \in [\sigma^2_{min}, \sigma^2_{max}]$ and $\tau \in [\tau_{min}, \tau_{max}]$ can be bounded if the filter is designed with augmented states modeled with a non-stationary GMP model with parameters:

$$\hat{\tau} = \tau_{max} \quad \text{and} \quad \hat{\sigma}^2 = \sigma^2_{max} \frac{\tau_{max}}{\tau_{min}}. \tag{4.49}$$

and initial variance given by:

$$\hat{\sigma}^2_{c,0} = \sigma^2_{max} \frac{2}{1 + \frac{\tau_{min}}{\tau_{max}}}. \tag{4.50}$$

Tight Initial Variance derivation

In the next, instead of using the conservative stationary bound of Section 4.1.3, let us consider the tight stationary bound obtained via frequency domain analysis of Section 4.2.1 in order to find the initial variance of a new tight non-stationary GMP. The initial condition can be obtained from Equation (4.45) when the value of $\bar{\sigma}^2$ related to the use of the tight bound parameters in Equation (4.41). In order to find the expression for $\bar{\sigma}^2$, it is necessary to revisit the general condition on the advanced sensitivity approach in Equation (4.21), that is here rewritten for convenience:

$$\begin{bmatrix} \hat{\mathbf{Q}}_a - \mathbf{Q}_a & -\Delta\mathbf{F}_a\boldsymbol{\Sigma}_a + \mathbf{Q}_a \\ -\boldsymbol{\Sigma}_a\Delta\mathbf{F}_a^T + \mathbf{Q}_a & \bar{\mathbf{Q}}_a - \mathbf{Q}_a \end{bmatrix} \geq \mathbf{0}. \tag{4.51}$$

Since the noise elements are uncorrelated and therefore the matrices are diagonal matrices, the condition for each noise component can be written as:

$$\begin{bmatrix} \hat{q} - q & -\delta l\bar{\sigma}^2 + q \\ -\delta l\bar{\sigma}^2 + q & \bar{q} - q \end{bmatrix} \geq \mathbf{0}, \tag{4.52}$$

Using Schur complements to force the cross-term to be zero, Equation (4.52) becomes:

$$\begin{bmatrix} \hat{q}-q-(q-\delta l\bar{\sigma}^2)^2(\bar{q}-q)^{-1} & 0 \\ 0 & \bar{q}-q \end{bmatrix} \geq \mathbf{0}. \tag{4.53}$$

Since Equation (4.53) is diagonal, it will be positive semidefinite if the diagonal elements are non-negative. The first diagonal element can be expressed as:

$$\hat{q}-q-\left(q+\frac{\tau}{2}\left(\frac{1}{\hat{\tau}}-\frac{1}{\tau}\right)\bar{q}\right)^2(\bar{q}-q)^{-1} \geq 0. \tag{4.54}$$

where the following substitutions are applied:

$$\delta l = \frac{1}{\tau}-\frac{1}{\hat{\tau}}, \text{ and, } \bar{q} = \frac{2\bar{\sigma}^2}{\tau}. \tag{4.55}$$

Since $\bar{q}-q \geq 0$ must also be non-negative, the inequality direction does not change after multiplying by it. This leads to:

$$\hat{q}\bar{q}-\hat{q}q-\bar{q}q-\tau\left(\frac{1}{\hat{\tau}}-\frac{1}{\tau}\right)q\bar{q}-\frac{\tau^2}{4}\left(\frac{1}{\hat{\tau}}-\frac{1}{\tau}\right)^2\bar{q}^2 \geq 0. \tag{4.56}$$

Grouping the factors of $\bar{q}$ leads to the following quadratic inequation:

$$-\frac{\tau^2}{4}\left(\frac{1}{\hat{\tau}}-\frac{1}{\tau}\right)^2\bar{q}^2+\left(\hat{q}-\frac{\tau}{\hat{\tau}}q\right)\bar{q}-\hat{q}q \geq 0. \tag{4.57}$$

Now substituting $q=\frac{2\sigma^2}{\tau}$, $\bar{q}=\frac{2\bar{\sigma}^2}{\tau}$ and $\hat{q}=\frac{2\hat{\sigma}^2}{\hat{\tau}}$, simplifies to:

$$-\left(\frac{1}{\hat{\tau}}-\frac{1}{\tau}\right)^2\bar{\sigma}^4+\frac{\left(\hat{\sigma}^2-\sigma^2\right)}{\hat{\tau}}\frac{4}{\tau}\bar{\sigma}^2-\frac{4\hat{\sigma}^2\sigma^2}{\hat{\tau}\tau} \geq 0. \tag{4.58}$$

From the possible solutions of $\bar{\sigma}^2$, the maximum and minimum values that satisfy Equation (4.58) can be found at the roots of the equality since Equation (4.58) is a downwards parabola function for a given value of σ^2 and τ. We have the freedom to choose either of the two possible solutions. However, the maximum one allows to be tighter in the determination of $\sigma^2_{c,0}$ in Equation (4.45) and it is therefore selected. On the other hand, Equation (4.58) must be satisfied for any value of σ^2 and τ within the possible range. Therefore, we seek to find the minimum value of $\bar{\sigma}^2$ for any value of the true unknown parameters. The determination of the necessary and most suitable $\bar{\sigma}^2$ can therefore be summarised as:

$$\bar{\sigma}^2_{\min} = \min\left(\max_{\sigma^2,\tau}\bar{\sigma}^2\right). \tag{4.59}$$

Solving the quadratic equation for $\bar{\sigma}^2$ gives the following solutions:

$$\bar{\sigma}^2 = \frac{-\frac{4(\hat{\sigma}^2-\sigma^2)}{\hat{\tau}\tau} \pm \sqrt{\left(\frac{4(\hat{\sigma}^2-\sigma^2)}{\hat{\tau}\tau}\right)^2 - 16\left(\frac{1}{\hat{\tau}}-\frac{1}{\tau}\right)^2 \frac{\hat{\sigma}^2\sigma^2}{\hat{\tau}\tau}}}{-2\left(\frac{1}{\hat{\tau}}-\frac{1}{\tau}\right)^2}, \tag{4.60}$$

which can be simplified to:

$$\bar{\sigma}^2 = 2\hat{\tau}\tau \frac{\hat{\sigma}^2 - \sigma^2 \pm \sqrt{\hat{\sigma}^4 + \sigma^4 - \hat{\sigma}^2\sigma^2 \frac{\tau^2+\hat{\tau}^2}{\hat{\tau}\tau}}}{(\tau-\hat{\tau})^2}. \tag{4.61}$$

From the range values of τ, the minimum value of $\bar{\sigma}^2$ that satisfies Equation (4.58) is achieved for both limiting cases $\tau = \tau_{\min}$ and $\tau = \tau_{\max}$ when choosing $\sigma^2 = \sigma^2_{\max}$. Under these circumstances the argument of the square root term is zero and minimum $\bar{\sigma}^2$ writes:

$$\bar{\sigma}^2_{\min} = 2\sigma^2_{\max} \frac{(\tau_{\max}-\hat{\tau})\,\tau}{(\hat{\tau}-\tau)^2}, \ \forall \tau = \{\tau_{\min}, \tau_{\max}\}. \tag{4.62}$$

It can be shown that this expressions achieves the same value for $\tau_{\min}$ and $\tau_{\max}$, for instance for $\tau_{\max}$ it reads:

$$\bar{\sigma}^2_{\min} = 2\sigma^2_{\max} \frac{\tau_{\max}}{\tau_{\max}-\hat{\tau}}. \tag{4.63}$$

Coming now back to the condition for the non-stationary bound and substituting Equation (4.63) in Equation (4.45) leads to:

$$\hat{\sigma}^2_{c,0} \geq \sigma^2_{\max} + \frac{\sigma^4_{\max}(\tau_{\max}-\hat{\tau})}{2\sigma^2_{\max}\tau_{\max} - \sigma^2_{\max}(\tau_{\max}-\hat{\tau})}. \tag{4.64}$$

Substituting $\hat{\tau} = \sqrt{\tau_{\min}\tau_{\max}}$, from Equation (4.41), and rearranging, the tightest bound on $\hat{\sigma}^2_{c,0}$ is found at equality, which is:

$$\hat{\sigma}^2_{c,0} = \sigma^2_{\max} \frac{2}{1+\sqrt{\frac{\tau_{\min}}{\tau_{\max}}}}. \tag{4.65}$$

Theorem 4.3.2 (Non-stationary continuous-Time GMP Tight Bounding Model)**.**

A non-stationary GMP with $\hat{\tau} = \sqrt{\tau_{min}\tau_{max}}$ and $\hat{\sigma}^2 = \sigma^2_{max}\sqrt{\frac{\tau_{max}}{\tau_{min}}}$ and initial variance:

$$\hat{\sigma}_{c,0} = \sigma^2_{max}\frac{2}{1+\sqrt{\frac{\tau_{min}}{\tau_{max}}}} \tag{4.66}$$

guarantees bounding conditions at the steady state of the GMP uncertain process as well as provides tight error bounding conditions during the transient phase.

5 Discrete-Time Kalman Filter Bounding Models

This chapter derives the main conditions of choosing GMP model parameters that guarantee tight bounding of error covariance in estimation for the discrete version of state-space estimators such as KF. The bounds are obtained by frequency and time domain analysis. Besides, proofs of the validity of parameter models derived in Chapter 4 in continuous-time are provided for its use in discrete-time.

5.1 Bound Derivation via Spectral Density Bounding

This section presents the analysis in the power spectral density domain of the error processes to derive the tightest GMP model bounds for noises with Gauss-Markov structure in discrete-time domain.

5.1.1 Frequency Domain Bounding Introduction

A general discrete or sampled linear system can be expressed by :

$$\mathbf{x}_k = \boldsymbol{\Phi}_k \mathbf{x}_{k-1} + \mathbf{G}_k \mathbf{w}_k, \tag{5.1}$$

$$\mathbf{z}_k = \mathbf{H}_k \mathbf{x}_k + \mathbf{J}_k \mathbf{v}_k, \tag{5.2}$$

where the state vector $\mathbf{x} \in \mathbb{R}^s$, process noise $\mathbf{w} \in \mathbb{R}^p$, $\mathbf{v} \in \mathbb{R}^l$ and transition matrix $\boldsymbol{\Phi} \in \mathbb{R}^{s \times s}$ are discrete-time vectors and matrices. Equivalently, the measurement and system model can be

expressed in a batch formulation as [39]:

$$\begin{bmatrix} \tilde{\mathbf{x}}_0 \\ 0 \\ \mathbf{z}_1 \\ 0 \\ \vdots \\ \mathbf{z}_k \end{bmatrix} = \begin{bmatrix} \mathbf{I} & 0 & \cdots & \cdots & 0 \\ \boldsymbol{\Phi}_1 & -\mathbf{I} & 0 & \cdots & 0 \\ 0 & \mathbf{H}_1 & 0 & \cdots & 0 \\ 0 & \boldsymbol{\Phi}_2 & -\mathbf{I} & \cdots & 0 \\ \vdots & \vdots & \vdots & \ddots & \vdots \\ 0 & 0 & \cdots & \cdots & \mathbf{H}_k \end{bmatrix} \begin{bmatrix} \mathbf{x}_0 \\ \mathbf{x}_1 \\ \mathbf{x}_2 \\ \vdots \\ \mathbf{x}_k \end{bmatrix} + \begin{bmatrix} \boldsymbol{\nu}_0 \\ \mathbf{G}_1\mathbf{w}_1 \\ \mathbf{J}_1\mathbf{v}_1 \\ \vdots \\ \mathbf{G}_k\mathbf{w}_k \\ \mathbf{J}_k\mathbf{v}_k \end{bmatrix}, \tag{5.3}$$

where $\tilde{\mathbf{x}}_0 \in \mathbb{R}^s$ is a pseudo-measurement representing an initialization of the estimation process and ν_0 is its associated noise. Equation (5.3) can be rewritten as a compact measurement equation:

$$\mathbf{z}_\mathrm{K} = \mathbf{C}_\mathrm{K}\mathbf{x}_\mathrm{K} + \mathbf{D}_\mathrm{K}\mathbf{T}_\mathrm{K}\boldsymbol{\nu}_\mathrm{K}, \tag{5.4}$$

where K is used to denote that times 0 to k are included in the vector or matrix (or equivalently expressed as $\mathrm{K} = 0:k$), and $\mathbf{D}_\mathrm{K} \in \mathbb{R}^{s(k+1)+kl \times s+k(p+l)}$ is the block diagonal matrix

$$\mathbf{D}_\mathrm{K} = \mathrm{diag}\left\{\mathbf{I}, \mathbf{G}_1, \mathbf{J}_1, \cdots, \mathbf{G}_k, \mathbf{J}_k\right\}. \tag{5.5}$$

The matrix $\mathbf{T}_\mathrm{K} \in \mathbb{R}^{s+k(p+l) \times s+k(p+l)}$ has been introduced to reorder the noise components in $\mathbf{w}$ and $\mathbf{v}$ such that $\boldsymbol{\nu}_\mathrm{K}$ contains now the grouped time-series of the individual noises ordered within one vector:

$$\boldsymbol{\nu}_\mathrm{K} = \left[\nu_{0,1}, \cdots, \nu_{0,s}, w_{1,1}, \cdots, w_{1,k}, v_{1,1}, \cdots, v_{1,k}, \cdots, w_{p,1}, \cdots, w_{p,k}, v_{l,1}, \cdots, v_{l,k}\right]^\mathrm{T}. \tag{5.6}$$

As $\boldsymbol{\nu}_\mathrm{K}$ regroups a zero-mean Gaussian noise, a least-square (LS) estimator of Equation (5.4) is:

$$\hat{\mathbf{x}}_\mathrm{K} = \underbrace{\left(\mathbf{C}_\mathrm{K}^\mathrm{T}\mathbf{W}\mathbf{C}_\mathrm{K}\right)^{-1}\mathbf{C}_\mathrm{K}^\mathrm{T}\mathbf{W}}_{\mathbf{S}_\mathrm{K}}\mathbf{z}_\mathrm{K}, \tag{5.7}$$

with weighting matrix $\mathbf{W}$ chosen as $\mathbf{W} = \left(\mathbf{D}_\mathrm{K}\mathbf{T}_\mathrm{K}\mathbf{N}_\mathrm{K}\mathbf{T}_\mathrm{K}^\mathrm{T}\mathbf{D}_\mathrm{K}^\mathrm{T}\right)^{-1}$, where $\mathbf{N}_\mathrm{K} = \mathrm{E}[\boldsymbol{\nu}_\mathrm{K}\boldsymbol{\nu}_\mathrm{K}^\mathrm{T}]$ is the covariance of the full noise vector. Note that the the batch estimator $\mathbf{S}_\mathrm{K}$ will produce the same estimate $\hat{\mathbf{x}}_\mathrm{K}$ at the instant k as a Kalman filter, such that $\hat{\mathbf{x}}_k = \mathbf{x}_{k|k}$. It is also possible to obtain the Kalman filter estimator from $\mathbf{S}_\mathrm{K}$ for all time epochs by making the elements of the upper

triangular part of $\mathbf{S}_K$ zeros. That is, if the batch least-square estimator is:

$$\mathbf{S}_K = \begin{bmatrix} s_{11} & s_{12} & \cdots & s_{1k} \\ s_{21} & s_{22} & \cdots & s_{2k} \\ \vdots & \vdots & \ddots & \vdots \\ s_{k1} & s_{k2} & \cdots & s_{kk} \end{bmatrix}, \tag{5.8}$$

the Kalman filter estimator for all times up to time k is:

$$\mathbf{S}_{KF,K} = \begin{bmatrix} s_{11} & 0 & \cdots & 0 \\ s_{21} & s_{22} & \cdots & 0 \\ \vdots & \vdots & \ddots & \vdots \\ s_{k1} & s_{k2} & \cdots & s_{kk} \end{bmatrix}, \tag{5.9}$$

and therefore $\hat{\mathbf{x}}_{KF,K} = \mathbf{S}_{KF,K}\mathbf{z}_K$ is the Kalman filter estimate for all time epochs.

The transformation of estimator matrix to the *all-times Kalman filter* is not critical since Equation (5.8) and Equation (5.9) show that both estimators are the same for the current time k and one could select k arbitrary. In fact, the conclusions of this section and chapter are equally valid for both batch least-squares, Kalman filter or any other linear estimator.

The covariance of the estimation error of $\hat{\mathbf{x}}_{KF,K}$ can be now computed for a given estimator (KF in this case) as:

$$\mathrm{Cov}[\hat{\mathbf{x}}_{KF,K}] = \mathbf{P}_K = \mathbf{S}_{KF,K}\mathbf{N}_K\mathbf{S}_{KF,K}^T. \tag{5.10}$$

The noise components in $\mathbf{v}$ can be considered independent in most applications (e.g., coming from different GNSS pseudorange errors). Therefore, the covariance matrix $\mathbf{N}$ is a block diagonal matrix containing the initial filter covariance and the autocovariance matrix of each of the noise components:

$$\mathbf{N}_K = \mathrm{diag}\left\{ \mathbf{P}_0, \quad \mathbf{R}_1, \quad \mathbf{R}_2, \quad \cdots, \quad \mathbf{R}_{n_K} \right\}, \tag{5.11}$$

where $\mathbf{R}_i$ is the autocovariance matrix of the i^{th} noise component in $\mathbf{v}$ which can be either one of the noise process of $\mathbf{w}$ or $\mathbf{v}$, depending on their specific position.

In order to overbound the variance of the KF estimated error so it reflects the uncertainty of noise parameters, the *designed KF* must produce a covariance matrix $\hat{\mathbf{P}}$ that overbounds the true covariance matrix $\mathbf{P}$. The overbounding of covariance matrix is defined such that the difference $\hat{\mathbf{P}} - \mathbf{P} \geq \mathbf{0}$ is positive semidefinite.

For a fixed estimator and according to Equation (5.10), this implies directly that the designed covariance matrix $\hat{\mathbf{N}}$ must be greater than the true one $\hat{\mathbf{N}} \geq \mathbf{N}$. And equivalently, $\hat{\mathbf{P}}(0) \geq \mathbf{P}(0)$ and $\hat{\mathbf{R}}_i \geq \mathbf{R}_i,\ \forall i$ must be guaranteed.

Since the individual autocovariance matrix of each of the noise process are Toeplitz matrix, the latter condition reduces to guaranteeing that the difference of the autocovariance sequences is a positive sequence [73]. For stationary processes, Einstein-Wiener-Khinchin theorem states that the autocovariance function and the Power Spectral Density (PSD) are Fourier pairs [55]. In discrete domain, the spectral density can be obtained from the autocovariance sequence as an infinity sum:

$$\mathrm{S_d}(\omega) = \sum_{n=-\infty}^{\infty} r[n] e^{-j\omega n}, \tag{5.12}$$

where ω is defined only in $[0, \pi]$ due to Nyquist limit. Conversely, the autocovariance sequence can be obtained from the discrete spectral density from the inverse discrete Fourier transform as:

$$r[n] = \int_{-\pi}^{\pi} e^{j\omega n} \mathrm{S_d}(\omega) d\omega, \tag{5.13}$$

since the process noises in our case are all related to real time valued signals and $\mathrm{S}_d(\omega)$ is an even function, it is enough to integrate over $\omega \in [0, \pi]$. Under some regularity conditions, the condition $\hat{\mathbf{R}} \geq \mathbf{R}$ is therefore satisfied when $\hat{\mathrm{S}}_\mathrm{d}(\omega) \geq \mathrm{S_d}(\omega),\ \forall \omega \in [0, \pi]$ [99]. The proof is provided in Appendix B.2.

Note that assuming that the discrete PSD is known, this condition is sufficient to produce an upper bound on the KF variance independently on the time a measurement is used in the KF or similarly, the equivalent length of the autocovariance sequence needed for the filter when considering the batch KF formulation. Theorem 5.1.1 summarizes the criteria for KF bounding based on frequency domain bounding.

Theorem 5.1.1 (Frequency Domain Bounding in Discrete-time)**.**

A Kalman filter estimated error covariance in discrete-time $\hat{\mathbf{P}}$ that upper bounds the true error covariance $\mathbf{P}$ can be obtained when designing the filter autocovariances $\hat{\mathbf{R}}_i$ for all noise processes i such that its equivalent Power Spectral Density (PSD) $\hat{\mathrm{S}}_\mathrm{d}(\omega)$ bounds the true PSD $\mathrm{S_d}(\omega)$.

$$\hat{\mathrm{S}}_\mathrm{d}(\omega) \geq \mathrm{S_d}(\omega),\ \forall \omega \in [0, \pi] \longrightarrow \hat{\mathbf{R}} \geq \mathbf{R} \longrightarrow \hat{\mathbf{P}} \geq \mathbf{P} \tag{5.14}$$

In the next section, the condition in Equation (5.14) is used to derive tight bounds for the case of Gauss-Markov process with uncertain parameters.

5.1.2 Stationary Discrete-Time GMP Model

Problem formulation

A discrete-time GMP model with $\hat{\tau}_d$ time constant and variance $\hat{\sigma}_d^2$ that ensures bounding condition on the estimation error can be written at any time epoch $n \in \mathbb{Z} \geq 0$ as:

$$a_n = \hat{\alpha}_d a_{n-1} + \sqrt{\hat{\sigma}_d^2 \left(1 - \hat{\alpha}_d^2\right)} w_n, \tag{5.15}$$

where $\hat{\alpha} = e^{\frac{-\Delta t}{\hat{\tau}_d}}$, $w_n \sim \mathcal{N}(0,1)$ $\Delta t \in \mathbb{R}_{>0}$ is the sampling time interval.

As shown in Section 5.1.1, in order to bound estimation error in sequential or batch type estimators, the spectral density of the model must be greater than or equal to the spectral density of the actual noise components S_d:

$$\hat{S}_d(\omega) \geq S_d(\omega), \ \forall \omega \in [0, \frac{\pi}{\Delta t}] \tag{5.16}$$

In the case that the model and underlying noise are Gauss-Markov processes, Equation (5.16) is a starting point to determine the values of $\hat{\tau}_d$ and k_d that produce the tightest estimation error variance bound. This is achieved by seeking to minimize the total net power of the process which is its variance $\hat{\sigma}_d^2$.

Discrete-time Model Derivation

The spectral density of a generic discrete-time first-order GMP can be expressed as [101]:

$$S_d(\omega) = \frac{\sigma^2 \Delta t \left(1 - \alpha^2\right)}{1 + \alpha^2 - 2\alpha \cos(\omega \Delta t)}, \tag{5.17}$$

where $\alpha = e^{\frac{-\Delta t}{\tau}}$. Based on the definition in Eq. (5.17), the condition in Equation (5.16) for all $\omega \in [0, \frac{\pi}{\Delta t}]$ must satisfy the inequality:

$$\frac{\hat{\sigma}_d^2 \Delta t \left(1 - \hat{\alpha}_d^2\right)}{1 + \hat{\alpha}_d^2 - 2\hat{\alpha}_d \cos(\omega \Delta t)} \geq \frac{\sigma^2 \Delta t \left(1 - \alpha^2\right)}{1 + \alpha^2 - 2\alpha \cos(\omega \Delta t)}. \tag{5.18}$$

After bringing the right-hand-side term to the left, expressing the two fractions with a common denominator, and dividing both sides by Δt, Equation (5.18) becomes:

$$\begin{aligned}&\frac{\hat{\sigma}_d^2\left(1-\hat{\alpha}_d^2\right)\left(1+\alpha^2-2\alpha\cos(\omega\Delta t)\right)}{\left(1+\hat{\alpha}_d^2-2\hat{\alpha}_d\cos(\omega\Delta t)\right)\left(1+\alpha^2-2\alpha\cos(\omega\Delta t)\right)}\\&-\frac{\sigma^2\left(1-\alpha^2\right)\left(1+\hat{\alpha}_d^2-2\hat{\alpha}_d\cos(\omega\Delta t)\right)}{\left(1+\hat{\alpha}_d^2-2\hat{\alpha}_d\cos(\omega\Delta t)\right)\left(1+\alpha^2-2\alpha\cos(\omega\Delta t)\right)}\geq 0,\\&\forall\omega\in[0,\frac{\pi}{\Delta t}].\end{aligned}\tag{5.19}$$

The second order polynomials appearing in the denominators are of the form $x^2-2x\cos(\omega\Delta t)+1$. That is, they are parabolas that open up with a minimum value of $1-\cos^2\omega\Delta t$ occurring at $x^*=\cos\omega\Delta t$. Given that $\cos(\omega\Delta t)\in[-1,1]$, the minimum value is always positive, and since the parabolas open up, it must be that the denominators in Equation (5.19) are also positive. Therefore, Equation (5.19) is satisfied if and only if the numerator is non-negative, which, after factoring out $\cos(\omega\Delta t)$, can be written as:

$$\cos(\omega\Delta t)\left(\sigma^2(1-\alpha^2)2\hat{\alpha}_d-\hat{\sigma}_d^2(1-\hat{\alpha}_d^2)2\alpha\right)+\hat{\sigma}_d^2(1-\hat{\alpha}_d^2)(1+\alpha^2)-\sigma^2(1-\alpha^2)(1+\hat{\alpha}_d^2)\geq 0,\tag{5.20}$$

Equation (5.20) is linear in $\cos(\omega\Delta t)$, which can be written independently of Δt as $\cos(\Omega)$ where $\Omega=\omega\Delta t,\ \forall\Omega\in[0,\pi]$. The term $\cos(\omega\Delta t)$ is a monotonically decreasing function of $\omega\Delta t$ for $\omega\in[0,\pi/\Delta t]$. Thus, showing that the inequality in Equation (5.20) is satisfied $\forall\omega\in[0,\frac{\pi}{\Delta t}]$ is equivalent to showing that it is satisfied for the limit values of $\cos(\omega\Delta t)$. For $\cos(\omega\Delta t)=1$, Equation (5.20) becomes:

$$\hat{\sigma}_d^2\geq\sigma^2\frac{(1+\alpha)(1-\hat{\alpha}_d)}{(1-\alpha)(1+\hat{\alpha}_d)}.\tag{5.21}$$

For $\cos(\omega\Delta t)=-1$, Equation (5.20) becomes:

$$\hat{\sigma}_d^2\geq\sigma^2\frac{(1-\alpha)(1+\hat{\alpha}_d)}{(1+\alpha)(1-\hat{\alpha}_d)}.\tag{5.22}$$

Equation (5.21) and Equation (5.22) must be satisfied $\forall\sigma^2\in[\sigma^2_{min},\sigma^2_{max}]$. Choosing $\sigma^2=\sigma^2_{max}$ ensures that Equation (5.21) and Equation (5.22) are satisfied for any other value of σ^2 within the admissible range.

In addition, Equation (5.21) and Equation (5.22) must hold for all values of α, i.e., $\forall\tau\in[\tau_{min},\tau_{max}]$. In Equation (5.21), the maximum value of the right-hand-side is for $\alpha=\alpha_{max}$, which maximizes the numerator while minimizing the denominator because $0<\alpha<1$. Similarly, in Equation (5.22), the maximum value of the right-hand-side is for $\alpha=\alpha_{min}$. Furthermore, the tightest PSD bound is found when $\hat{\sigma}_d^2$ is minimized, which is achieved at equality in

Equation (5.21) and Equation (5.22). The following two equations are derived:

$$\hat{\sigma}_d^2 = \sigma_{max}^2 \frac{(1+\alpha_{max})(1-\hat{\alpha}_d)}{(1-\alpha_{max})(1+\hat{\alpha}_d)}, \tag{5.23}$$

$$\hat{\sigma}_d^2 = \sigma_{max}^2 \frac{(1-\alpha_{min})(1+\hat{\alpha}_d)}{(1+\alpha_{min})(1-\hat{\alpha}_d)}. \tag{5.24}$$

Solving for $\hat{\alpha}_d$ and $\hat{\sigma}_d^2$ in Equation (5.23) and Equation (5.24), a discrete-time, stationary, first-order GMP model that bounds the PSD of the uncertain GMP is found with the parameters in Equation (5.25) and Equation (5.26).

Theorem 5.1.2 (Discrete-time stationary GMP Tight Bounding Model)**.**

The stationary discrete-time GMP model that provides the tightest bound on an actual GMP with uncertain but bounded variance $\sigma^2 \in [\sigma_{min}^2, \sigma_{max}^2]$ and time constant $\tau \in [\tau_{min}, \tau_{max}]$ is determined by the following time correlation constant and variance:

$$\hat{\sigma}_d^2 = \sigma_{max}^2 \sqrt{\frac{(1-\alpha_{min})(1+\alpha_{max})}{(1+\alpha_{min})(1-\alpha_{max})}}, \text{ and} \tag{5.25}$$

$$\hat{\tau}_d = -\Delta t \left[\ln\left(\frac{1-\sqrt{\Gamma}}{1+\sqrt{\Gamma}} \right) \right]^{-1}, \tag{5.26}$$

where

$$\alpha_{min} = e^{-\frac{\Delta_t}{\tau_{min}}}, \ \alpha_{max} = e^{-\frac{\Delta_t}{\tau_{max}}}, \text{ and} \tag{5.27}$$

$$\Gamma = \frac{(1-\alpha_{min})(1-\alpha_{max})}{(1+\alpha_{min})(1+\alpha_{max})}. \tag{5.28}$$

Figure 5.1 shows the PSD of different GMPs with the limit values of time-correlation constant and variance within its range along with the new GMP model parameters.

5.1.3 Using Discrete-Time Models with Parameters values derived in continuous time

In Section 5.1.2 and Section 4.2.1 two different expressions were derived using frequency domain overbounding in the discrete and continuous domain, respectively.

It can be shown that the expressions for $\hat{\tau}_d$ and $\hat{\sigma}_d^2$ in Equation (5.26) and Equation (5.25) tend

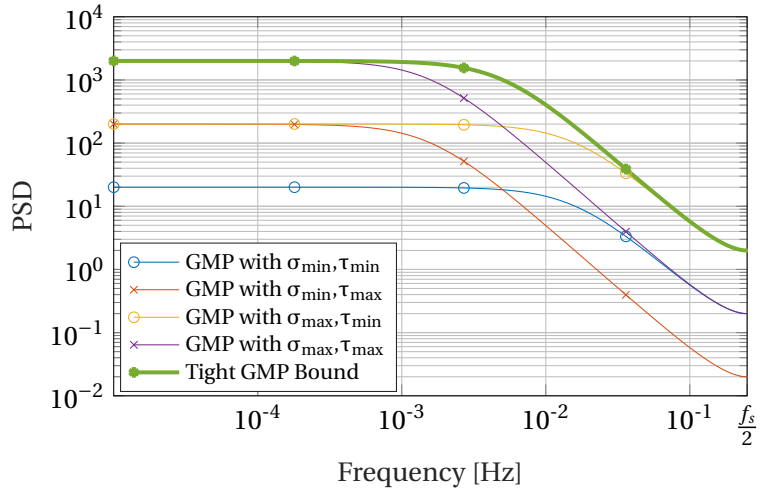

Figure 5.1: Discrete-time Power Spectral Density (PSD) of stationary GMP with $\sigma^2 \in [1,10]$ and $\tau \in [10,100]s$, and New Tight Bound.

to their continuous counter part when $\Delta t \to 0$, and already in particular when $\Delta t << \tau_{\text{min}}$:

$$\lim_{\Delta t \to 0} \hat{\sigma}_{\text{d}} = \hat{\sigma}_{\text{c}}, \tag{5.29}$$

$$\lim_{\Delta t \to 0} \hat{\tau}_{\text{d}} = \hat{\tau}_{\text{c}}. \tag{5.30}$$

Therefore, for some practical applications the model parameters in Equation (4.41) derived in the continuous time domain might be more attractive to use given their compact expressions. This section proofs that using the model parameters derived for continuous-time in a discrete-time model also produces bounding conditions independently of the sampling interval Δt. The proof reduces to show that the spectral density of a GMP using $\hat{\sigma}_{\text{c}}, \hat{\tau}_{\text{c}}$ upper bounds the PSD of the GMP using $\hat{\sigma}_{\text{d}}, \hat{\tau}_{\text{d}}$ for all Δt. This can be expressed mathematically as:

$$\frac{\hat{\sigma}_{\text{c}}^2 \Delta t \left(1-\hat{\alpha}_{\text{c}}^2\right)}{1+\hat{\alpha}_{\text{c}}^2 - 2\hat{\alpha}_{\text{c}} \cos(\omega \Delta t)} \geq \frac{\hat{\sigma}_{\text{d}}^2 \Delta t \left(1-\hat{\alpha}_{\text{d}}^2\right)}{1+\hat{\alpha}_{\text{d}}^2 - 2\hat{\alpha}_{\text{d}} \cos(\omega \Delta t)}, \forall \Delta t \geq 0 \tag{5.31}$$

The inequality in Equation (5.31) is of the same form as that in Equation (5.18). Thus, following the same steps as in Equation (5.18) to Equation (5.22), it can be shown that Equation (5.31) is true if and only if the following two inequalities are satisfied for all $\Delta t \geq 0$:

$$\hat{\sigma}_{\text{c}}^2 \frac{(1+\hat{\alpha}_{\text{c}})}{(1-\hat{\alpha}_{\text{c}})} \geq \hat{\sigma}_{\text{d}}^2 \frac{(1+\hat{\alpha}_{\text{d}})}{(1-\hat{\alpha}_{\text{d}})}, \tag{5.32}$$

$$\hat{\sigma}_{\text{c}}^2 \frac{(1-\hat{\alpha}_{\text{c}})}{(1+\hat{\alpha}_{\text{c}})} \geq \hat{\sigma}_{\text{d}}^2 \frac{(1-\hat{\alpha}_{\text{d}})}{(1+\hat{\alpha}_{\text{d}})}. \tag{5.33}$$

Substituting the expressions of $\hat{\sigma}_{\text{d}}^2$ in Equation (5.23) and Equation (5.24) into Equation (5.32)

and Equation (5.33), respectively, using the definition of $\hat{\sigma}_c^2$ in Equation (4.41) and dividing both sides by σ_{max}^2, the last two inequalities become:

$$\sqrt{\frac{\tau_{max}}{\tau_{min}}}\frac{(1+\hat{\alpha}_c)}{(1-\hat{\alpha}_c)} \geq \frac{(1+\alpha_{max})}{(1-\alpha_{max})}, \tag{5.34}$$

$$\sqrt{\frac{\tau_{max}}{\tau_{min}}}\frac{(1-\hat{\alpha}_c)}{(1+\hat{\alpha}_c)} \geq \frac{(1-\alpha_{min})}{(1+\alpha_{min})}. \tag{5.35}$$

Multiplying both sides of these inequalities by $\sqrt{\tau_{max}\tau_{min}} = \hat{\tau}_c$, bringing all terms to the left-hand side, expanding, factoring out $(\tau_{max} - \hat{\tau}_c)$ and $(\tau_{max} + \hat{\tau}_c)$, and rearranging, lead to the following expressions:

$$f_1(\Delta t) = (\tau_{max} - \hat{\tau}_c)(1 - \alpha_{max}\hat{\alpha}_c) + (\tau_{max} + \hat{\tau}_c)(\hat{\alpha}_c - \alpha_{max}), \tag{5.36}$$

$$f_2(\Delta t) = (\tau_{max} - \hat{\tau}_c)(1 - \alpha_{min}\hat{\alpha}_c) + (\tau_{max} + \hat{\tau}_c)(\alpha_{min} - \hat{\alpha}_c). \tag{5.37}$$

Substituting the definitions of $\hat{\alpha}_c$, α_{min} and α_{max} into the above two expressions, the following limits are found:

$$\lim_{\Delta t \to 0} f_1(\Delta t) = 0, \qquad \lim_{\Delta t \to 0} f_2(\Delta t) = 0. \tag{5.38}$$

Equation (5.31) is satisfied if and only if $f_1(\Delta t) \geq 0$ and $f_2(\Delta t) \geq 0, \forall \Delta t \geq 0$. Given Equation (5.38), this is equivalent to showing that $f_1(\Delta t)$ and $f_2(\Delta t)$ are monotonically increasing, i.e., that their derivatives are non-negative for all $\Delta t \geq 0$.

First, the derivative of $f_1(\Delta t)$ can be written as:

$$f_1'(\Delta t) = \frac{(\tau_{max} - \hat{\tau}_c)(\tau_{max} + \hat{\tau}_c)}{\tau_{max}\hat{\tau}_c} e^{-\frac{\Delta t}{\tau_{max}}} e^{-\frac{\Delta t}{\hat{\tau}_c}} + \frac{(\tau_{max} + \hat{\tau}_c)}{\tau_{max}\hat{\tau}_c}\left(\hat{\tau}_c e^{-\frac{\Delta t}{\tau_{max}}} - \tau_{max} e^{-\frac{\Delta t}{\hat{\tau}_c}}\right) \geq 0. \tag{5.39}$$

Dividing both sides of the inequality by the non-negative factor $e^{-\frac{\Delta t}{\tau_{max}}} e^{-\frac{\Delta t}{\hat{\tau}_c}} \frac{\tau_{max}+\hat{\tau}_c}{\tau_{max}\hat{\tau}_c}$ and rearranging, the left-hand side in Equation (5.39) becomes:

$$f_{1,1}(\Delta t) = \hat{\tau}_c\left(e^{\frac{\Delta t}{\hat{\tau}_c}} - 1\right) - \tau_{max}\left(e^{\frac{\Delta t}{\tau_{max}}} - 1\right). \tag{5.40}$$

To show that $f_{1,1}$ is non-negative, consider the facts that:

$$\lim_{\Delta t \to 0} f_{1,1}(\Delta t) = 0 \tag{5.41}$$

and that the derivative of $f_{1,1}$ is positive, i.e.:

$$f'_{1,1}(\Delta t) = e^{\frac{\Delta t}{\hat{\tau}_c}} - e^{\frac{\Delta t}{\tau_{max}}} \geq 0, \ \forall \Delta t \geq 0, \tag{5.42}$$

because $\tau_{max} \geq \hat{\tau}_c$. This proves that $f'_1(\Delta t)$ is non-negative.

Second, the derivative of $f_2(\Delta t)$ is:

$$f'_2(\Delta t) = \frac{(\tau_{max} - \hat{\tau}_c)(\tau_{min} + \hat{\tau}_c)}{\tau_{min}\hat{\tau}_c} e^{-\frac{\Delta t}{\tau_{min}}} e^{-\frac{\Delta t}{\hat{\tau}_c}} + \frac{(\tau_{max} + \hat{\tau}_c)}{\tau_{min}\hat{\tau}_c} \left(\tau_{min} e^{-\frac{\Delta t}{\hat{\tau}_c}} - \hat{\tau}_c e^{-\frac{\Delta t}{\tau_{min}}} \right) \geq 0. \tag{5.43}$$

Dividing both sides of the inequality by the non-negative factor $\left(e^{-\frac{\Delta t}{\tau_{min}}} e^{-\frac{\Delta t}{\hat{\tau}_c}} \frac{1}{\tau_{max}\hat{\tau}_c} \right)$ and rearranging, the left-hand side in Equation (5.43) becomes:

$$f_{2,1}(\Delta t) = \tau_{max}\tau_{min}\left(e^{\frac{\Delta t}{\tau_{min}}} + 1 \right) - \tau_{max}\hat{\tau}_c\left(e^{\frac{\Delta t}{\hat{\tau}_c}} - 1 \right) + \hat{\tau}_c\tau_{min}\left(e^{\frac{\Delta t}{\tau_{min}}} - 1 \right) - \hat{\tau}_c^2\left(e^{\frac{\Delta t}{\hat{\tau}_c}} + 1 \right) \geq 0. \tag{5.44}$$

To show that $f_{2,1}$ is non-negative, consider similarly the fact that:

$$\lim_{\Delta t \to 0} f_{2,1}(\Delta t) = 2\tau_{max}\tau_{min} - 2\hat{\tau}_c^2 = 0, \tag{5.45}$$

and that the derivative of $f_{2,1}(\Delta t)$ is:

$$f'_{2,1}(\Delta t) = (\tau_{max} + \hat{\tau}_c)\left(e^{\frac{\Delta t}{\tau_{min}}} - e^{\frac{\Delta t}{\hat{\tau}_c}} \right) \geq 0 \tag{5.46}$$

because $\tau_{min} \leq \hat{\tau}_c$. This proves that $f'_2(\Delta t)$ is non-negative.

The facts that $f'_1(\Delta t)$ and $f'_2(\Delta t)$ are also non-negative for all $\Delta t \geq 0$ and that the limits of $f_1(\Delta t)$ and $f_2(\Delta t)$ as $\Delta t \to 0$ are non-negative prove that $f_1(\Delta t) \geq 0$ and $f_2(\Delta t) \geq 0, \forall \Delta t \geq 0$, which ultimately proves Equation (5.31). The GMP model with parameters derived in continous-time provide similar bounding behaviour as the discrete-time ones. Only in situations where Δt approached or exceeded τ_{min}, did the continuous-time GMP model become more conservative than the discrete-time model. Nevertheless, in most practical problems, where Δt is smaller than τ_{min}, the process would be better modeled as a white noise and not as a time-correlated GMP. Figure (5.2) shows the difference in total net power between the bound derived using the continuous-time PSD (Equation (4.41) and the bound derived using the discrete-time PSD expressions (Equation (5.25) and Equation (5.26)) when used in a discrete KF with different interval sampling. Figure (5.2) shows that for sampling intervals which are smaller than the minimum GM time constant $\Delta t << \tau_{min}$, both bounds offer similar results.

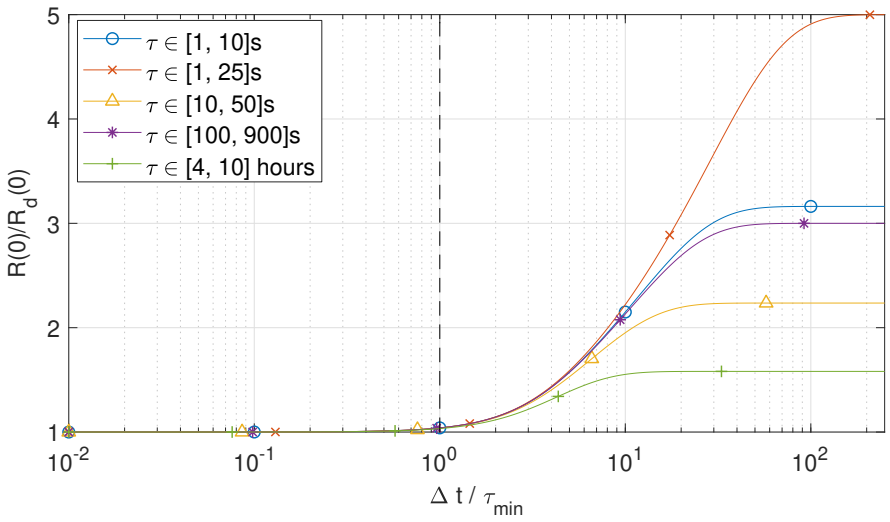

Figure 5.2: Difference in Power of Continuous and Discrete Derived Stationary Bounds for different sampling interval

For this reason it is therefore suggested to use the continuous expressions because of their simplicity. Only in cases when the sampling interval Δt approaches $\tau_{\min}$ the continuous-time derived bound becomes extremely conservative.

Remark (when $\tau_{\min} = 0$)

An interesting situation when the more complex expression of the discrete-time PSD bound are necessary to be used is in the case that $\tau_{\min} = 0$. In this case, note that the stationary bound obtained in the continuous-time cannot be used. That is:

$$\lim_{\tau_{\min}\to 0} \hat{\sigma}_c^2 = \sigma_{\max}^2 \sqrt{\frac{\tau_{\max}}{\tau_{\min}}} = \infty. \tag{5.47}$$

Therefore, when $\tau \in [0, \tau_{\max}]$, the discrete-time form can be used to properly define a suitable bound. In this case note that:

$$\hat{\sigma}_d^2 = \sigma_{\max}^2 \sqrt{\frac{(1+\alpha_{\max})}{(1-\alpha_{\max})}} = \sigma_{\max}^2 \underbrace{\sqrt{\frac{(1+e^{-\frac{\Delta_t}{\tau_{\max}}})}{(1-e^{-\frac{\Delta_t}{\tau_{\max}}})}}}_{k_d(\tau_{\min}=0)}, \quad \text{and} \tag{5.48}$$

$$\hat{\tau}_d = -\Delta t \left[\ln\left(\frac{1-k_d^{-1}}{1+k_d^{-1}} \right) \right]^{-1}. \tag{5.49}$$

5.2 Non-Stationary GMP Model

In this section, two approaches are presented to obtain the minimum initial variance σ_0^2 of a non-stationary GMP that still satisfies bounding condition on the estimation error in discrete-time while providing tighter error bounding during a first transient phase. The first is derived analytically following a similar approach as in Section 4.3. The second one is a numerical solution that yields even tighter bounding in certain practical situations.

5.2.1 Analytical Solution

Following a similar approach as in the continuous-time case of Sec. 4.3 and based on Appendix A.1 and A.2, KF bounding conditions in discrete-time domain can be obtained via sensitivity analysis:

$$\begin{aligned} \boldsymbol{\Sigma}_{k|k-1} - \mathbf{P}_{k|k-1} \geq 0, \forall k \in [1, \infty), \\ \boldsymbol{\Sigma}_0 - \mathbf{P}_0 \geq 0. \end{aligned} \tag{5.50}$$

The conditions in Equation (5.50) are the discrete-time version of Equation (4.18). While still satisfying bounding conditions at steady state, it is possible to design the KF filter augmented states with non-stationary time-correlated GMP models that are tighter at the initial transient phase. This is imposed by the second condition in Equation (5.50), which can be written in a similar manner to Equation (4.42) as:

$$\begin{bmatrix} \boldsymbol{\Sigma}_{\xi,0} - \mathbf{P}_{\xi,0} & \mathbf{0} & \mathbf{0} \\ \mathbf{0} & \hat{\boldsymbol{\Sigma}}_{\mathrm{a},0} - \mathbf{P}_{\mathrm{a},0} & \mathbf{P}_{\mathrm{a},0} \\ \mathbf{0} & \mathbf{P}_{\mathrm{a},0} & \bar{\boldsymbol{\Sigma}}_{\mathrm{a},0} - \mathbf{P}_{\mathrm{a},0} \end{bmatrix} \geq \mathbf{0}. \tag{5.51}$$

Following the same reasoning as in Section 4.3, the above relation reduces to:

$$\hat{\sigma}_{\mathrm{d},0}^2 \geq \sigma^2 + \frac{\sigma^4}{\bar{\sigma}_{\mathrm{d}}^2 - \sigma^2}, \tag{5.52}$$

for each of the GMP time correlated processes under consideration. Appendix A.2 shows that for the GMP parameters in Equation (5.25) and Equation (5.26), the minimum of the stationary variance $\bar{\sigma}_{\mathrm{d}}^2$ (with respect to the unknown parameters σ^2 and τ) can be expressed in the discrete case as:

$$\bar{\sigma}_{\mathrm{d,min}}^2 = \frac{(1-\hat{\alpha}_{\mathrm{d}}^2)(1-\alpha_{\max}^2)}{2(\hat{\alpha}_{\mathrm{d}} - \alpha_{\max})^2}(\hat{\sigma}_{\mathrm{d}}^2 - \sigma_{\max}^2). \tag{5.53}$$

Using the expressions of $\hat{\sigma}_{\mathrm{d}}^2$ and $\hat{\tau}_{\mathrm{d}}$ in Equation (5.25) and Equation (5.26), respectively, and substituting Equation (5.53) in Equation (5.52) leads to:

$$\hat{\sigma}_{\mathrm{d},0}^2 = \sigma_{\max}^2 \frac{1}{1 - \frac{2(\hat{\alpha}_{\mathrm{d}} - \alpha_{\max})^2}{(1-\hat{\alpha}_{\mathrm{d}}^2)(1-\alpha_{\max}^2)(k_{\mathrm{d}}-1)}}, \tag{5.54}$$

where

$$k_{\mathrm{d}} = \sqrt{\frac{(1-\alpha_{\min})(1+\alpha_{\max})}{(1+\alpha_{\min})(1-\alpha_{\max})}}. \tag{5.55}$$

and where $\sigma^2 = \sigma_{\max}^2$ has been chosen to satisfy Equation (5.52) for any value of σ^2 within the possible range.

Theorem 5.2.1 (Non-stationary Discrete-Time GMP Tight Bounding Model)**.**

A non-stationary GMP with and initial variance:

$$\hat{\sigma}_{\mathrm{d},0}^2 = \sigma_{\max}^2 \frac{1}{1 - \frac{2(\hat{\alpha}_{\mathrm{d}} - \alpha_{\max})^2}{(1-\hat{\alpha}_{\mathrm{d}}^2)(1-\alpha_{\max}^2)(k_{\mathrm{d}}-1)}}, \tag{5.56}$$

where

$$k_{\mathrm{d}} = \sqrt{\frac{(1-\alpha_{\min})(1+\alpha_{\max})}{(1+\alpha_{\min})(1-\alpha_{\max})}} \tag{5.57}$$

guarantees bounding conditions at the steady state of the GMP uncertain process as well as provides tight error bounding conditions during the transient phase.

Figure 5.3 shows the different values of $\hat{\sigma}_0^2$ for different ranges of τ-values where we can see the impact of Δt in the initial variance of the tight non-stationary GMP model.

5.2.2 Discrete Non-stationary Model using Parameters Derived in Continuous-time

In Section 5.1.3 it was proven that at stationary regime the GMP parameters derived in continuous-time would provide also a bound when used in discrete-time GMP models. For completeness, this section extend the use of parameters derived in the continuous-time domain to also non-stationary discrete-time GMP models. The proof reduces to showing that the second condition in Equation (5.50) holds when the initial variance in Equation (4.65) is used. This is equivalent to showing that $\hat{\sigma}_{\mathrm{c},0}^2$ in Equation (4.65) is larger or equal to $\hat{\sigma}_{\mathrm{d},0}^2$ when

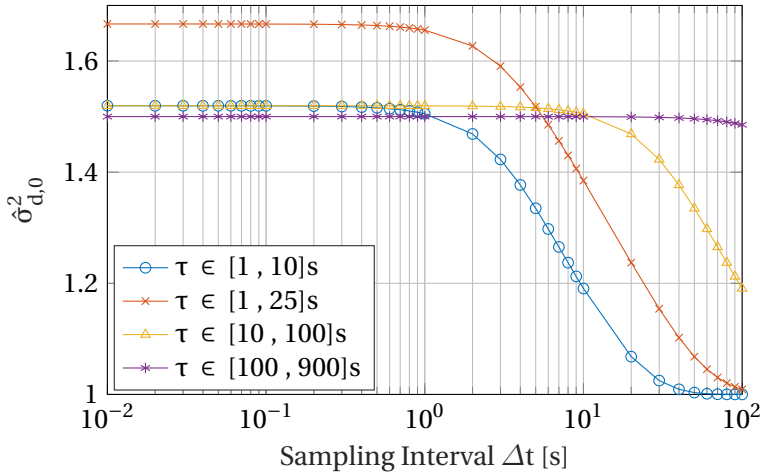

Figure 5.3: Initial variance of non-stationary GMP bounding model for different τ-ranges and $\sigma^2_{max} = 1$.

the parameters derived in the continuous-time domain (Equation (4.41)) are used, i.e.:

$$\hat{\sigma}^2_{c,0} \geq \hat{\sigma}^2_{d,0}(\hat{\sigma}^2_c, \hat{\tau}_c), \forall \Delta t > 0. \tag{5.58}$$

Comparing the original expressions of $\hat{\sigma}^2_{c,0}$ and $\hat{\sigma}^2_{d,0}$ from Equation (4.45) and Equation (5.52), Equation (5.58) is ensured if and only if the minimum values on the $\bar{\sigma}^2$ satisfy:

$$\bar{\sigma}^2_{c,min} \leq \bar{\sigma}^2_{d,min}(\hat{\sigma}^2_c, \hat{\tau}_c), \forall \Delta t > 0. \tag{5.59}$$

The reader can find the proof of Equation (5.59) in Appendix A.3, which ultimately proofs Equation (5.58) and therefore the claim of this section.

5.2.3 Numerical Solution for Time-limited GMP

Section 5.2.3 provided an expression for the initial variance of a non-stationary discrete-time GMP bounding process. That non-stationary GMP model is valid for any duration of a certain measurement or system process used within the KF filtering. However, in some applications, time-correlated measurements are only possible to be used within a certain time duration (e.g., GPS satellites are typically only visible for a maximum of 12 hours from a static observer). In this section, an additional approach is provided to compute the initial variance of a discrete-time non-stationary GMP bound use of which is expected to be limited in time. The new numerically computed initial variance will provide an even tighter bound at a certain cost of the necessary numerical solver. This new model will still match the stationary one at steady state, but will provide a tighter estimation for error variance bound during the transient period.

Consider the autocovariance r_{np} of a non-stationary discrete-time GMP model between any two time steps n and p where $n \in \mathbb{Z} \geq 0, p \in \mathbb{Z} \geq 0$ and $p \geq n$. r_{np} is defined as:

$$r_{np} = \mathrm{E}[a_n a_p^{\mathrm{T}}] = \hat{\alpha}^{n+p}\sigma_0^2 + \hat{\sigma}^2(1-\hat{\alpha}^{2n})\hat{\alpha}^{p-n}, \tag{5.60}$$

where $\hat{\alpha} = e^{\frac{-\Delta_t}{\hat{\tau}}}$, $a_0 \sim \mathcal{N}(0, \sigma_0^2)$, and $w_n \sim \mathcal{N}(0,1)$. The derivation of this expression for a general non-stationary GMP can be found in Appendix A.4. Without loss of generality the values of $\hat{\alpha}$ and $\hat{\sigma}^2$ can be either the ones derived in the continuous or in the discrete time domain.

A numerical approach is used to find the minimum value of σ_0^2 that still guarantees an upper bound on the estimation error variance. The value of σ_0^2 only needs to be determined once for each noise component, i.e., for each range of $\sigma^2 \in [\sigma^2_{\min}, \sigma^2_{\max}]$ and $\tau \in [\tau_{\min}, \tau_{\max}]$. This process can be performed offline, so prior to KF initialization or implementation and therefore does not require extra computational load when running the KF.

The autocovariance matrix (ACM) of size N (maximum epoch duration of the time-correlated process in the filter) of the bounding non-stationary GMP model is:

$$\hat{\mathbf{R}}(\mathrm{N}) = \begin{bmatrix} r_{00} & r_{01} & \cdots & r_{0\mathrm{N}} \\ r_{01} & r_{11} & \cdots & r_{1\mathrm{N}} \\ \vdots & \vdots & \ddots & \vdots \\ r_{0\mathrm{N}} & r_{1\mathrm{N}} & \cdots & r_{\mathrm{NN}} \end{bmatrix}, \tag{5.61}$$

The actual, unknown stationary GMP ACM is expressed as:

$$\mathbf{R}(\mathrm{N}) = \begin{bmatrix} \sigma^2 & \alpha\sigma^2 & \cdots & \alpha^{\mathrm{N}}\sigma^2 \\ \alpha\sigma^2 & \sigma^2 & \cdots & \alpha^{\mathrm{N}-1}\sigma^2 \\ \vdots & \vdots & \ddots & \vdots \\ \alpha^{\mathrm{N}}\sigma^2 & \alpha^{\mathrm{N}-1}\sigma^2 & \cdots & \sigma^2 \end{bmatrix}. \tag{5.62}$$

Equation (5.62) is obtained by setting $\sigma_0^2 = \sigma^2$ and by replacing $\hat{\sigma}^2 = \sigma^2$ and $\hat{\alpha}$ with $\alpha = e^{\frac{-\Delta_t}{\tau}}$ in Equation (5.60), and substituting the result into Equation (5.61).

As shown in Section 5.1.1, error estimation bounding conditions can be established at the noises covariance level, therefore it must be ensured that:

$$\Delta\mathbf{R} = \hat{\mathbf{R}} - \mathbf{R} = \hat{\mathbf{R}} - \sigma^2\bar{\mathbf{R}} \geq 0, \tag{5.63}$$

where σ^2 has been extracted from Equation (5.62) as common factor and $\bar{\mathbf{R}}$ is the autocorrelation matrix. The matrix $\Delta\mathbf{R}$ in Equation (5.63) must be positive semidefinite for all values of $\sigma^2 \in [\sigma^2_{\min}, \sigma^2_{\max}]$ and $\tau \in [\tau_{\min}, \tau_{\max}]$. If matrix $\Delta\mathbf{R}$ is positive semidefinite when choosing $\sigma^2 = \sigma^2_{\max}$, it is ensured that it will also be positive semidefinite for all the possible values of σ^2.

Using $\sigma^2 = \sigma^2_{\max}$ and the notation $\hat{\sigma}^2 = \sigma^2_{\max} k$, where k can be extracted from Equation (4.41) or Equation (5.25) and $\sigma^2_0 = \sigma^2_{\max} k_0$, Equation (5.63) can be expressed over a time span N as:

$$\Delta\mathbf{R}(\mathrm{N}, k_0) = \sigma^2_{\max} \begin{bmatrix} k_0 - 1 & \cdots & \hat{\alpha}^{n-1} k_0 - \alpha^{\mathrm{N}-1} \\ \vdots & \ddots & \vdots \\ \cdots & \cdots & \hat{\alpha}^{2\mathrm{N}} k_0 + k\left(1 - \hat{\alpha}^{2\mathrm{N}}\right) - 1 \end{bmatrix}. \tag{5.64}$$

The minimum acceptable value of k_0 is the smallest one guaranteeing that $\Delta\mathbf{R}$ is positive semidefinite [73]. In order to find k_0, we use the fact that the eigenvalues of a real symmetric matrix are real, and that the matrix is positive semidefinite if and only if its minimum eigenvalue is nonnegative. For the symmetric matrix $\Delta\mathbf{R}(\mathrm{N})$ with minimum eigenvalue $\lambda_{\min}$, we must ensure that $\lambda_{\min}(\mathrm{N}) \geq 0, \forall \mathrm{N} \in \mathbb{Z}_{\geq 0}$. The numerical search for σ^2_0 can be expressed as:

$$\sigma^2_0 = \sigma^2_{\max} \cdot \arg\min_{k_x} \{\lambda_{\min}(\Delta\mathbf{R}(\mathrm{N}, k_x)) \geq 0\}. \tag{5.65}$$

A good initialization point for the numerical search is provided in Appendix A.5. It ensures that the first 2x2 leading principal sub-matrix of $\Delta\mathbf{R}$ is positive semidefinite.

5.3 Evaluation in Kalman Filter Implementation

In this section the behaviour of the conservative and tight bounds in Chapter 4 and Chapter 5 are analysed for a simple discrete-time example. The example in Section 1.2 is used as a simple system for comparing the selection of different bounds. Figure (5.4) shows first the difference between the standard deviation of the position estimated using a KF with different choice of GMP model parameters and the standard deviation of the error of the KF estimation. For computation of the true estimated error standard deviation of a discrete-time KF, the reader is recall to consult the Appendix A.1. Figure (5.4) displays the stationary and non-stationary GMP models conservative and tight bounds derived via frequency domain and sensitivity analysis. Positive values of the curves mean that the GMP models all produce upper bounds on the positioning variance. If the simulation time were long enough, we would see the positioning uncertainty based on the non-stationary GMP models converge towards their corresponding stationary GMP models.

Let us turn the attention to the transient period. It can be seen that over the first 300s of

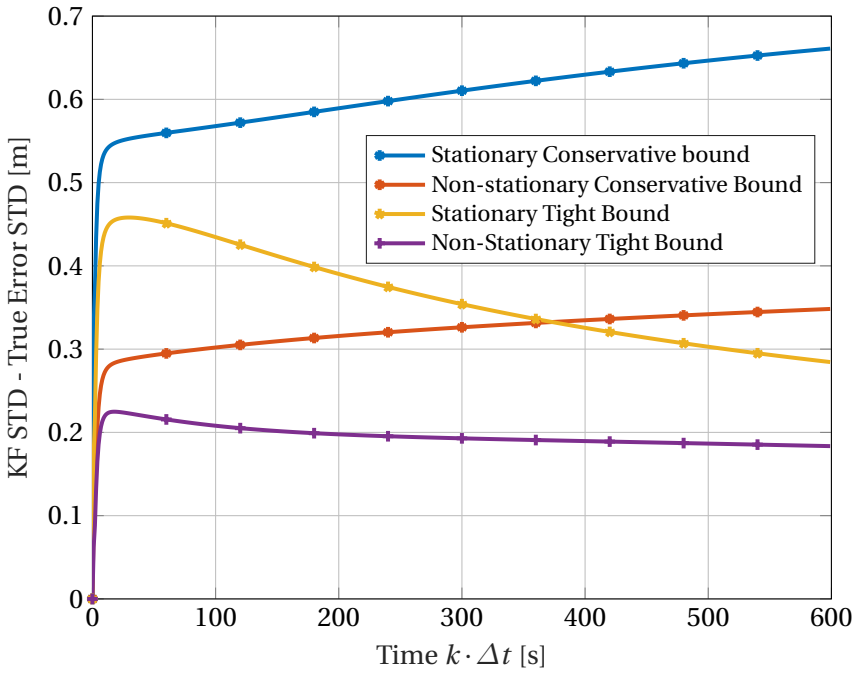

Figure 5.4: KF estimated std vs true error std (Position) ($\tau_{max} = 100$, $\tau_{min} = 10$, $\tau_{true} = 50$ and $\Delta t = 1$s).

simulation time, the non-stationary GMP model using sensitivity analysis provides a tighter positioning deviation bound than the model in Section 4.2.1. But, as filtering approaches steady-state, the proposed stationary model in Section 4.2.1 provides a tighter bound on the underlying error. The non-stationary GMP model in Section 5.2.3 achieves the tightest positioning error bound under the given conditions.

In addition, Figure (5.5), shows the KF positioning standard deviations for the different GMP models , and the KF standard deviation obtained if we knew the true value of correlation time constant. This figure illustrates the inflation in standard deviation that we endure for lack of knowledge of the actual error correlation time constant, and the tightness of the positioning variance bounds obtained using the proposed GMP models.

5.4 Conclusions

In this Chapter, different mechanism for selecting parameters of stationary GMP models were derived that guarantee upper bounds on linear estimation error variance in the presence of uncertain models employing Gauss-Markov structure. The stationary models are obtained via a modified sensitivity analysis of KF and with frequency domain analysis in both the continuous-time and discrete-time domains. Although the selection of model parameters de-

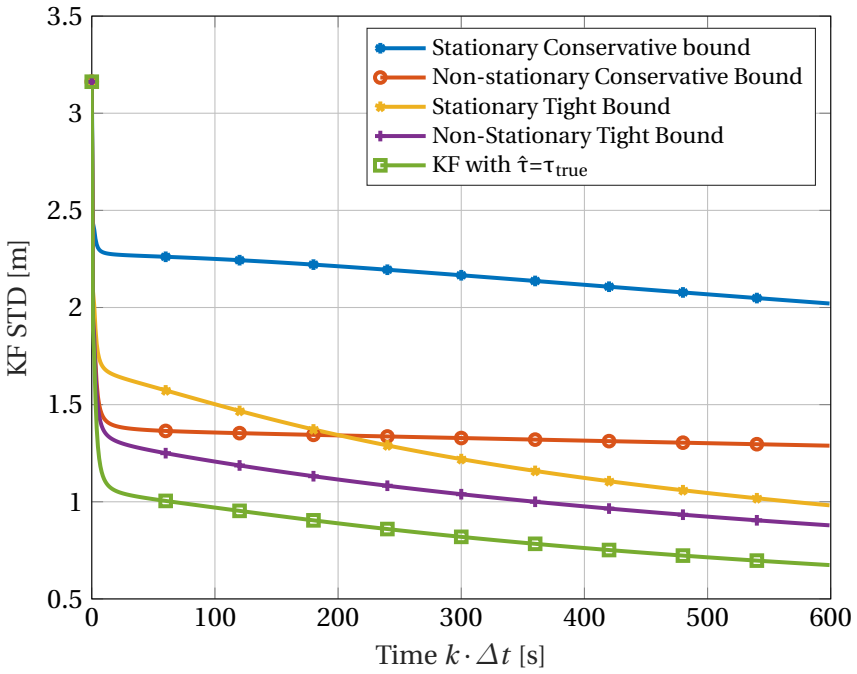

Figure 5.5: KF estimated standard deviation (Position) ($\tau_{max} = 100$, $\tau_{min} = 10$, $\tau_{true} = 50$ and $\Delta t = 1$s).

vised in the continuous-time are less complex, those based on discrete case have a wider field of application. The stationary models were improved upon using non-stationary GMP which provides a tighter variance and error bound during the transient period. It was shown that the parameter selection for such GMP models can easily be implemented in linear dynamic estimators such as Kalman filters.

Summary of Main Results

Under the presence of Gauss-Markov error processes with uncertain but bounded time-correlation constant within an interval $\tau \in [\tau_{\min}, \tau_{\max}]$ and variance $\sigma^2 \in [\sigma^2_{\min}, \sigma^2_{\max}]$, a tight upper bound on the estimated variance-covariance of any linear estimator like a Kalman filter can be obtained when choosing the individual stationary GMP models with parameters in Table 5.1:

Table 5.1: Summary Gauss-Markov Process Bounding Models Parameters

	Continuous-time Domain* (for $\tau_{\max} \geq \tau_{\min} > 0$)	Discrete-time Domain (for $\tau_{\max} \geq \tau_{\min} \geq 0$)
Stationary Model	$\hat{\sigma}^2_c = \sqrt{\frac{\tau_{\max}}{\tau_{\min}}}\sigma^2_{\max}$, $\hat{\tau}_c = \sqrt{\tau_{\min}\tau_{\max}}$.	$\hat{\sigma}^2_d = \sigma^2_{\max}\sqrt{\frac{(1-\alpha_{\min})(1+\alpha_{\max})}{(1+\alpha_{\min})(1-\alpha_{\max})}}$, $\hat{\tau}_d = -\Delta t \left[\ln\left(\frac{1-\sqrt{\Gamma}}{1+\sqrt{\Gamma}}\right)\right]^{-1}$, where $\alpha_{\min} = e^{-\frac{\Delta_t}{\tau_{\min}}}$, $\alpha_{\max} = e^{\frac{\Delta_t}{\tau_{\max}}}$, $\Gamma = \frac{(1-\alpha_{\min})(1-\alpha_{\max})}{(1+\alpha_{\min})(1+\alpha_{\max})}$.
Non-Stationary Model (Initial variance)	$\hat{\sigma}^2_{c,0} = \sigma^2_{\max}\frac{2}{1+\sqrt{\frac{\tau_{\min}}{\tau_{\max}}}}$.	$\hat{\sigma}_{d,0} = \sigma^2_{\max}\frac{1}{1-\frac{2(\hat{\alpha}-\alpha_{\max})^2}{(1-\hat{\alpha}^2)(1-\alpha^2_{\max})(k_d-1)}}$, where $k_d = \sqrt{\frac{(1-\alpha_{\min})(1+\alpha_{\max})}{(1+\alpha_{\min})(1-\alpha_{\max})}}$.

*Continuous-time model parameters can also be used in discrete-time models

Part III

Application to GNSS/INS Integrity Monitoring

6 Overbounding GNSS/INS Integration for Aviation Users

Chapter 5 provided new selection of Gauss-Markov Error Models that guarantee covariance bounding condition on KF integration when the error processes contain uncertain parameters. This chapter shows how the new GMP models can be applied for safe GNSS/INS integration in terms of integrity as discussed in Chapter 3. In particular, uncertain GNSS error models for the different error sources as reported in literature are adapted to a GNSS/INS filter design. Finally a complete algorithm is proposed based on a bank of KFs and a multiple hypothesis solution separation architecture that determines protection levels and ensure integrity over larger span of possible situations.

6.1 Error Model Implementation

This section describes the error models for the GNSS and IMU measurements. Particularly relevant in this work is the consideration of uncertain parameters for the time correlated errors in GNSS, which are assumed to reside within a known range of values.

6.1.1 GNSS

The linearized ionospheric-free code and carrier measurements can be expressed as:

$$\rho_{\mathrm{IF},k}^{i,j} - \tilde{\rho}_k^{i,j}(\mathbf{x}_{0,k}) = \mathbf{u}_k^{i,j^{\mathrm{T}}} \Delta\mathbf{x}_k + b_k^j + \Delta \mathrm{S}_k^{i,j} + dT_k^{i,j} + mp_{\rho,k}^{i,j} + \epsilon_{\rho,k}^{i,j}, \tag{6.1}$$

$$\phi_{\mathrm{IF},k}^{i,j} - \tilde{\phi}_k^{i,j}(\mathbf{x}_{0,k}) = \mathbf{u}_k^{i,j^{\mathrm{T}}} \Delta\mathbf{x}_k + b_k^j + \Delta \mathrm{S}_k^{i,j} + dT_k^{i,j} + N_\phi^{i,j} + mp_{\phi,k}^{i,j} + \epsilon_{\phi,k}^{i,j}, \tag{6.2}$$

where $\rho_{\mathrm{IF},k}^{i,j}$ is the code measurement of satellite i of constellation j at time epoch k. $\mathbf{u}_k^{i,j^{\mathrm{T}}}$ is a unit line of sight vector user to satellite, $\Delta\mathbf{x}_k$ is the user position with respect to the linearization point. The receiver clock offset with respect to constellation j is b_k^j. $\Delta \mathrm{S}_k^{i,j}$ is the residual satellite clock and ephemeris error after correction based on broadcast ephemeris, $dT_k^{i,j}$ is

the tropospheric error, $mp^{i,j}_{\rho,k}$ and $mp^{i,j}_{\phi,k}$ the multipath error in code and carrier respectively, $\epsilon^{i,j}_k$ the receiver noise and $N^{i,j}_\phi$ is the float ionospheric-free carrier-phase ambiguity term.

Satellite Clock and Orbit Errors

According to [85], residual satellite clock and ephemeris error for a satellite i can be expressed as Gauss-Markov processes with uncertain time constant in a given range:

$$\Delta S^{i,\mathrm{GPS}} \sim \mathcal{GM}(\sigma^2_{\mathrm{URA}}, \tau \in [4,50] \text{ hours}), \tag{6.3}$$

$$\Delta S^{i,\mathrm{GAL}} \sim \mathcal{GM}(\sigma^2_{\mathrm{SISA}}, \tau \in [2,38] \text{ hours}). \tag{6.4}$$

The user range accuracy (URA) is nominally chosen to be $\sigma_{\mathrm{URA}} = \sigma_{\mathrm{SISA}} = 1\mathrm{m}$ for both GPS and Galileo [21].

Tropospheric Errors

The largest part of the tropospheric error caused by the dry component can be removed by applying standard models [18]. The remaining wet component of the troposphere is more unpredictable and it is typically modeled as:

$$\Delta T^{i,j}_k = m_{\mathrm{tropo}}(\theta^{i,j}) \cdot \eta_{\mathrm{tropo},k}, \tag{6.5}$$

where $m_{\mathrm{tropo}}(\theta^{i,j})$ is a mapping function that depends on the satellite elevation $\theta^{i,j}$ [18]:

$$m_{\mathrm{tropo}}(\theta^{i,j}) = \frac{1.001}{\sqrt{0.002001 + \sin(\theta^{i,j})^2}}. \tag{6.6}$$

The uncertain component $\eta_{\mathrm{tropo},k}$ at the zenit is specified in [18] to be overbounded by a zero mean Gaussian distribution with variance $\sigma^2_{\mathrm{tropo}} = (0.12)^2\mathrm{m}^2$. The random component $\eta_{\mathrm{tropo},k}$ is a first-order Gauss-Markov process with the range of parameters specified in Table 6.1.

Multipath and antenna group delay

For 100 seconds carrier-smoothed code, the following expression is given for the multipath error standard deviation [21]:

$$\sigma^{i,j}_{mp,\rho,\mathrm{sm}} = \sqrt{\frac{(f^2_{\mathrm{L1}} - f^2_{\mathrm{L5}})^2}{f^4_{\mathrm{L1}} + f^4_{\mathrm{L5}}}} \left(0.13 + 0.53 e^{-\theta^{i,j}_{\mathrm{deg}}/10}\right), \tag{6.7}$$

where f_{L1} and f_{L5} are the GNSS carrier frequencies for L1 and L5 signals respectively and $\theta^{i,j}_{deg}$ is the satellite elevation in degrees from the user standpoint.

Considering unsmoothed measurements in the filter has several advantages. First it avoids the artificial correlation that the smoothing would cause between the measurements in the filter. Second, the need for the smoothing-filter initialization time is removed. It is found in [102], [103], that the unsmoothed code and carrier phase standard deviation due to multipath can be obtained with the following scaling of the smoothed observations:

$$\begin{aligned} \sigma_{mp,\rho} &= 1.5 \cdot \sigma_{mp,\rho,sm}, \\ \sigma_{mp,\phi} &= 0.015 \cdot \sigma_{mp,\rho,sm}. \end{aligned} \tag{6.8}$$

The total multipath for code and carrier is in this case expressed as:

$$mp^{i,j}_{\rho,k} = \sigma_{mp,\rho}(\theta^{i,j}_k) \cdot \eta^{i,j}_{mp_\rho,k}, \tag{6.9}$$

$$mp^{i,j}_{\phi,k} = \sigma_{mp,\phi}(\theta^{i,j}_k) \cdot \eta^{i,j}_{mp_\phi,k}. \tag{6.10}$$

The first term will follow Equation (6.8) and Equation (6.7) and it is used as a mapping or scaled parameter. The stochastic process $\eta^{i,j}_{mp_\rho,k}$ and $\eta^{i,j}_{mp_\phi,k}$ are modeled as first-order Gauss-Markov processes with unit variance and time-correlations in the ranges specified in Table 6.1.

Receiver Noise

The receiver noise component in the code and carrier measurement is modeled as a zero mean white Gaussian noise. Receiver code and carrier phase standard deviations can be expressed as [103]:

$$\begin{aligned} \sigma^{i,j}_{\epsilon_\rho} &= 19.6 \cdot \sigma^{i.j}_{\epsilon_\rho,sm}, \\ \sigma^{i,j}_{\epsilon_\phi} &= 0.196 \cdot \sigma^{i.j}_{\epsilon_\rho,sm}, \end{aligned} \tag{6.11}$$

where $\sigma^{i.j}_{\epsilon_\rho,sm}$ is the iono-free scaled carrier smoothed code noise standard deviation which is dependent on elevation [21]:

$$\sigma^{i.j}_{\epsilon_\rho,sm} = \sqrt{\frac{(f^2_{L1} - f^2_{L5})^2}{f^4_{L1} + f^4_{L5}}} \left(0.15 + 0.43 e^{-\theta^{i,j}_{deg}/6.9}\right). \tag{6.12}$$

where the elevation dependent model for class A receivers from [104] has been used.

Table 6.1: GNSS Error Model Parameters.

		Error Parameters		
Error source	Mapping	Variance	τ_{min}	τ_{max}
Clock and Eph. (GPS)	-	$\sigma^2_{URA}, \sigma^2_{URE}$	4 h.	50 h.
Clock and Eph. (Gal)	-	$\sigma^2_{SISA}, \sigma^2_{SISRE}$	2 h.	38 h.
Tropospheric	Eq.(6.6)	$(0.12\ \text{m})^2$	900 s	2700 s
Raw Code Multipath	Eqs.(6.7,6.8)	1m^2	10 s	900 s
Raw Carrier Multipath	Eqs.(6.7,6.8)	1m^2	10 s	900 s
Receiver Code Noise	-	Eqs.(6.11,6.12)	-	-
Receiver Carrier Noise	-	Eqs.(6.11,6.12)	-	-

Table 6.2: GNSS GMP Bound Error Model

	GMP Bound Parameters		
Error source	$\hat{\sigma}^2$	$\hat{\tau}$	σ^2_0
Clock and Eph. (GPS)	$\{\sigma^2_{URA}, \sigma^2_{URE}\} \cdot 3.54$	14.14 h.	$\{\sigma^2_{URA}, \sigma^2_{URE}\} \cdot 1.56$
Clock and Eph. (Gal)	$\{\sigma^2_{SISA}, \sigma^2_{SISRE}\} \cdot 4.36$	8.72 h.	$\{\sigma^2_{SISA}, \sigma^2_{SISRE}\} \cdot 1.63$
Tropospheric	0.025	1558.85 s.	0.018
Raw Code Multipath	9.49	94.87 s.	1.81
Raw Carrier Multipath	9.49	94.87 s.	1.81

Receiver Clock

GNSS receiver clocks are typically quartz oscillators; their offset with respect to GPS time is often treated as a parameter to be estimated. In this work, it is conservatively assumed that at any particular time, we do not have any prior knowledge of the clock bias from previous time instants. This is modeled as an KF state parameter following a random walk with infinite (very high) variance.

6.1.2 Inertial Measurement Unit (IMU)

The inertial measurements coming from gyroscopes and accelerometers are typically modeled as a combination of error sources and processes. First, deterministic errors include misalignment of the sensor axis, scaling factors and constant biases. In this work, these errors are assumed to be estimated and compensated for using an offline calibration procedure by the manufacturer. Second, stochastic errors that cannot be apriori compensated for need to be considered in the estimation algorithm. A widely-used approach for navigation and high tactical grade IMUs is to model stochastic errors of the IMU as the sum of a random constant turn-on bias, a time-correlated process and a white-Gaussian noise. In this case, turn rate and

Table 6.3: IMU Accelerometer Error Parameters.

Grade	**Noise** [μg/$\sqrt{\text{Hz}}$]	**Bias Noise** [μg]	τ [s]
Navigation	15	20	3000
Tactical	50	160	3000

Table 6.4: IMU Gyroscope Error Parameters.

Grade	**Noise** [°/h/$\sqrt{\text{Hz}}$]	**Bias Noise** [° h^{-1}]	τ [s]
Navigation	0.01	0.005	12000
Tactical	2	0.5	10000

specific force measurements can be expressed as:

$$\tilde{\mathbf{w}}^b = \mathbf{w}^b + \mathbf{b}_{w,0} + \mathbf{b}_w + \boldsymbol{\eta}_w, \tag{6.13}$$

$$\tilde{\mathbf{f}}^b = \mathbf{f}^b + \mathbf{b}_{f,0} + \mathbf{b}_f + \boldsymbol{\eta}_f, \tag{6.14}$$

where $\tilde{\mathbf{w}}^b$ and $\tilde{\mathbf{f}}^b$ are the 3-axis measured turn rates and specific forces in a body frame b, respectively; similar, $\mathbf{w}^b$ and $\mathbf{f}^b$ are their true values, $\mathbf{b}_{\star,0}$ is the turn-on random constant bias with $\star$ referring either to the angular rates $\mathbf{w}$ or to the specific forces $\mathbf{f}$. Last, $\mathbf{b}_\star$ is the time-correlated bias and $\boldsymbol{\eta}_\star$ are the white Gaussian noise vectors of the associated measurements.

The turn-on biases are initially roughly estimated by initial alignment process and further improved during navigation process [28]. For low cost sensors in particular, final estimation of these random constant biases is often performed while in operation and thanks to the dynamics of the vehicle.

The most widely used model for the time-correlated bias of IMU measurements is based on a GM approximation, in part because it can easily by incorporated in a Kalman filter by state augmentation. This model is also adopted here. Typical GM model parameter values for two sensor grades are listed in Table 6.3 and Table 6.4 for the GM bias over time (including a time constant and driving noise specifications) and for the measurement white noise.

Contrary to GNSS system, each aircraft will contain its own particular IMU system. Therefore only general claims about grades or categories of sensors are here considered. The specific IMU error parameters are assumed to be known and relatively stable.

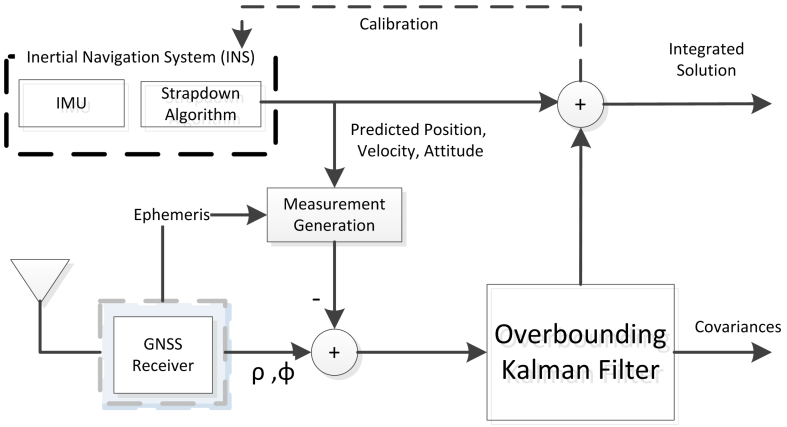

Figure 6.1: GNSS/INS Kalman filter Architecture.

6.2 GNSS/INS Kalman Filter Design

This research considers a tightly coupled integration between GNSS and Inertial Navigation System (INS) with an error-state Kalman Filter. A general architecture of the system design is depicted in Figure 6.1 [105]. Note that the inertial navigation system is run outside the KF and in the architecture scheme it is *calibrated* with parameters estimated using the KF.

6.2.1 State Selection

Kalman filter state parameters include position, velocity and attitude errors in a local navigation frame. In order to account for the time correlated errors present in IMU measurements we include the augmented states $\mathbf{b}_f$ and $\mathbf{b}_w$. The total number of error states related to the INS system is therefore $N_{INS} = 15$:

$$\mathbf{x}_{\text{INS}} = \begin{pmatrix} \delta\boldsymbol{\psi}^{\text{T}} & \delta\mathbf{v}^{\text{T}} & \delta\mathbf{p}^{\text{T}} & \mathbf{b}_f^{\text{T}} & \mathbf{b}_w^{\text{T}} \end{pmatrix}^{\text{T}} \tag{6.15}$$

where $\delta\boldsymbol{\psi}$, $\delta\mathbf{v}$ and $\delta\mathbf{p}$ are the 3D errors in attitude, velocity and position of the INS, respectively. The filter states specific to GNSS first include the receiver clock biases with respect to each constellation in use. In order to account for the time correlated errors, additional augmented states are added to the state vector to capture the satellite clock and ephemeris, tropospheric and multipath error of each satellite. Finally, we add the integer ambiguities to each of the satellites in view. The GNSS-specific state vector component is therefore:

$$\mathbf{x}_{\text{GNSS}} = \begin{pmatrix} \mathbf{b}_{\text{clk}}{}^{\text{T}} & \Delta\mathbf{S}^{\text{T}} & \mathbf{m}_{\text{tropo}}{}^{\text{T}} & \mathbf{mp}_{\rho}^{\text{T}} & \mathbf{mp}_{\phi}^{\text{T}} & \mathbf{N}_{\phi}{}^{\text{T}} \end{pmatrix}^{\text{T}} \tag{6.16}$$

where $\mathbf{b}_{\text{clk}}$ are the user clock biases for each GNSS constellation, $\Delta\mathbf{S}$ the satellite ephemeris and clock error, $\mathbf{m}_{\text{tropo}}$ the tropospheric error at zenith, $\mathbf{mp}_{\rho}$ and $\mathbf{mp}_{\phi}$ the code and carrier

multipath respectively and $\mathbf{N}_\Phi$ the float iono-free integer ambiguities. The KF state vector therefore contains $N_{KF} = 15 + N_j + 5N_i$ parameters, where N_j is the number of constellations and N_i the number of satellites in view:

$$\mathbf{x}_{KF} = \begin{pmatrix} \mathbf{x}_{INS}^T & \mathbf{x}_{GNSS}^T \end{pmatrix}^T. \tag{6.17}$$

6.2.2 KF Prediction

The KF time-update or prediction step propagates the mean and covariance of the state estimates as follows:

$$\hat{\mathbf{x}}_{k|k-1} = \hat{\mathbf{\Phi}}_k \hat{\mathbf{x}}_{k-1|k-1}, \tag{6.18}$$

$$\hat{\mathbf{P}}_{k|k-1} = \hat{\mathbf{\Phi}}_k \hat{\mathbf{P}}_{k-1|k-1} \hat{\mathbf{\Phi}}_k^T + \mathbf{G}_k \hat{\mathbf{Q}}_k \mathbf{G}_k^T, \tag{6.19}$$

where $\hat{\mathbf{x}}_{k|k-1}$ and $\hat{\mathbf{P}}_{k|k-1}$ are the predicted states and covariance respectively, $\hat{\mathbf{\Phi}}_k$ is the time propagation matrix, $\hat{\mathbf{Q}}_k$ is the covariance of the process noise and $\mathbf{G}_k$ maps the process noise vector to the relevant states. The $\hat{}$ notation on $\hat{\mathbf{\Phi}}_k$ and $\hat{\mathbf{Q}}_k$ indicates that a filter design choice is made: we want to set $\hat{\mathbf{\Phi}}_k$ and $\hat{\mathbf{Q}}_k$ guaranteeing that the computed estimate error covariance $\hat{\mathbf{P}}_{k|k-1}$ overbounds the actual estimation uncertainty. The discrete propagation matrix $\hat{\mathbf{\Phi}}_k$ for the GNSS/INS design can be expressed as:

$$\hat{\mathbf{\Phi}}_k = \begin{bmatrix} \mathbf{\Phi}_{k,INS} & \mathbf{0} \\ \mathbf{0} & \hat{\mathbf{\Phi}}_{k,GNSS} \end{bmatrix}, \tag{6.20}$$

where

$$\mathbf{\Phi}_{k,INS} = e^{\mathbf{F}_{k,INS}\Delta t} \approx \mathbf{I} + \mathbf{F}_{k,INS}\Delta t. \tag{6.21}$$

The Jacobian matrix $\mathbf{F}_{k,INS}$ can be obtained by differentiating the strapdown inertial differential Equations 2.19 at time k to which the bias $\mathbf{b}_f$ and $\mathbf{b}_w$ terms are added. This matrix is well known and can be found in Appendix C.2. It is worth noticing that $\mathbf{\Phi}_{INS}$ and $\mathbf{F}_{INS}$ do not have the $\hat{}$ notation because, in this work, the IMU error process parameters are assumed to be determined with enough accuracy. The propagation design matrix $\hat{\mathbf{\Phi}}_{k,GNSS}$ is a diagonal matrix expressed as:

$$\hat{\mathbf{\Phi}}_{k,\text{GNSS}} = \begin{bmatrix} \mathbf{I}^{\text{N}_j \times \text{N}_j} & & & & & \\ & e^{-\frac{\Delta_t}{\hat{\tau}_{\text{S}}}} \mathbf{I}^{\text{N}_i \times \text{N}_i} & & & & \\ & & e^{-\frac{\Delta_t}{\hat{\tau}_{\text{tropo}}}} \mathbf{I}^{\text{N}_i \times \text{N}_i} & & & \\ & & & e^{-\frac{\Delta_t}{\hat{\tau}_{mp,\rho}}} \mathbf{I}^{\text{N}_i \times \text{N}_i} & & \\ & & & & e^{-\frac{\Delta_t}{\hat{\tau}_{mp,\phi}}} \mathbf{I}^{\text{N}_i \times \text{N}_i} & \\ & & & & & \mathbf{I}^{\text{N}_i \times \text{N}_i} \end{bmatrix}. \tag{6.22}$$

In Equation (6.19), the $\hat{\mathbf{Q}}_k$ matrix can also be split into contributions from the IMU and GNSS error processes using the following definitions:

$$\hat{\mathbf{Q}}_k = \begin{bmatrix} \mathbf{Q}_{\text{IMU}} & \mathbf{0} \\ \mathbf{0} & \hat{\mathbf{Q}}_{k,\text{GNSS}} \end{bmatrix}. \tag{6.23}$$

The covariance $\mathbf{Q}_{\text{IMU}}$ contains the IMU noise and GM variances which are not changing at different epochs.

The matrix $\hat{\mathbf{Q}}_{k,\text{GNSS}}$ is a diagonal matrix expressed as:

$$\hat{\mathbf{Q}}_{k,\text{GNSS}} = \text{diag}\begin{pmatrix} \sigma^2_{\text{clk}} \Delta t \mathbf{1}^{\text{N}_j \times 1} \\ \hat{\sigma}^2_{\Delta_{\text{S}}} \left(1 - e^{-\frac{2\Delta_t}{\hat{\tau}_{\text{S}}}}\right) \mathbf{1}^{\text{N}_i \times 1} \\ \hat{\sigma}^2_{\text{tropo}} \left(1 - e^{-\frac{2\Delta_t}{\hat{\tau}_{\text{tropo}}}}\right) \mathbf{1}^{\text{N}_i \times 1} \\ \hat{\sigma}^2_{mp,\rho} \left(1 - e^{-\frac{2\Delta_t}{\hat{\tau}_{mp,\rho}}}\right) \mathbf{1}^{\text{N}_i \times 1} \\ \hat{\sigma}^2_{mp,\phi} \left(1 - e^{-\frac{2\Delta_t}{\hat{\tau}_{mp,\phi}}}\right) \mathbf{1}^{\text{N}_i \times 1} \\ \mathbf{0}^{\text{N}_i \times 1} \end{pmatrix}. \tag{6.24}$$

The notation $\mathbf{1}^{a \times b}$ and $\mathbf{0}^{a \times b}$ indicates a matrix (or vector) of size $a \times b$ filled with ones or zeros respectively. The values of the $\hat{\sigma}^2$ and $\hat{\tau}$ parameters are computed using Equation (4.41) and parameter range limits in Table 6.1 to ensure that the KF estimation error covariance is

overbounded. Finally, matrix $\mathbf{G}_k$ can be written as:

$$\mathbf{G}_k = \begin{bmatrix} \mathbf{G}_{k,\text{IMU}} & \mathbf{0}^{\text{N}_{\text{INS}} \times \text{N}_{\text{GNSS}}} \\ \mathbf{0}^{\text{N}_{\text{GNSS}} \times \text{N}_{\text{INS}}} & \mathbf{I}^{\text{N}_{\text{GNSS}} \times \text{N}_{\text{GNSS}}} \end{bmatrix}, \tag{6.25}$$

where $\text{N}_{\text{INS}} = 15$ and $\text{N}_{\text{GNSS}} = \text{N}_j + 5\text{N}_i$. Matrix $\mathbf{G}_{k,\text{IMU}}$ is given in Appendix in [106].

6.2.3 KF Update

The Kalman filter measurement update is performed using the following equations:

$$\hat{\mathbf{x}}_{k|k} = \hat{\mathbf{x}}_{k|k-1} + \hat{\mathbf{K}}_k \left(\mathbf{z}_k - \mathbf{H}_k \hat{\mathbf{x}}_{k|k-1} \right), \tag{6.26}$$

$$\hat{\mathbf{P}}_{k|k} = \left(\mathbf{I} - \hat{\mathbf{K}}_k \mathbf{H}_k \right) \hat{\mathbf{P}}_{k|k-1}, \tag{6.27}$$

where $\hat{\mathbf{K}}$ is the Kalman filter gain obtained using:

$$\hat{\mathbf{K}}_k = \hat{\mathbf{P}}_{k|k-1} \mathbf{H}_k^{\text{T}} \left(\mathbf{H}_k \hat{\mathbf{P}}_{k|k-1} \mathbf{H}_k^{\text{T}} + \mathbf{R}_k \right)^{-1}. \tag{6.28}$$

The linearized KF measurement vector $\mathbf{z}$ is made of the differences between the ionospheric-free code and carrier phase measurements and their predicted values computed using the INS current position projected via the non-linear relations $h(x)$:

$$\mathbf{z}_k = \begin{bmatrix} \rho^1_{\text{IF},k} - \rho^1_{k,\text{INS}} \\ \vdots \\ \rho^{\text{N}_i}_{\text{IF},k} - \rho^{\text{N}_i}_{k,\text{INS}} \\ \phi^1_{\text{IF},k} - \phi^1_{k,\text{INS}} \\ \vdots \\ \phi^{\text{N}_i}_{\text{IF},k} - \phi^{\text{N}_i}_{k,\text{INS}} \end{bmatrix}. \tag{6.29}$$

The measurement matrix $\mathbf{H}$ is a linearized version of $h(x)$ that projects the states into measurement space and is expressed as:

$$\mathbf{H}_k = \begin{bmatrix} \mathbf{0}^{6\times N_i} & \mathbf{0}^{6\times N_i} \\ \mathbf{U}_k^T & \mathbf{U}_k^T \\ \mathbf{0}^{6\times N_i} & \mathbf{0}^{6\times N_i} \\ \mathbf{1}_{\{s^i\in c^j\}}^{N_j\times N_i} & \mathbf{1}_{\{s^i\in c^j\}}^{N_j\times N_i} \\ \mathbf{I}^{N_i\times N_i} & \mathbf{I}^{N_i\times N_i} \\ \mathbf{M}_{\text{tropo}} & \mathbf{M}_{\text{tropo}} \\ \mathbf{M}_{mp,\rho} & \mathbf{0}^{N_i\times N_i} \\ \mathbf{0}^{N_i\times N_i} & \mathbf{M}_{mp,\phi} \\ \mathbf{0}^{N_i\times N_i} & \mathbf{I}^{N_i\times N_i} \end{bmatrix}^T, \tag{6.30}$$

where $\mathbf{U}_k \in \mathbb{R}^{N_i\times 3}$ contains the line-of-sight vectors related to each of the satellites in view. The diagonal matrix $\mathbf{M}_{\text{tropo}} \in \mathbb{R}^{N_i\times N_i}$ contains the tropospheric mapping function for each of the satellites depending on their elevation as in Equation (6.6). And the diagonal matrix $\mathbf{M}_{mp,\rho}, \mathbf{M}_{mp,\phi} \in \mathbb{R}^{N_i\times N_i}$ contains the scaling of the multipath time-correlated errors according to their elevation as in Equation (6.8) for the code and carrier phase measurement respectively. Each element (j,i) of the matrix $\mathbf{1}_{\{s^i\in c^j\}}^{N_j\times N_i}$ is one if the satellite s^i belongs to constellation c_j and zero otherwise. Finally, $\mathbf{R}_k$ is a diagonal matrix containing the code and carrier receiver noise variances (Equation (6.11)):

$$\mathbf{R}_k = \begin{bmatrix} \sigma_{\epsilon_\rho}^2 \mathbf{I}^{N_i\times N_i} & \mathbf{0} \\ \mathbf{0} & \sigma_{\epsilon_\phi}^2 \mathbf{I}^{N_i\times N_i} \end{bmatrix}. \tag{6.31}$$

Note that in the case of loss of satellites tracking, the size of state vector and covariance matrix must be reduced accordingly. Similarly, new states must be created and initialized if new satellites are available during the filter runtime. The change of satellites in view also affects the size of $\hat{\mathbf{\Phi}}_{k,\text{GNSS}}$, $\hat{\mathbf{Q}}_{k,\text{GNSS}}$, $\mathbf{G}_k$, $\mathbf{H}_k$ and $\mathbf{R}_k$.

6.3 GNSS/INS Multiple Hypothesis Solution Separation

This chapter has provided so far with the necessary design elements to guarantee a safe GNSS/INS estimation under the presence of uncertain *nominal* GNSS errors. In fault-free conditions (hypothesis H0), the estimated KF covariance $\mathbf{\Sigma} = \hat{\mathbf{P}}$ is sufficient to determine the

associated integrity risk in a dimension l for a given alert limit as:

$$\mathrm{IR}_{l,\mathrm{H0}} = \mathrm{Q}\left(\frac{\mathrm{AL}_l}{\sqrt{\boldsymbol{\varepsilon}_l^{\mathrm{T}}\hat{\mathbf{P}}\boldsymbol{\varepsilon}_l}}\right), \tag{6.32}$$

where Q is the complementary error function and $\boldsymbol{\varepsilon}_l$ is a vector with one in the selected state l and zero otherwise. In the presence of faults, estimators are accompanied by some type of monitor or fault detection that protects the computed solution. Two main fault detection algorithms are normally used in the context of Kalman filtering. One of them is based on the innovation sequence and would typically compute a χ^2 test statistic, either in a snapshot or accumulated over time. The other type of fault detection strategy is based on solution separation. It has been shown that solution separation test statistics are more powerful than residual-based tests [102] since they are tailored to specific fault modes. Moreover, innovation-based tests tend to lose detectability if employed over too long periods [36]. In this work, the Multiple Hypothesis Solution Separation (MHSS) algorithm is adopted by considering a bank of Kalman filters, each of them running a specific subset of measurements. This strategy is not new and it has been considered over many years for GNSS/INS integration [40], [107]. However, over the last decade a lot of effort has been put in formalizing MHSS in ARAIM. Fully adapting the well known bank of KF to the ARAIM definitions, errors and threat models as well as protection level computation still requires additional considerations. In particular, this section presents a strategy to consider the impact of the worst-case nominal bias and the propagation of separate error models in relation to continuity and integrity.

6.3.1 MHSS Architecture and Protection Level Computation

The main processing architecture of the GNSS/INS KF MHSS algorithm is depicted in Fig. 6.2. The determination of the necessary fault modes hypothesis (and therefore number of parallel filters) is determined similarly as in ARAIM ADD based on the probability of fault of the individual satellites, probability of constellation fault, the integrity risk requirement and a certain tolerance [21]. Each hypothesis subset must provide a state vector estimation $\hat{\mathbf{x}}$, an associated covariance for integrity $\hat{\mathbf{P}}_{\mathrm{int}}$ (based on the integrity error model), an associated covariance for accuracy and continuity $\hat{\mathbf{P}}_{\mathrm{acc}}$. The latter is used for accuracy checking and fault detection as well as for the projection of worst-case nominal biases $\mathbf{b}$ in the vertical and horizontal domains. Fault detection is based on solution separation test statistic:

$$q_{ss}^{h} = |\hat{x}^0 - \hat{x}^h|, \tag{6.33}$$

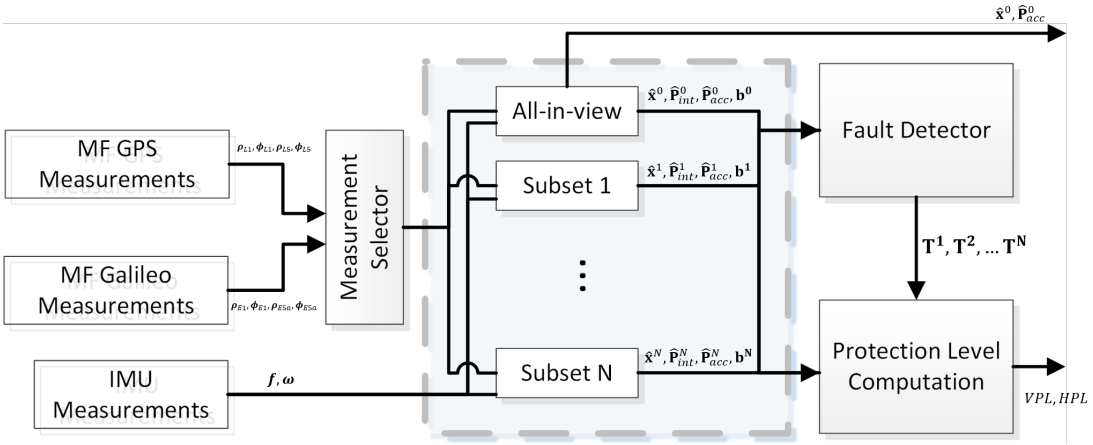

Figure 6.2: GNSS/INS MHSS Processing

and compared to a threshold:

$$T_{ss} = Q^{-1}\left(\frac{P_{fa}}{2N_h}\right)(\sigma_h^2 - \sigma_0^2), \tag{6.34}$$

where notice that $\sigma_h^2 = \boldsymbol{\varepsilon}^T \hat{\mathbf{P}}^h_{acc} \boldsymbol{\varepsilon}$ is extracted from the covariance with the accuracy-continuity model. The Vertical Protection Level (VPL) can be obtained by solving the following implicit equation [21]:

$$\begin{aligned} &2Q\left(\frac{VPL - b_3^0}{\sigma_3^0}\right) + \sum_{h=1}^{N_{\text{fault-mode}}} P_{\text{fault},h} Q\left(\frac{VPL - T_3^h - b_3^h}{\sigma_3^h}\right) = \\ &P_{HMI,v}\left(1 - \frac{P_{\text{sat,notMon}} + P_{\text{const, notMon}}}{P_{\text{HMI, v}} + P_{\text{HMI, H}}}\right). \end{aligned} \tag{6.35}$$

For horizontal, we compute east and north HPL separatelly following:

$$\begin{aligned} &2Q\left(\frac{HPL_l - b_l^0}{\sigma_l^0}\right) + \sum_{h=1}^{N_{\text{fault-mode}}} P_{\text{fault},h} Q\left(\frac{HPL_l - T_l^h - b_l^h}{\sigma_l^h}\right) = \\ &P_{HMI,H}\left(1 - \frac{P_{\text{sat,notMon}} + P_{\text{const, notMon}}}{P_{\text{HMI, v}} + P_{\text{HMI, H}}}\right). \end{aligned} \tag{6.36}$$

Then we HPL is obtained with:

$$HPL = \sqrt{HPL_1^2 + HPL_2^2}. \tag{6.37}$$

In Equation (6.34), Equation (6.35) and Equation (6.36) we recognized the use of different error models for accuracy-continuity and integrity and the use of the worst-case propagated nominal bias to the dimension of interest. The next sections provide some details how to handle this multiple propagation over time in each of the subset filters.

6.3.2 Propagation of Accuracy and Integrity Models

Although the assessment of the accuracy-continuity and integrity error covariance must be considered for the fault detection and for the protection level calculation, these covariances are propagated through the same Kalman filter estimator. The Kalman filter estimator is ultimately characterized by the Kalman gain **K** in Equation (6.28) and computed with the integrity error model. With this in mind, the covariance with the integrity model is just obtained from a normal KF with the integrity model, whereas the accuracy-continuity model is propagated as:

$$\hat{\mathbf{P}}_{\text{acc},k|k-1} = \hat{\mathbf{\Phi}}_k \hat{\mathbf{P}}_{\text{acc},k-1|k-1} \hat{\mathbf{\Phi}}_k^{\mathrm{T}} + \mathbf{G}_k \hat{\mathbf{Q}}_{\text{acc},k} \mathbf{G}_k^{\mathrm{T}}, \tag{6.38}$$

$$\hat{\mathbf{P}}_{\text{acc},k|k} = \left(\mathbf{I} - \hat{\mathbf{K}}_k \mathbf{H}_k\right) \hat{\mathbf{P}}_{\text{acc},k|k-1} \left(\mathbf{I} - \hat{\mathbf{K}}_k \mathbf{H}_k\right)^{\mathrm{T}} + \hat{\mathbf{K}}_k \mathbf{R}_k \hat{\mathbf{K}}_k^{\mathrm{T}}. \tag{6.39}$$

Notice that the expression in Equation (6.39) is used in the update step instead of the compact expression $\mathbf{P}_{k|k} = (\mathbf{I} - \mathbf{KH})\mathbf{P}_{k|k-1}$ since in this situation the projected predicted covariance and the covariance matrix used to compute the Kalman gain are different. Notice also that in Equation (6.39) the Kalman gain from the *integrity-modeled* filter is used. One can also notice that since both covariances will share the same number of states, some of the matrices in Equation (6.39) can be reused for both models and only need to be computed once. Finally, the main purpose of the propagation of the accuracy-continuity model is to derive the solution separation thresholds and to perform an assessment of required accuracy. For this reasons only the covariance is necessary to be propagated.

6.3.3 Nominal Bias Determination

We are interested in determining the worst-case impact of the nominal biases on the desired coordinate of interest. The expected value of the estimated KF error under the presence of nominal biases **b** in the measurements can be expressed for one time epoch as:

$$\mathrm{E}[\mathbf{x}_{k|k}] = (\mathbf{I} - \mathbf{K}_k \mathbf{H}_k) \hat{\mathbf{\Phi}}_k \mathrm{E}[\mathbf{x}_{k-1|k-1}] + \mathbf{K}_k \mathbf{b}_k. \tag{6.40}$$

The impact in any time epoch on the expected value of the aposteriori estimation can be written by using a similar formulation as in [35] as:

$$\mathrm{E}[\mathbf{x}_k] = \underbrace{\begin{bmatrix} \mathbf{A}_{1k} & \cdots & \mathbf{A}_{kk} \end{bmatrix}}_{\mathbf{A}_{\mathrm{K}}} \underbrace{\begin{bmatrix} \mathbf{b}_1 \\ \vdots \\ \mathbf{b}_k \end{bmatrix}}_{\mathbf{b}_{\mathrm{K}}}, \tag{6.41}$$

where

$$\mathbf{A}_{ij} = \begin{cases} \left(\prod_{t=j}^{i+1} (\mathbf{I} - \mathbf{K}_t \mathbf{H}_t) \hat{\mathbf{\Phi}}_t\right) \mathbf{K}_i, & \text{if } i < j, \\ \mathbf{K}_i, & \text{if } i = j. \end{cases} \tag{6.42}$$

In Equation (6.41), the nominal bias at each epoch for each measurement is explicitly considered. The square of the expected error due to the nominal biases in a certain state or coordinate l as:

$$b_l^2 = \mathbf{b}_{\mathrm{K}}^{\mathrm{T}} \mathbf{A}_{\mathrm{K}}^{\mathrm{T}} \boldsymbol{\varepsilon}_l^{\mathrm{T}} \boldsymbol{\varepsilon}_l \mathbf{A}_{\mathrm{K}} \mathbf{b}_{\mathrm{K}}, \tag{6.43}$$

where $\boldsymbol{\varepsilon}_l$ is used to extract the desired coordinate of interest. In principle we only know the possible maximum value of the unmodelled bias (i.e., b_{nom} from ISM message) for each satellite. However, the impact on coordinate l can be bounded by assuming the maximum nominal bias b_{nom} in each satellite for each epoch and the worst-case sign by taking the absolute value of the projection through the estimator:

$$\hat{b}_l \leq |\boldsymbol{\varepsilon}_l^{\mathrm{T}} \mathbf{A}_{\mathrm{K}}| \mathbf{1}^{\mathrm{N}k \times 1} b_{\mathrm{nom}}, \tag{6.44}$$

which is a similar expression as the one used for batch sequential ARAIM in [103]. Notice that this expression can be very conservative in the sense that the worst case sign of the bias is used for every epoch for every satellite. It is also not a practical solution since it implies the storage in memory of the growing size matrix $\mathbf{A}_{\mathrm{K}}$. The evolution of the effects that are condensed in the nominal bias are however not likely to jump from worst case positive to worst case negative or viceversa from epoch to epoch. In order to relaxed this conservatism, it is assumed that the worst case bias is stable over long periods and does not change sign during one approach. This is justified since it has been observed in previous studies that these biases show a constant behaviour for each satellite [108]. Nevertheless, so that the worst case sign that could impact the current estimation is still considered, this sign is assumed for each bias by using the absolution value on each coefficient of the estimator. Then, the matrices in $\mathbf{A}_{\mathrm{K}}$ can be summed by taking a common factor of bias for a single epoch. In this situation, the worst case impact of the nominal bias from Equation (6.44) can be written as:

$$\hat{b}_{l,k} \leq \boldsymbol{\varepsilon}_l^{\mathrm{T}} \left| \underbrace{\sum_{i=0}^{k} \left[\prod_{j=1+i}^{k} \left(\mathbf{I} - \mathbf{K}_j \mathbf{H}_j\right) \hat{\mathbf{\Phi}}_j \right] \mathbf{K}_i}_{\mathbf{S}_k} \right| \mathbf{1}^{\mathrm{N}_s \times 1} b_{\mathrm{nom}}. \tag{6.45}$$

Notice that the estimator matrix $\mathbf{S}_k$ can be written and computed in a recursive fashion as:

$$\mathbf{S}_k = (\mathbf{I} - \mathbf{K}_k\mathbf{H}_k)\,\hat{\mathbf{\Phi}}_k\mathbf{S}_{k-1} + \mathbf{K}_k. \tag{6.46}$$

This approach is therefore a more practical as compared to Equation (6.44). Up to now, Equation (6.45) assumes a constant number of satellites N_s over time. This is in practice not realistic but can be easily handled by slightly modifying the propagation of the estimator matrix $\mathbf{S}_k$ in Equation (6.46) as:

$$\mathbf{S}_k = (\mathbf{I} - \mathbf{K}_k\mathbf{H}_k)\,\hat{\mathbf{\Phi}}_k\mathbf{S}_{k-1}\mathbf{T}_s + \mathbf{K}_k\mathbf{T}_k, \tag{6.47}$$

with $\mathbf{T}_s$ the past time estimator can be adapted to new appearing satellite measurements by including zero columns in $\mathbf{S}_{k-1}$. On the other hand, $\mathbf{T}_k$ can adapt the Kalman gain to previous number of available satellites. Notice that in this way, the number of columns in $\mathbf{S}_k$ will always increase. This is important since past time measurements still have an impact in the projection of nominal biases even if the satellite is not visible anymore at current epoch. This impact of course reduces with time and for operations of longer duration one could consider removing the corresponding column of a *disappeared* satellite after a certain time has passed. The nominal bias is mainly considered to capture signal deformation and therefore it affects only code measurements. Since the measurement vector considers both code and phase measurements in Equation (6.29), to respect the natural size of $\mathbf{S}_k$, $\mathbf{K}_k$ and $\mathbf{H}_k$, Equation (6.45) can be refined as:

$$\hat{b}_{l,k} \leq \boldsymbol{\varepsilon}_l^{\mathrm{T}}\,|\mathbf{S}_k| \begin{bmatrix} \mathbf{1}^{\mathrm{N}_s\times 1} \\ \mathbf{0}^{\mathrm{N}_s\times 1} \end{bmatrix} b_{\mathrm{nom}} \tag{6.48}$$

The impact of the GNSS/INS designed in this chapter with the overbounding error models as well as the performance of protection levels with the bank of Kalman filters and nominal bias determination will be demonstrated in Chapter 7.

7 GNSS/INS MHSS and ARAIM Evaluation

Current ARAIM algorithm analysis consists of estimating the availability coverage maps like the one depicted in Fig. 7.1. For each grid point in the map, availability is computed based on the percentage of time that the system satisfies the integrity, accuracy and continuity requirements over 24 hours time period divided in certain time steps. For an aircraft, the visibility of satellites is determined with respect to horizon and a certain elevation mask (typically 5 degrees). The location of satellites in space are obtained for each time step from a reference GPS and Galileo almanac. This availability analysis gives a good overview of the impact of satellite geometry in ARAIM performance for different locations in the world. It is, however, disconnected from the actual procedures and operations an aircraft might need to follow. In particular, the following aspects are not considered:

- Grid points in space and time are considered disconnected. However, there is a correlation of location and time for particular aircraft operations when obtaining probability of loss of service and thus continuity.
- Satellite visibility is based on horizon visibility with respect to the local-level navigation frame. However, actual tracking is dependent on the visible satellites from the antenna gain pattern and therefore more related to the aircraft body frame. During manoeuvres in airport vicinity, the attitude of the aircraft changes and the horizon visibility is not realistic anymore.
- ARAIM algorithm is based on carrier-smoothed code measurements with typically 100 seconds smoothing time. In the case of the lost and reacquisition of a satellite, the algorithm waits 100 seconds until it can use again the previously lost satellite for position computation.

In the case of evaluating the performance of a GNSS/INS system it is not possible to perform availability in a snapshot way as for ARAIM. The actual accuracy and integrity of a GNSS/INS

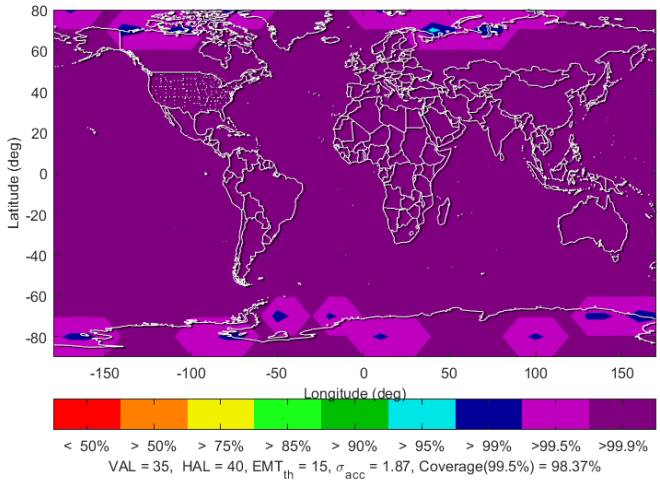

Figure 7.1: ARAIM availability as function of user location [109]

solution is dependent on past conditions and errors. Changing number of visible satellites and encountered dynamics change the filter capacity to estimate/calibrate the INS errors. In this respect, a procedure-based approach is more appropriate and is proposed here to:

1. Assess the performance of the developed GNSS/INS algorithm in Chapter 6 that includes the error overbounding methodology developed in Chapters 4 and 5.

2. Provide new insights about the impact of procedures in the performance of ARAIM algorithm.

3. Being able to assess the expected availability and continuity loss of a GNSS/INS system in a certain relevant scenario or operation.

4. Being able to compare the performance of ARAIM and the GNSS/INS system.

7.1 Procedure-based Simulation

In order to evaluate the behavior of the GNSS/INS system designed in Chapter 6 in a realistic operational scenario, a simulated precision approach landing procedure as shown in Figure 7.2 is created with the DLR multisensor navigation simulator [110]. This approach is a half race-track procedure starting from a holding position at 7000ft (around 2.1 km) Above Ground Level (AGL) with 200 knots (around 100 m/s) speed. For the turn, the bank angle is at its maximum of 25 degrees as specified in [111], which is a worst case trajectory (i.e., highest likelihood of losing visible low-elevation satellites due to banking). More realistic dynamics for the procedures could be additionally considered based on true airspeed and tailwind,

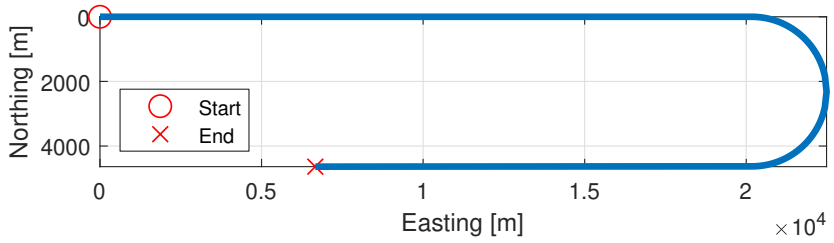

(a) Horizontal Profile

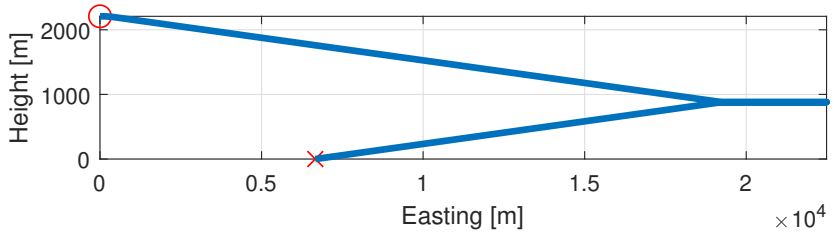

(b) Height profile

Figure 7.2: Simulated half race-track procedure

but these are beyond the scope of this work. From the generated trajectory in Fig. 7.2, IMU measurements are simulated at 100Hz. GNSS measurements are assumed to be present at 1 Hz at the receiver from satellites at locations based on GPS and Galileo almanac data.

Figure 7.3 shows an example of the evolution of visible satellites over the trajectory in Fig. 7.2 at Munich Airpot (EDDM). It can be seen that due to the banking of the aircraft, the number of visible satellites drops during the turn. This will have several implications in the expected performance and behaviour of GNSS PVT algorithms and the GNSS/INS integrated system.

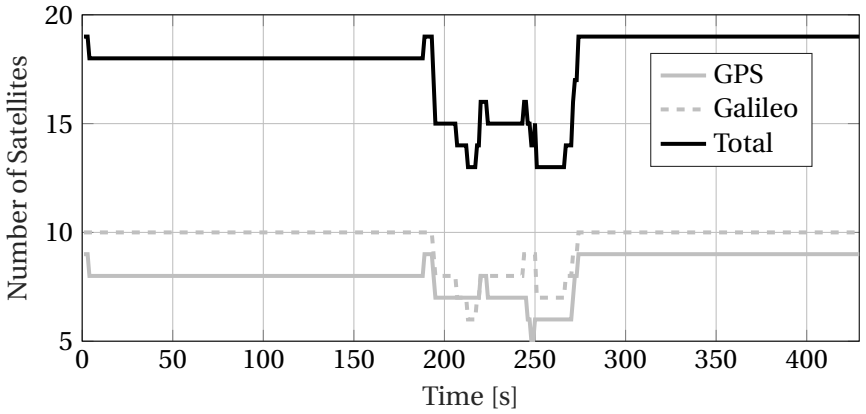

Figure 7.3: Evolution of number of visible satellites during half race-track procedure

7.2 Covariance Bounding Analysis

The new error models derived in Chapter 4 and 5 guarantee bounding conditions under uncertain GMP error models. Based on the uncertain GNSS error models presented in Table 6.1, the estimation with error bounding can be verified for a given set of true underlying parameters; for instance by sensitivity analysis as shown in Appendix A.1. There are however multiple possible combinations of true GNSS error parameters for a given situation. In order to validate that the GNSS/INS system provides error estimation that overbounds the uncertain errors, covariance analysis are performed over the trajectory and conditions described in Section 7.1. For the simulation and analysis the filter has been initiated one hour before starting the final approach procedure. This initialization consists of replicating the available satellite measurements at the beginning of the trajectory for this period of time. This is a standard procedure to reflect better the status of the filter in real operations, avoiding the effect of a convergence and/or transition phase [8] (e.g., large mis-alignments, unknown biases of inertial sensors, etc.). A navigation grade inertial sensor is considered for this first analysis with the parameters shown in Table 6.4. In Fig. 7.4, the difference between estimated and true error variance is presented for some extreme cases of true error model parameters: when all time correlation constants of the GNSS GMP errors are i) at their possible minimum, ii) at their possible maximum and iii) in the middle of their possible range. The analysis completes by considering both stationary and non-stationary GMP bounding models when using the integrity error model over the trajectory in Fig. 7.2 consistent with the visible satellites in Fig. 7.3.

Figure 7.4 first shows that all the curves are in the positive region. This means that the designed GNSS/INS KF correctly overbounds the uncertain underlying error under all situations. Up to around half a meter difference can be observed in these situations. This conservatism is the *price to pay* for the lack of knowledge of the exact value of error model parameters and thus possible process realization in a given moment. The results in Fig. 7.4 also show that the non-stationary models are less conservative when new satellites appear, which mainly happens when the aircraft starts banking just before $t = 200$ s.

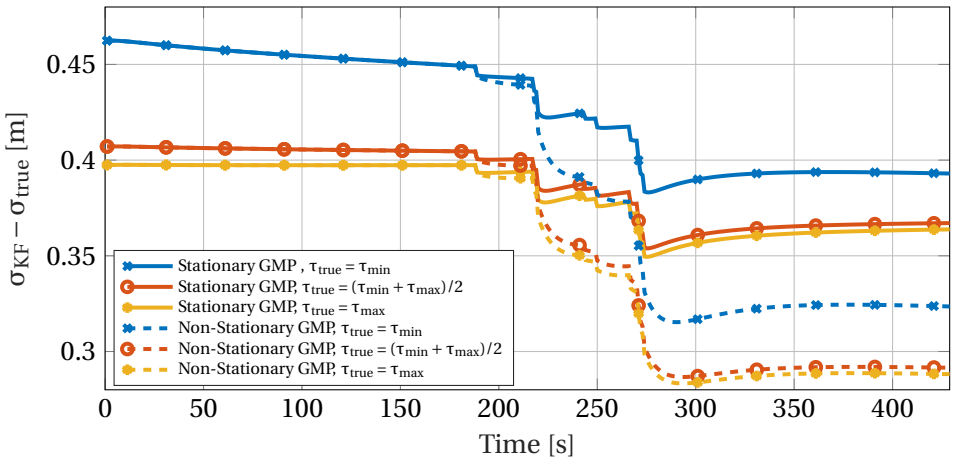

(a) Horizontal

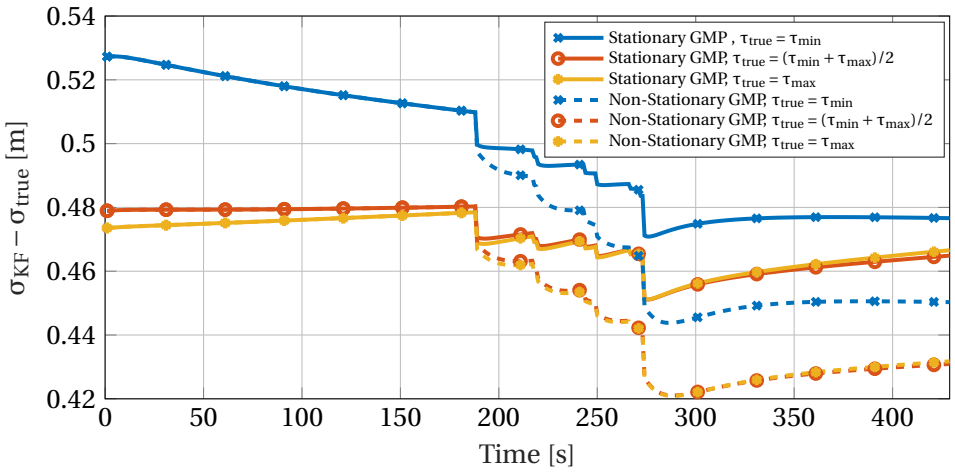

(b) Vertical

Figure 7.4: Difference of estimated KF standard deviation with error bounding (σ_{KF}) and true KF error standard deviation for different cases of GMP true parameters

7.3 Algorithm Performance Results

7.3.1 Fault-Free Accuracy

The first important requirement for approach operations is the accuracy. For the simulated scenario described previously, Fig. 7.5 depicts the standard deviation extracted from the GNSS/INS covariances for the following error model configurations:

- **Stationary GMP**: The filter is configured with the GNSS errors modelled with the GMP stationary bounding model.

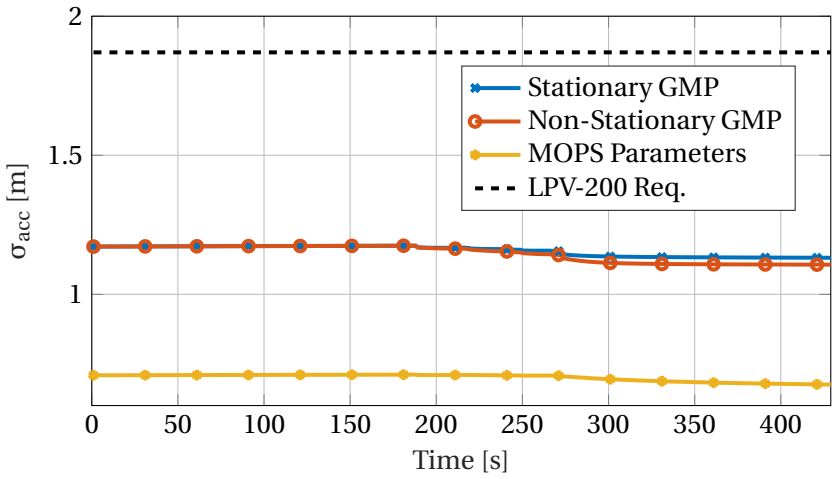

Figure 7.5: Fault-free accuracy results

- **Non-Stationary GMP**: The filter is configured with the GNSS errors modelled with the GMP non-stationary bounding model.
- **MOPS parameters**: The filter is configured with the same augmented states as described in Chapter 6 but using as time-correlation constants for satellite clock-ephemeris, troposphere and multipath as proposed in avionic standards (e.g., [8]). Note that since specific models are not currently available for Galileo in MOPS, the GPS time constants are also for Galileo.

In Fig. 7.5, the most restrictive accuracy requirement for LPV-200 is also shown as a reference. The new GMP bounding models with the proposed parameters in Chapter 6 are significantly more conservative than the GNSS/INS with the DO-384 time correlation constants. However, from what it has been observed in the literature, it might be that the parameters proposed in MOPS do not capture completely all the range of possible time-correlation error behaviour (e.g., in satellite orbit and clock errors), which could lead to misleading information in some situations. Even though more conservative, during the whole procedure the GNSS/INS system with both fully stationary or non-stationary models still satisfy (with good margin) the LPV-200 accuracy requirement while accounting for the range of variations in time-correlated errors.

7.3.2 Protection Level Evolution

Vertical ARAIM targets to support LPV-200 operations. However, during certain maneuvers, the possible loss of visible satellites can compromise the availability and continuity of the approach. In this sense, it is relevant to study the possible gain when using a coupled GNSS/INS system that still respects most of the algorithm description and parameters that are already

Table 7.1: ARAIM-GNSS/INS MHSS Simulation Parameters

Parameter	Description	Value
P_{HMI}	Total Integrity budget per approach	10^{-7}
P_{FA}	Probability of false alarm (Continuity risk)	$4 \cdot 10^{-6}$
VAL	Vertical Alert Limit	35 m.
b_{nom}	Maximum nominal bias for integrity	0.75 m.
P_{sat}	Prior probability of satellite fault per approach	10^{-5}
$P_{const,\,GPS}$	Probability of GPS constellation fault per approach	10^{-8}
$P_{const,\,GAL}$	Probability of Galileo constellation fault per approach	10^{-4}

set for VARAIM. One of the key parameters is the accuracy, as shown in the previous section. The other main indicator to determine whether the system is available for the user is the comparison of the computed protection level with respect to the alert limit (AL).

Table 7.1 summaries the parameters that are used for the ARAIM and GNSS/INS protection level (PL) simulations. The values are based on typical values set in the ARAIM ADD [112] and are the same for both estimators. Figure 7.6 presents the vertical PLs (VPL) obtained under the following algorithms. First and as a reference, the ARAIM VPL assuming that satellites could be incorporated immediately into the snapshot PVT algorithm once they become visible (ARAIM snapshot visibility). This is not a realistic situation due to the typical 100 second smoothing time the carrier-smoothing (CS) filters need to reinitialize. It is, however, here shown as a reference since this assumption is the one taken for current ARAIM availability and coverage analysis world-wide. The VPL performance assuming the reinitialization of the smoothing filters is also considered (ARAIM CS reinit). Finally, the VPL obtained with the GNSS/INS algorithm under the different error models as before, that is, assuming the time correlation constant from avionics MOPS, with the stationary GMP model and with the non-stationary GMP model. Figure 7.6b provides a zoomed version of the latter cases. In Fig. 7.6, the impact of carrier-smoothing filter reinitialization can be observed. This reinitialization may expand significantly the period of time when VPL exceeds VAL, which is considered as a loss of continuity. In this sense the GNSS/INS integrity monitoring algorithm is able to maintain almost a constant (and lower) VPL over the whole operation and thus *bridge* the possible ARAIM gaps during aircraft manoeuvres. It is, however, worth mentioning that for more stringent operations, where for instance a VAL of 10 m. would be necessary, the current setup with the selected sensor (e.g. lack of a barometer) and error models might still find difficult to satisfy. In the next section a more complete study on the probability of loss of continuity is presented.

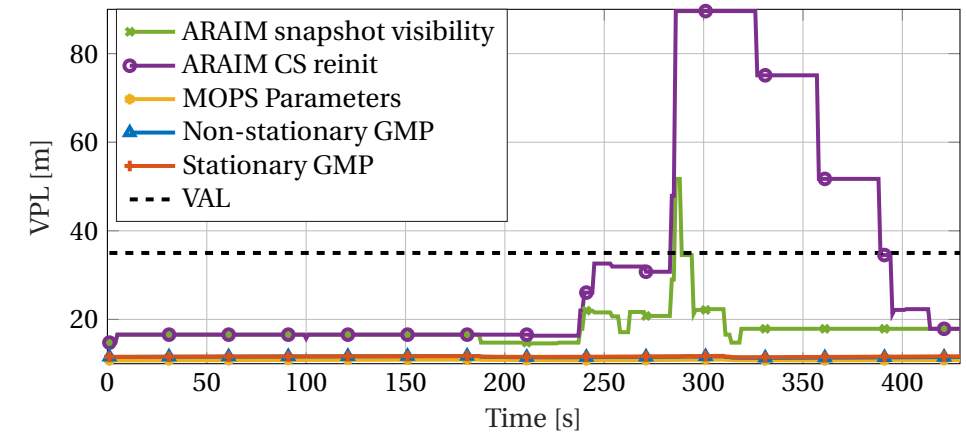

(a)

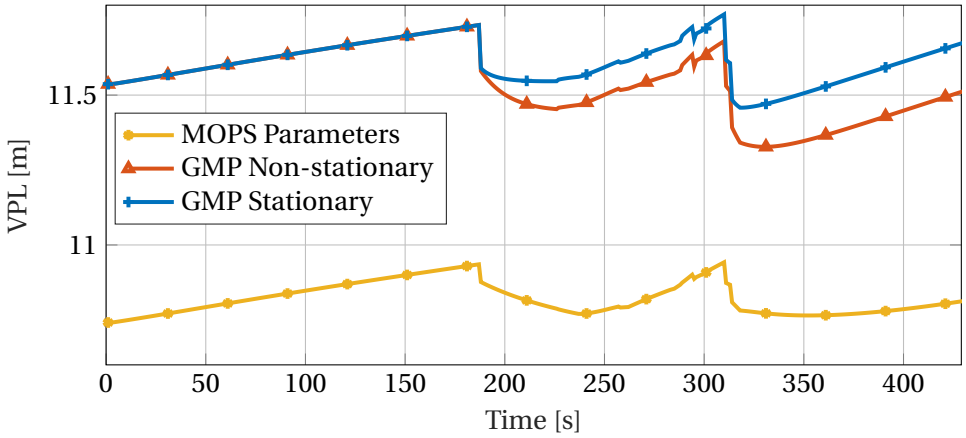

(b)

Figure 7.6: Impact of aircraft dynamic and smoothing on VPL (Racetrack Trajectory, EDDM airport, runway 08L for operation starting at 17:20)

7.3.3 Impact of Sensor Quality

In this section, the GNSS/INS MHSS algorithm is evaluated considering a tactical-grade inertial sensor instead of the navigation grade one used in the previous results. The characteristics of the model are as presented in Table 6.3 and 6.4. Fig. 7.7 depicts the achieved accuracy and VPL with the two different quality of inertial sensors.

Under the simulation conditions of this research, the difference in performance is small (or even negligible) in relation to the operational requirements of LPV-200. The reason is that the expected performance with different sensors deviates when few or none satellites are visible and the solution is mainly driven by the inertial coasting. In the case of a sufficient high number of available satellite measurements and their respective geometry, the filter is able

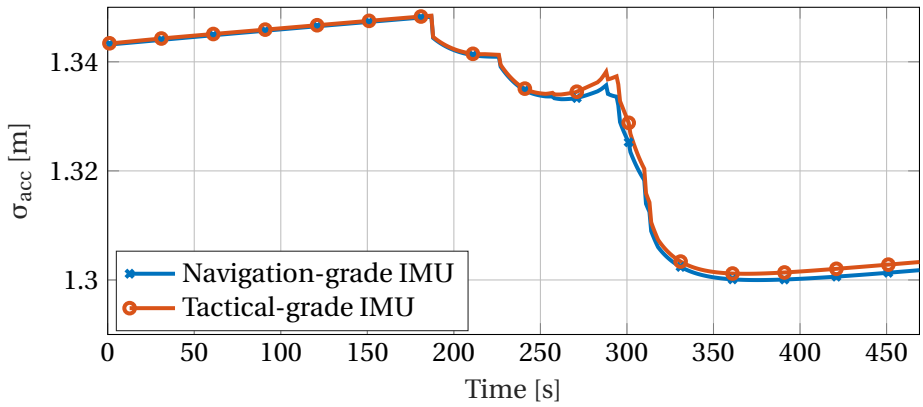

(a) Fault-free accuracy

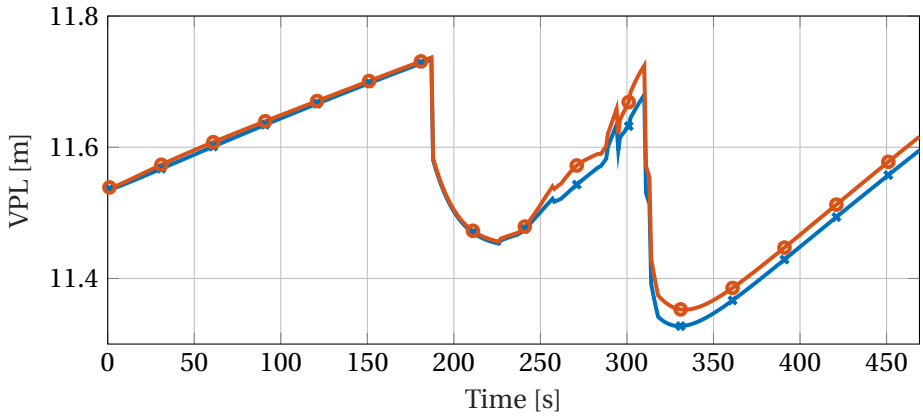

(b) Vertical Protection Level

Figure 7.7: Performance with different inertial sensor grades

to maintain a good estimation of the INS errors. In the case of reduced number of satellites, the impact of inertial quality would become more observable after a larger time interval. This can be seen in Fig. 7.7 after second 250 when some satellites are not longer tracked. Recall that one hour of stable conditions with all available satellite measurements were considered before starting the simulated procedure. This is why both filters with different IMU sensors have very similar performance at the first 200 seconds on the plot.

7.3.4 Loss of Continuity Analysis

In general sense the continuity risk or probability of loss of continuity (LOC) is defined as the probability of a detected but unscheduled navigation function interruption after an operation has been initiated [113]. The authors in [114] expressed the total continuity risk as:

$$P_{LOC} = P_{LOC,alert} + P_{LOC,PL>AL} + P_{LOC,other}, \tag{7.1}$$

where $P_{LOC,alert}$ is primary linked with fault detection alerts at the receiver, $P_{LOC,other}$ are cases of loss of service due to other reasons like presence of RF interference or ionospheric scintillation, and $P_{LOC,PL>AL}$ is a loss of continuity due to violation of integrity risk or alert limit. Alert limit violation can happen for several reasons, for instance due to a very unfavorable nominal geometry, an unusually high user range accuracy (URA) or due to unscheduled satellite outages [114]. However, a bad geometry situation can arise, as it was shown in the previous section, due to aircraft manoeuvres during an approach. Another source of satellite measurement outage that can lead to geometry degradation is due to carrier-phase cycle slips, which are initially not considered in the fault detection continuity budget while are likely to happen in real operation. In this section, the impact of manoeuvres in loss of continuity is further evaluated via simulations. If ARAIM is not performing availability predictions based on real type of operations and assuming that at least some type of banking is always necessary during an approach, loss of visible satellites during manoeuvres and smoothing filter reinitialization has to be considered as an unscheduled event.

Each airport has in principle their specific approach procedures, so it is difficult to make general statements about the expected type of manoeuvres. However, some common patterns can be found in many of them and can be considered as general *templates* for the availability and continuity analysis during operation. One of them is the half race track shape presented in Fig. 7.2 which is a typical pattern use to reduce altitude during the intial approach segment and it is also part of a holding pattern, where ATM could send an aircraft to if necessary (e.g., due to airport congestion). Furthermore, this pattern contains a turn with a worst-case banking angle, and therefore could be considered an extreme situation for ARAIM.

In order to perform simulations that are closer to the actual operational scenarios, the methodology in Fig. 7.8 is considered. From public databases, a list of airports and information about their runways can be extracted. In this work the data from [115] has been used for such purpose. For each runway the geographical location of the start as well as the heading angle of the runway is known. Whether the runway is a left or right side approach entry is also provided when applicable. With this information, a *template* procedure can be translated and rotated so that it is aligned to a Final Approach Fix (FAF). In order to capture the temporal dynamics of the GNSS constellations the operation can be initiated based on a time grid similar as for

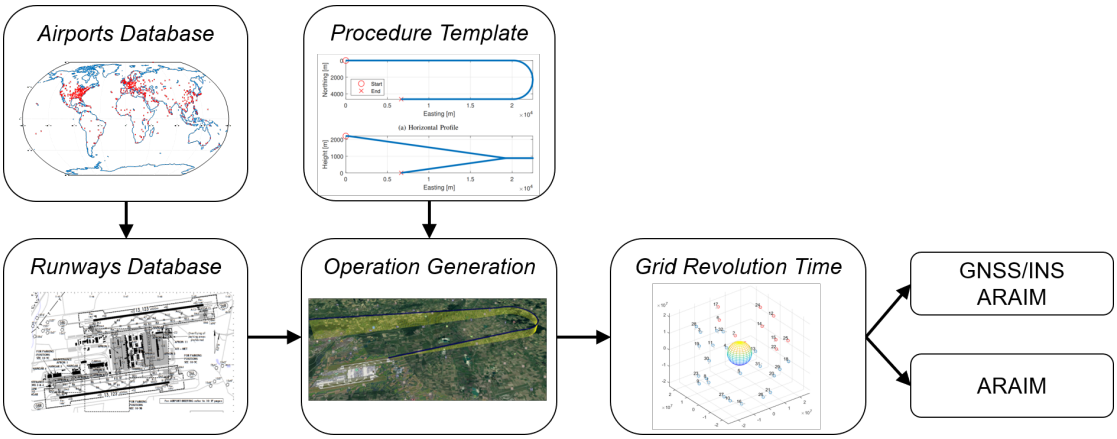

Figure 7.8: Availability Study Methodology

Table 7.2: V-ARAIM Probability of loss of availability and continuity due to racetrack procedure in EDDM airport, considering four runways.

	(1 - Prob. loss Avail.)x100	(1 - Prob. loss Cont.)x100
V-ARAIM (Snapshot)	99.77	87.63
V-ARAIM (smoothing reinit)	87.6	61.19
GNSS/INS KF ARAIM	100	100

ARAIM availability studies and then narrowed down to the visible satellites at aircraft attitude i.e., the visible satellites at the antenna level.

Based on the methodology in Fig. 7.8 and approaches every 5 minutes, Table 7.2 shows the average over 4 runways in Munich airport (EDDM) in terms of availability and continuity for: ARAIM assuming snapshot satellite visibility, ARAIM with smoothing filter reinitialization and the GNSS/INS system presented in Chapter 6 with the non-stationary GMP model. The probability of loss of availability is computed epoch-based irrespective of the operation. Probability of loss of continuity is based on each of the initiated operations, that is, if the protection level exceeds the alert limit at least at one epoch during an operation, that operation is counted as a loss of continuity event. As it is shown in Table 7.2, the maneuver procedure has a big impact on ARAIM continuity. The results suggests that the integration of inertial with GNSS with ensured error bounding and integrity monitoring presented in this work can mantain 100% continuity during the ARAIM *gaps* for LPV-200.

Finally, Fig. 7.9 shows the obtained V-ARAIM loss of continuity for different airports around the world averaged over their specific number of runways. The GNSS/INS ARAIM algorithm simulated here is able to guarantee the 100% continuity in all of them. Due to the simulated pattern of trajectory, it appears that the loss of continuity is similar in all of them. It should be noted, however, that such trajectory might be possible yet rare to be used at some airports.

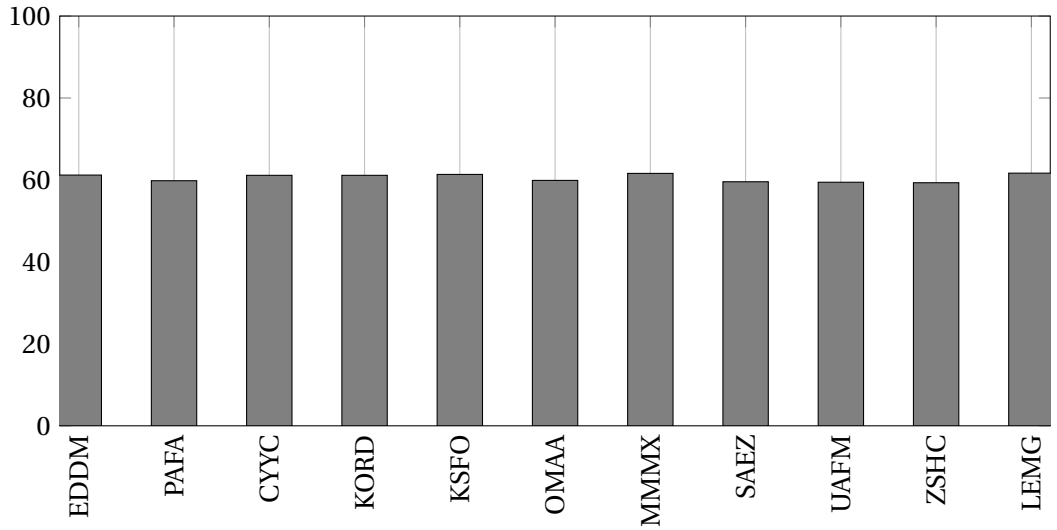

Figure 7.9: (1 - Prob. loss of Continuity)x100 at different airports due to approach procedure with banking angle of 25 degrees

Moreover, the probability of having a specific type of operation should be also considered for a final statement of loss of continuity. In any case, the simulations performed here may provide a guidance to a first worst-case assessment on this matter.

Closing Part IV

8 Concluding Remarks

8.1 Summary

This work has provided new tools, methods and models to handle uncertainty in model parameters of time-correlated error processes in their subsequent use in estimation. This topic and results can be of great importance for several emerging applications that are now considering integrated navigation with state-space estimators like Kalman filtering for safety-critical operation. The new models to handle Gauss-Markov model parameter uncertainty have been applied to GNSS/INS estimation by leveraging and creating links between current MOPS standards, ARAIM and recent literature.

The main achievements based on this work can be summarized as:

1. **Uncertainty in study time-correlated processes.** Model-parameter uncertainty is quite common in real physical systems. This work has provided new leads how to handle such uncertainty in time-correlated processes employed within safety-related applications, by creating a link between model behaviour in time to guarantee correct estimation uncertainty of impacted parameters with sequential estimators.

2. **Gauss-Markov Process Bounding.** Gauss-Markov processes are of widespread used in different communities due to their facility to be incorporated in linear estimators. This work has provided rigorous derivation of new bounding model parameters with theoretical proofs. These can be used to select the parameters of uncertain GMP to ensure covariance bounding conditions of linear estimators.

3. **GNSS/INS MHSS Architecture with Uncertain Time Correlated Models.** While leveraging on previously derived GMP bounding, a complete GNSS/INS integrity monitoring design has been presented based on a multiple hypothesis solution separation algorithm that allows for a closer comparison with current ARAIM and can facilitate the use of

Dual Frequency, Multi-constellation GNSS/INS for safety critical purposes.

4. **Impact of trajectory on loss of continuity.** Inertial systems are always mentioned as the possible main contributor to improve continuity of the navigation system. In this work, a direct study has been provided that shows its potential to guarantee continuity independently on the actual trajectory and banking of the aircraft.

8.2 Conclusions

Future updates to avionics standards dealing with GNSS/INS integration will consider dual frequency, multi-constellation GNSS as the main driver to increase performance. In order to ensure correct integrity risk quantification, the potential uncertain nature of time-correlated GNSS (or inertial) errors and related models must be taken into account. This research has provided theoretical bounding criteria that can support this objective and its impact on the final estimation result. The derivation of new parameters for Gauss-Markov model ensuring bounding conditions provides a rigorous insights that can be easily implemented by designers. Furthermore, with the increment of emerging applications that require navigation safety assurance, the results of this research work can support certain aspect for the certification of navigation algorithms using state-space estimators.

8.3 Future Work

- **Inclusion of uncertain IMU error models.** This thesis focused on the impact of uncertain GNSS error sources on the GNSS/INS Integrity Monitoring results. IMU errors are also expected to have some level of uncertainty, in particular for lower-cost IMUs. Further work could tackle the uncertainty in IMU model parameters.

- **Optimization of Kalman Filter MHSS with augmented states.** The state vector of the designed GNSS/INS KF in this work was very large. In fact, most of the augmented states for the uncertain GNSS errors had only the role of properly accounting for the necessary uncertainty, but their observability might not be possible. On one side, some optimization could be applied to reduce complexity of the bank of KFs by exploiting similarities between subsets. On the other side, some other methodologies could be used to avoid the use of many augmented states, for instance measurement differencing.

- **Impact of non-linearities in EKF.** The analysis performed in Chapter 7 were done considering a linearized Kalman filter. The possible impact of non-linearities in the overbounding capability of the filter, in particular during strong manoeuvres, should be addressed in the future. In the case of navigation grade IMUs, the impact is expected to be small and it does not seem to pose a big concern in the aviation community. When

using tactical grade or low-cost IMUs, this impact could reach some importance due to the significantly higher drift in heading and higher amplitude of sensor errors in general.

- **Evaluation of GNSS Multipath based on Real Data.** One of the most challenging error sources to model is multipath. In this work a wide range for the time correlation of multipath was used. Further studies could address a dedicated evaluation of real multipath in aircraft or for other vehicles so that the time-correlation range can be reduced and to avoid possible extra conservatism in the estimation.

- **Non-Gaussian Error Processes.** In this work, the new derived bounding models are assumed to be Gaussian, or in the application GNSS/INS case, it was assumed that the provided variances for each error were bounding the underlying empirical distribution. Further work could study new methods to account for non-Gaussian error processes and their impact on the final estimation [116].

Appendix Part V

A KF Sensitivity Analysis and Bounding

A.1 Discrete KF True error Covariance

Consider a general discrete-time linear dynamic system described as follows:

$$\mathbf{x}_k = \mathbf{\Phi}\mathbf{x}_{k-1} + \mathbf{G}_k\mathbf{w}_k, \tag{A.1}$$

$$\mathbf{z}_k = \mathbf{H}_k\mathbf{x}_k + \mathbf{v}_k. \tag{A.2}$$

where $\mathbf{x}$ is the state vector, $\mathbf{\Phi}$ the transition matrix and $\mathbf{w}$ the process noise with $\mathrm{E}[\mathbf{w}\mathbf{w}^{\mathrm{T}}] = \mathbf{Q}$. Additionally, $\mathbf{G}$ is the process noise projection matrix, $\mathbf{z}$ is the measurement vector, $\mathbf{H}$ the measurement matrix and $\mathbf{v}$ the measurement noise. A Kalman filter estimator that designs *imperfectly* $\mathbf{\Phi}$ and $\mathbf{Q}$ with $\hat{\mathbf{\Phi}}$, and $\hat{\mathbf{Q}}$ respectively, can be written as:

$$\hat{\mathbf{x}}_{k|k-1} = \hat{\mathbf{\Phi}}\hat{\mathbf{x}}_{k-1|k-1}, \tag{A.3}$$

$$\hat{\mathbf{P}}_{k|k-1} = \hat{\mathbf{\Phi}}_k\hat{\mathbf{P}}_{k-1|k-1}\hat{\mathbf{\Phi}}_k^{\mathrm{T}} + \mathbf{G}_k\hat{\mathbf{Q}}_k\mathbf{G}_k^{\mathrm{T}}, \tag{A.4}$$

$$\hat{\mathbf{K}}_k = \hat{\mathbf{P}}_{k|k-1}\mathbf{H}_k^{\mathrm{T}}\left(\mathbf{H}_k\hat{\mathbf{P}}_{k|k-1}\mathbf{H}_k^{\mathrm{T}} + \mathbf{R}_k\right)^{-1}, \tag{A.5}$$

$$\hat{\mathbf{x}}_{k|k} = \hat{\mathbf{x}}_{k|k-1} + \hat{\mathbf{K}}_k\left(\mathbf{z}_k - \mathbf{H}_k\hat{\mathbf{x}}_{k|k-1}\right), \tag{A.6}$$

$$\hat{\mathbf{P}}_{k|k} = \left(\mathbf{I} - \hat{\mathbf{K}}_k\mathbf{H}_k\right)\hat{\mathbf{P}}_{k|k-1}. \tag{A.7}$$

where $\mathbf{R}$ is the measurement noise covariance matrix.Notice that because the filter is imperfectly designed, the state covariance matrix $\hat{\mathbf{P}}_{k|k}$ is not guaranteed to bound the actual true error in $\hat{\mathbf{x}}_{k|k}$. In [33] a methodology is proposed to study the sensitivity of the imperfect modeling for a continuous Kalman filter. In [73] similar expressions can be found for the hybrid Kalman filter. This appendix follows the same approach to derive the true covariance error for the complete discrete-time Kalman filter.

Let us define the error vector $\mathbf{e} \hat{=} \hat{\mathbf{x}} - \mathbf{x}$. The KF prediction step can be then written as:

$$\begin{aligned}\mathbf{e}_{k|k-1} &= \hat{\mathbf{x}}_{k|k-1} - \mathbf{x}_k \\ &= \hat{\mathbf{\Phi}}\hat{\mathbf{x}}_{k-1|k-1} - \mathbf{\Phi}\mathbf{x}_{k-1} - \mathbf{G}_k\mathbf{w}_k.\end{aligned} \tag{A.8}$$

where Equation (A.1) has been used to substitute the true state vector. Defining now $\Delta\mathbf{\Phi} \hat{=} \hat{\mathbf{\Phi}} - \mathbf{\Phi}$, Equation (A.8) leads to:

$$\mathbf{e}_{k|k-1} = \hat{\mathbf{\Phi}}\mathbf{e}_{k-1|k-1} + \Delta\mathbf{\Phi}\mathbf{x}_{k-1} - \mathbf{G}\mathbf{w}_k. \tag{A.9}$$

In order to propagate this error over time, we can consider the time propagation of the extended vector $\boldsymbol{\zeta} = \begin{bmatrix} \mathbf{e}^{\mathrm{T}} & \mathbf{x}^{\mathrm{T}} \end{bmatrix}^{\mathrm{T}}$ as:

$$\begin{bmatrix} \mathbf{e}_{k|k-1} \\ \mathbf{x}_k \end{bmatrix} = \begin{bmatrix} \hat{\mathbf{\Phi}} & \Delta\mathbf{\Phi} \\ \mathbf{0} & \mathbf{\Phi} \end{bmatrix} \begin{bmatrix} \mathbf{e}_{k-1|k-1} \\ \mathbf{x}_{k-1} \end{bmatrix} + \begin{bmatrix} -\mathbf{G}_k\mathbf{w}_k \\ \mathbf{G}_k\mathbf{w}_k \end{bmatrix}, \tag{A.10}$$

whose associated covariance is:

$$\mathbf{P}_{\zeta,k|k-1} = \begin{bmatrix} \hat{\mathbf{\Phi}} & \Delta\mathbf{\Phi} \\ \mathbf{0} & \mathbf{\Phi} \end{bmatrix} \mathbf{P}_{\zeta,k-1|k-1} \begin{bmatrix} \hat{\mathbf{\Phi}} & \Delta\mathbf{\Phi} \\ \mathbf{0} & \mathbf{\Phi} \end{bmatrix}^{\mathrm{T}} + \begin{bmatrix} \mathbf{G}_k\mathbf{Q}_k\mathbf{G}_k^{\mathrm{T}} & -\mathbf{G}_k\mathbf{Q}_k\mathbf{G}_k^{\mathrm{T}} \\ -\mathbf{G}_k\mathbf{Q}_k\mathbf{G}_k^{\mathrm{T}} & \mathbf{G}_k\mathbf{Q}_k\mathbf{G}_k^{\mathrm{T}} \end{bmatrix}. \tag{A.11}$$

For the update step we proceed in a similar way:

$$\begin{aligned}\mathbf{e}_{k|k} = \hat{\mathbf{x}}_{k|k} - \mathbf{x}_k &= \left(\mathbf{I} - \hat{\mathbf{K}}_k\mathbf{H}_k\right)\hat{\mathbf{x}}_{k|k-1} + \hat{\mathbf{K}}_k\mathbf{z}_k - \mathbf{x}_k \\ &= \left(\mathbf{I} - \hat{\mathbf{K}}_k\mathbf{H}_k\right)\mathbf{e}_{k|k-1} - \hat{\mathbf{K}}_k\mathbf{v}_k,\end{aligned} \tag{A.12}$$

which leads to the extended update expression:

$$\begin{bmatrix} \mathbf{e}_{k|k} \\ \mathbf{x}_k \end{bmatrix} = \begin{bmatrix} \left(\mathbf{I} - \hat{\mathbf{K}}_k\mathbf{H}_k\right) & \mathbf{0} \\ \mathbf{0} & \mathbf{I} \end{bmatrix} \begin{bmatrix} \mathbf{e}_{k|k-1} \\ \mathbf{x}_k \end{bmatrix} + \begin{bmatrix} -\hat{\mathbf{K}}_k\mathbf{v}_k \\ \mathbf{0} \end{bmatrix} \tag{A.13}$$

and whose associated covariance is now:

$$\mathbf{P}_{\zeta,k|k} = \begin{bmatrix} \left(\mathbf{I} - \hat{\mathbf{K}}_k\mathbf{H}_k\right) & \mathbf{0} \\ \mathbf{0} & \mathbf{I} \end{bmatrix} \mathbf{P}_{\zeta,k|k-1} \begin{bmatrix} \left(\mathbf{I} - \hat{\mathbf{K}}_k\mathbf{H}_k\right) & \mathbf{0} \\ \mathbf{0} & \mathbf{I} \end{bmatrix}^{\mathrm{T}} + \begin{bmatrix} \hat{\mathbf{K}}_k\mathbf{R}_k\hat{\mathbf{K}}_k^{\mathrm{T}} & \mathbf{0} \\ \mathbf{0} & \mathbf{0} \end{bmatrix}. \tag{A.14}$$

The true error covariance of the states of interest, i.e., $\mathbf{P} = \mathrm{E}[\mathbf{e}\mathbf{e}^{\mathrm{T}}]$ can be extracted from the upper block of the covariance matrix $\mathbf{P}_\zeta$.

Notice also that Equation (A.14) cannot be written in a simplified fashion as in Equation (A.7)

because the covariance of the prediction of $\mathbf{e}_{k|k-1}$ is different from the one that is used to compute the Kalman gain, which is based on the *imperfectly* designed Kalman filter estimator.

Finally, the initial state covariance $\hat{\mathbf{P}}_0$ must also be set according to the design. Assuming an error state implementation of the filter where $\mathrm{E}[\mathbf{x}_0] = 0$, the initialization of the extended matrix used for the sensitivity analysis is described as:

$$\mathbf{P}_{\zeta,0} = \begin{bmatrix} \mathbf{P}_0 & -\mathbf{P}_0 \\ -\mathbf{P}_0 & \mathbf{P} \end{bmatrix}. \tag{A.15}$$

Using Equation (A.15), Equation (A.11) and Equation (A.14) it is possible to obtain recursively the true error KF covariance matrix over time.

A.2 Derivation of Auxiliary Process Covariance in Discrete-Time

This appendix derives the variance of the individual auxiliary processes used for the derivation of non-stationary GMP bound parameters in Section 5.2.

The expression of discrete-time LDS where the error due to misdesigned time-correlated GMP is isolated by augmenting the state vector is [73]:

$$\begin{bmatrix} \mathbf{e}_k \\ \mathbf{a}_k \end{bmatrix} = \begin{bmatrix} \hat{\mathbf{F}} & \Delta\mathbf{F} \\ \mathbf{0} & \mathbf{L} \end{bmatrix} \begin{bmatrix} \mathbf{e}_{k-1} \\ \mathbf{a}_{k-1} \end{bmatrix} + \begin{bmatrix} -\mathbf{w}_k \\ \mathbf{w}_k \end{bmatrix}, \tag{A.16}$$

with associated predicted covariance matrix:

$$\mathbf{P}_{\zeta,k|k-1} = \begin{bmatrix} \hat{\mathbf{F}} & \Delta\mathbf{F} \\ \mathbf{0} & \mathbf{L} \end{bmatrix} \mathbf{P}_{\zeta,k-1|k-1} \begin{bmatrix} \hat{\mathbf{F}} & \Delta\mathbf{F} \\ \mathbf{0} & \mathbf{L} \end{bmatrix}^{\mathrm{T}} + \mathbf{Q}_k. \tag{A.17}$$

On the other side, the KF estimated covariance matrix can also be augmented with an auxiliary process to a similar shape as Equation (A.17):

$$\boldsymbol{\Sigma}_{k|k-1} = \begin{bmatrix} \hat{\mathbf{F}} & \mathbf{0} \\ \mathbf{0} & \mathbf{L} \end{bmatrix} \boldsymbol{\Sigma}_{k-1|k-1} \begin{bmatrix} \hat{\mathbf{F}} & \mathbf{0} \\ \mathbf{0} & \mathbf{L} \end{bmatrix}^{\mathrm{T}} + \begin{bmatrix} \hat{\mathbf{Q}}_k & \mathbf{0} \\ \mathbf{0} & \bar{\mathbf{Q}}_k \end{bmatrix}, \tag{A.18}$$

where Σ is a block diagonal matrix. In order to be able to compare Equation (A.17) and Equation (A.18), we can introduce the block cross matrices in the propagation matrices in

Equation (A.18) by rewriting it as:

$$\boldsymbol{\Sigma}_{k|k-1} = \begin{bmatrix} \hat{\mathbf{F}} & \Delta\mathbf{F} \\ \mathbf{0} & \mathbf{L} \end{bmatrix} \boldsymbol{\Sigma}_{k-1|k-1} \begin{bmatrix} \hat{\mathbf{F}} & \Delta\mathbf{F} \\ \mathbf{0} & \mathbf{L} \end{bmatrix}^{\mathrm{T}} \begin{bmatrix} \hat{\mathbf{Q}}_k - \Delta\mathbf{F}\boldsymbol{\Sigma}_{\mathrm{a}}\Delta\mathbf{F}^{\mathrm{T}} & -\Delta\mathbf{F}\boldsymbol{\Sigma}_{\mathrm{a}}\mathbf{L}^{\mathrm{T}} \\ -\mathbf{L}\boldsymbol{\Sigma}_{\mathrm{a}}\Delta\mathbf{F}^{\mathrm{T}} & \bar{\mathbf{Q}}_k \end{bmatrix}. \tag{A.19}$$

The value of $\bar{\mathbf{Q}}_k$ can be derived by considering the first condition in Equation (5.50). Using the transformation $\boldsymbol{\Delta} = \boldsymbol{\Sigma} - \mathbf{P}$, the difference between Equation (A.17) and Equation (A.19) is:

$$\begin{aligned} \boldsymbol{\Delta}_{k|k-1} &= \begin{bmatrix} \hat{\mathbf{F}} & \Delta\mathbf{F} \\ \mathbf{0} & \mathbf{L} \end{bmatrix} \boldsymbol{\Delta}_{k-1|k-1} \begin{bmatrix} \hat{\mathbf{F}} & \Delta\mathbf{F} \\ \mathbf{0} & \mathbf{L} \end{bmatrix}^{\mathrm{T}} + \\ &\begin{bmatrix} \hat{\mathbf{Q}}_{\xi,k} - \mathbf{Q}_{\xi,k} & \mathbf{0} & \mathbf{0} \\ \mathbf{0} & \hat{\mathbf{Q}}_{\mathrm{a}} - \Delta\mathbf{L}\boldsymbol{\Sigma}_{\mathrm{a}}\Delta\mathbf{L}^{\mathrm{T}} - \mathbf{Q}_{\mathrm{a}} & -\Delta\mathbf{L}\boldsymbol{\Sigma}_{\mathrm{a}}\mathbf{L}^{\mathrm{T}} + \mathbf{Q}_{\mathrm{a}} \\ \mathbf{0} & -\mathbf{L}\boldsymbol{\Sigma}_{\mathrm{a}}\Delta\mathbf{L}^{\mathrm{T}} + \mathbf{Q}_{\mathrm{a}} & \bar{\mathbf{Q}}_k - \mathbf{Q}_{\mathrm{a}} \end{bmatrix}. \end{aligned} \tag{A.20}$$

where $\Delta\mathbf{L} \triangleq \hat{\mathbf{L}} - \mathbf{L}$. Since $\boldsymbol{\Delta}_0 \geq 0$ (as it is ensured in Sec. 5.2.3), $\boldsymbol{\Delta}_{k|k-1} \geq 0, \forall k \geq 1$ if the last matrix in Equation (A.20) is positive semidefinite. For the states of interest $\boldsymbol{\xi}$ we can assume that the process noise are designed such that $\hat{\mathbf{Q}}_{\xi,k} - \mathbf{Q}_{\xi,k} \geq 0$. Therefore, the desired condition is satisfied if the 2x2 lower-right block diagonal matrix in Equation (A.20) is positive semidefinite. Since the GMP are considered to be independent among each others, this is equivalent to satisfy for each GMP the following inequality:

$$\begin{bmatrix} \hat{q} - (\hat{\alpha} - \alpha)^2\bar{\sigma}^2 - q & -(\hat{\alpha} - \alpha)\alpha\bar{\sigma} + q \\ -(\hat{\alpha} - \alpha)\alpha\bar{\sigma} + q & \bar{q} - q \end{bmatrix} \geq 0. \tag{A.21}$$

where $\hat{q}$,$\hat{\alpha}$,α and $\bar{\sigma}^2$ are one of the diagonal elements of $\hat{\mathbf{Q}}_{\mathrm{a}}$,$\hat{\mathbf{L}}$,$\mathbf{L}$ and $\boldsymbol{\Sigma}_{\mathrm{a}}$ respectively. Equation (A.21) can be satisfied by ensuring the determinant is non-negative. Using $\bar{q} = \bar{\sigma}^2(1-\alpha^2)$, $q = \sigma^2(1-\alpha^2)$ and $\hat{q} = \hat{\sigma}^2(1-\hat{\alpha}^2)$, we lead to:

$$-(\alpha - \hat{\alpha})^2\bar{\sigma}^4 + (1-\alpha^2)(1-\hat{\alpha}^2)(\hat{\sigma}^2 - \sigma^2)\bar{\sigma}^2 - \hat{\sigma}^2\sigma^2(1-\alpha^2)(1-\hat{\alpha}^2) \geq 0. \tag{A.22}$$

Similar as in the continuous-time case (Section 4.3), we solve the quadratic expression in Equation (A.22) for $\bar{\sigma}^2$. The minimum imposed solution of $\bar{\sigma}^2$ that satisfies Equation (A.22) for the stationary model parameters in Equation (5.25) and Equation (5.26) is the one that provides only one root, which is achieved when $\sigma^2 = \sigma^2_{\max}$ is chosen and we use either $\alpha = \alpha_{\min}$ or $\alpha = \alpha_{\max}$. For $\alpha = \alpha_{\max}$, the minimum solution of $\bar{\sigma}^2$ (in discrete-time) is:

$$\bar{\sigma}^2_{\mathrm{d,min}} = \frac{(1-\hat{\alpha}_{\mathrm{d}}^2)(1-\alpha_{\max}^2)}{2(\hat{\alpha}_{\mathrm{d}} - \alpha_{\max})^2}(\hat{\sigma}^2_{\mathrm{d}} - \sigma^2_{\max}). \tag{A.23}$$

A.3 Proof of Continuous-time Parameters in Discrete-time Non-stationary Models

This appendix supports the proof that parameters derived in continuous-time can be used in non-stationary discrete-time models while still ensuring bounding conditions. This is achieved providing the proofs to Equation (5.59), which is here rewritten for convenience as:

$$\bar{\sigma}^2_{d,min}(\hat{\sigma}^2_c, \hat{\tau}_c) - \bar{\sigma}^2_{c,min} \geq 0, \forall \Delta t > 0. \tag{A.24}$$

On one side, $\bar{\sigma}^2_{c,min}$ was found in Section 4.3 to be:

$$\bar{\sigma}^2_{c,min} = 2\sigma^2_{max}\frac{\tau_{max}}{\tau_{max} - \hat{\tau}_c}. \tag{A.25}$$

In order to obtain $\bar{\sigma}^2_{d,min}(\hat{\sigma}^2_c, \hat{\tau}_c)$, we consider the main quadratic condition on $\bar{\sigma}^2$ in the discrete-time domain from Equation (A.22). As explained in Section 4.3 we are interested in the maximum of the quadratic Equation (A.22), which is:

$$\begin{aligned}\bar{\sigma}^2 = &\frac{(1-\alpha)(1-\hat{\alpha}^2)(\hat{\sigma}^2 - \sigma^2)}{2(\alpha - \hat{\alpha})^2} + \\ &\frac{\left\{(1-\alpha^2)(1-\hat{\alpha}^2)^2(\hat{\sigma}^2-\sigma^2)^2 - 4(\alpha-\hat{\alpha})^2\hat{\sigma}^2\sigma^2(1-\alpha^2)(1-\hat{\alpha}^2)\right\}^{1/2}}{2(\alpha-\hat{\alpha})^2}.\end{aligned} \tag{A.26}$$

In the case that $\hat{\alpha} = \hat{\alpha}_c$ (i.e., $\hat{\tau} = \hat{\tau}_c$) and $\hat{\sigma}^2 = \hat{\sigma}^2_c$, the term with the square root in Equation (A.26) is not zero in general, but it must be a positive value $\epsilon \geq 0$. Therefore $\bar{\sigma}^2_d(\hat{\sigma}^2_c, \hat{\tau}_c)$ can be written:

$$\bar{\sigma}^2_d(\hat{\sigma}^2_c, \hat{\tau}_c) = \frac{(1-\alpha)(1-\hat{\alpha}^2_c)(\hat{\sigma}^2_c - \sigma^2)}{2(\alpha - \hat{\alpha}_c)^2} + \epsilon, \tag{A.27}$$

which is on one side clearly minimum for $\sigma^2 = \sigma^2_{max}$ and it must be minimum at either $\alpha = \alpha_{min}$ or $\alpha = \alpha_{max}$. Substituting Equation (A.27) and Equation (A.25) into Equation (A.24) we lead to:

$$\frac{(1-\alpha)(1-\hat{\alpha}^2_c)(\hat{\sigma}^2_c - \sigma^2_{max})}{2(\alpha-\hat{\alpha}_c)^2} + \epsilon - 2\sigma^2_{max}\frac{\tau_{max}}{\tau_{max} - \hat{\tau}} \geq 0. \tag{A.28}$$

Substituting $\hat{\sigma}^2_c$ from Equation (4.41), taking σ^2_{max} as common factor and operating the two fractions in Equation (A.28) we lead to:

$$\sigma^2_{max}\left[\frac{(\tau_{max} - \hat{\tau}_c)(1-\alpha)(1-\hat{\alpha}^2_c)(\sqrt{\frac{\tau_{max}}{\tau_{min}}} - 1)}{2(\alpha-\hat{\alpha}_c)^2(\tau_{max} - \hat{\tau}_c)} - \frac{4\tau_{max}(\alpha-\hat{\alpha}_c)^2}{2(\alpha-\hat{\alpha}_c)^2(\tau_{max}-\hat{\tau}_c)}\right] + \epsilon \geq 0. \tag{A.29}$$

Since $\tau_{max} \geq \hat{\tau}_c$, the denominator is larger than zero and the condition in Equation (A.29) reduces to ensuring the numerator is larger or equal to zero. This is the case since 1. the

limit of the numerator for $\Delta t \to 0 = 0$ and 2. it is a monotonically increasing function of Δt independent on the actual value of τ. We can check that by checking the derivative of the numerator, which is:

$$\begin{aligned}&(\tau_{\max} - \hat{\tau}_c)(k_c - 1)\left[\frac{2(1 - e^{\frac{-\Delta_t}{\tau}})e^{\frac{-2\Delta_t}{\hat{\tau}_c}}}{\hat{\tau}_c} + \frac{e^{\frac{-\Delta_t}{\tau}}(1 - e^{\frac{-2\Delta_t}{\hat{\tau}_c}})}{\tau}\right] \\ &- 8\tau_{\max}\left(e^{\frac{-\Delta_t}{\tau}} - e^{\frac{-\Delta_t}{\hat{\tau}_c}}\right)\left(\frac{e^{\frac{-\Delta_t}{\hat{\tau}_c}}}{\hat{\tau}_c} - \frac{e^{\frac{-\Delta_t}{\tau}}}{\tau}\right) \geq 0.\end{aligned} \tag{A.30}$$

where $k_c = \sqrt{\frac{\tau_{\max}}{\tau_{\min}}}$ is used. Since $k_c \geq 1$ and all the negative exponentials exists between 0 and 1, the first argument in Equation (A.30) is always positive. The second argument led by a negative sign can be rewritten as:

$$-8\frac{\tau_{\max}}{\hat{\tau}_c \tau}\left(e^{\frac{-\Delta_t}{\tau}} - e^{\frac{-\Delta_t}{\hat{\tau}_c}}\right)e^{\frac{-\Delta_t}{\hat{\tau}_c}}e^{\frac{-\Delta_t}{\tau}}\left(\tau e^{\frac{\Delta_t}{\tau}} - \hat{\tau}_c e^{\frac{-\Delta_t}{\hat{\tau}_c}}\right) \geq 0. \tag{A.31}$$

If $\tau < \hat{\tau}_c$, $\left(e^{\frac{-\Delta_t}{\tau}} - e^{\frac{-\Delta_t}{\hat{\tau}_c}}\right) < 0$ and $\left(\tau e^{\frac{\Delta_t}{\tau}} - \hat{\tau}_c e^{\frac{-\Delta_t}{\hat{\tau}_c}}\right) > 0$, makes Equation (A.31) positive. If $\tau > \hat{\tau}_c$, $\left(e^{\frac{-\Delta_t}{\tau}} - e^{\frac{-\Delta_t}{\hat{\tau}_c}}\right) > 0$ and $\left(\tau e^{\frac{\Delta_t}{\tau}} - \hat{\tau}_c e^{\frac{-\Delta_t}{\hat{\tau}_c}}\right) < 0$, makes Equation (A.31) also positive. In the case that $\tau = \hat{\tau}_c$, Equation (A.31) is zero. This proofs that Equation (A.30) is non-negative, ultimately proving Equation (A.24).

A.4 Non-Stationary GMP Covariance over Time

This Appendix provides an expression for the autocovariance of a general non-stationary discrete-time GMP between two time steps. The first three samples of the discrete-time GMP sequence can be expressed with respect to the initial GMP sample a_0 as:

$$\begin{aligned}a_1 &= \alpha a_0 + \sqrt{\sigma^2(1-\alpha^2)}\,w_1, \\ a_2 &= \alpha^2 a_0 + \alpha\sqrt{\sigma^2(1-\alpha^2)}\,w_1 + \sqrt{\sigma^2(1-\alpha^2)}\,w_2, \\ a_3 &= \alpha^3 a_0 + \alpha^2\sqrt{\sigma^2(1-\alpha^2)}\,w_1 + \alpha\sqrt{\sigma^2(1-\alpha^2)}\,w_2 + \sqrt{\sigma^2(1-\alpha^2)}\,w_3, \\ &\vdots\end{aligned} \tag{A.32}$$

where

$$\alpha = e^{\frac{-\Delta_t}{\tau}}, \text{ and } w_i \sim \mathcal{N}(0,1),\ \forall i \in \mathbb{Z} > 0. \tag{A.33}$$

A general, compact form of these equations can be written for any time step n as:

$$a_n = \alpha^n a_0 + \sqrt{\sigma^2(1-\alpha^2)} \sum_{i=0}^{n-1} \alpha^i w_{n-i}. \tag{A.34}$$

Since the expected value of a GMP is zero for any time step ($\mathrm{E}[a_n] = 0,\ \forall n \geq 0$), the autocovariance of this non-stationary process between any integer $n \in \mathbb{Z}$ and $p \in \mathbb{Z}$ time step with $p \geq n$ is:

$$\mathrm{E}[a_n a_p] = \mathrm{E}\left[\left(\alpha^n a_0 + \sqrt{\sigma^2(1-\alpha^2)} \sum_{i=0}^{n-1} \alpha^i w_{n-i}\right)\left(\alpha^p a_0 + \sqrt{\sigma^2(1-\alpha^2)} \sum_{j=0}^{p-1} \alpha^j w_{p-j}\right)\right]. \tag{A.35}$$

Using $\mathrm{E}[a_0^2] = \sigma_0^2$ and $\mathrm{E}[a_0 w_i] = 0,\ \forall i \in \mathbb{Z} > 0$, and rearranging, Equation (A.35) becomes:

$$\mathrm{E}[a_n a_p] = \alpha^n \alpha^p \sigma_0^2 + \sigma^2(1-\alpha^2) \sum_{i=0}^{n-1} \sum_{j=0}^{p-1} \alpha^i \alpha^j \mathrm{E}[w_{n-i} w_{p-j}]. \tag{A.36}$$

Because the driving noise w_i is a white sequence, the expectation function under the double summation in Equation (A.36) is non-zero only if $n - i = p - j$, which is expressed as:

$$\begin{aligned} &\mathrm{E}[w_i w_i] = 1,\ \forall i > 0, \\ &\mathrm{E}[w_i w_j] = 0, \text{ for } i \neq j. \end{aligned} \tag{A.37}$$

Therefore we can make the change of variable: $j = p - n + i$ to get rid of one of the two summations:

$$\mathrm{E}[a_n a_p] = \alpha^n \alpha^p \sigma_0^2 + \sigma^2(1-\alpha^2) \sum_{i=0}^{n-1} \alpha^{2i+p-n}. \tag{A.38}$$

Recognizing a geometric series, Equation (A.38) becomes:

$$\mathrm{E}[a_n a_p] = \alpha^n \alpha^p \sigma_0^2 + \sigma^2(1-\alpha^2) \frac{(\alpha^{2n}-1)\alpha^{p-n}}{\alpha^2 - 1}, \tag{A.39}$$

which finally leads to:

$$\mathrm{E}[a_n a_p] = \alpha^{n+p} \sigma_0^2 + \sigma^2(1-\alpha^{2n})\alpha^{p-n},\ \forall p \geq n. \tag{A.40}$$

It is worth noting that if the process is stationary (i.e., $\sigma_0^2 = \sigma^2$), then Equation (A.40) expectedly reduces to:

$$\mathrm{E}[a_n a_p] = \sigma^2 \alpha^{p-n},\ \forall p \geq n. \tag{A.41}$$

The correlation between two time steps is the same regardless of the order of indices, that is: $\mathrm{E}[a_n a_p] = \mathrm{E}[a_p a_n]$. With this in mind, we can give an expression that does not specify which of n or p is larger:

$$\mathrm{E}[a_n a_p] = \alpha^{n+p}\sigma_0^2 + \sigma^2(1-\alpha^{2\min(n,p)})\alpha^{|p-n|}. \tag{A.42}$$

A.5 Approximate Non-Stationary Initial Variance Inflation Factor

In order to support the numerical search of k_0 in Equation (5.64), we can use the fact that the impact of k_0 on the positive semidefiniteness of $\Delta\mathbf{R}$ is most significant on the first leading principal minors. A first good approximation of $\tilde{k}_0$ can therefore be obtained by considering the first 2x2 leading principal submatrix. This is obtained by considering $\mathrm{N} = 2$, $n = 0$ and $p = 1$ in Equation (5.64), which reduces to [117]:

$$\sigma_{\max}^2 \begin{bmatrix} k_0 - 1 & \hat{\alpha}k_0 - \alpha \\ \hat{\alpha}k_0 - \alpha & \hat{\alpha}^2 k_0 + k\left(1-\hat{\alpha}^2\right) - 1 \end{bmatrix} \succeq 0, \tag{A.43}$$

This inequality leads to the following condition on $\tilde{k}_0$:

$$\tilde{k}_0 \geq \frac{k\left(1-\hat{\alpha}^2\right) - 1 + \alpha^2}{k\left(1-\hat{\alpha}^2\right) - 1 - \hat{\alpha}^2 + 2\alpha\hat{\alpha}}. \tag{A.44}$$

The right-hand side of Equation (A.44) is larger when $\tau = \tau_{\min}$ and therefore the most restrictive condition on $\tilde{k}_0$ is:

$$\tilde{k}_0 \geq \frac{k\left(1-e^{-\frac{2\Delta_t}{\hat{\tau}}}\right) - 1 + e^{-\frac{2\Delta_t}{\tau_{\min}}}}{k\left(1-e^{-\frac{2\Delta_t}{\hat{\tau}}}\right) - 1 - e^{-\frac{2\Delta_t}{\hat{\tau}}} + 2e^{-\Delta_t\left(\frac{1}{\hat{\tau}}+\frac{1}{\tau_{\min}}\right)}}. \tag{A.45}$$

The value in Equation (A.45) has been observed to be very close to the minimum condition on k_0 and it is therefore a good initialization value for the search of k_0. It is noteworthy in this discrete time expression that the minimum value of k_0 is dependent on the values and range of τ and on the sample interval Δt. The impact of Δt becomes significant when Δt approaches $\tau_{\min}$.

B Frequency Domain Bounding

B.1 Proof Frequency Domain Bounding in Continuous-Time

This appendix provides a proof to Theorem 4.2.1 for Kalman filter covariance bounding criteria based on frequency domain bounding in continuous-time domain. This proof follows the one provided in [51] and the reader is recommended to consult it for more details.

In general, since a Kalman filter is a linear estimator, any estimated state of interest can be expressed as a linear combination of the filter response to the independent inputs, which can be process, measurements or control inputs in general:

$$x(t) = x_1(t) + x_2(t) + \cdots + x_n(t). \tag{B.1}$$

where $x_i(t)$ is the filter response to process or measurement $i \in [1, n]$. Since the inputs to the KF are independent, the total variance of the error is also the sum of the individual error variances for each of the response to each input, assuming that errors in the inputs are zero-mean:

$$\sigma_x^2(t) = \sigma_{x,1}^2(t) + \sigma_{x,2}^2(t) + \cdots + \sigma_{x,n}^2(t). \tag{B.2}$$

We can then focus on the variance of each of the responses to each individual error component. The KF is in general a linear time varying (LTV) filter characterized with the impulse response $g_i(u,t)$. The response to a given error $z_i(t)$ can be expressed as the following convolution operation:

$$\epsilon_{x,i}(t) = \int_{-\infty}^{\infty} g_i(u,t) z_i(u) du. \tag{B.3}$$

This expression is a generalization to the well known convolution of linear time invariant systems. In here, it is important to interpret that for a given time moment, the frequency response of the filter would be different. The variance associated with an arbitrary $\epsilon_{x,i}(t)$ can

be computed as [53]:

$$\begin{aligned}\sigma_x^2(t) = \mathrm{E}[\epsilon_x(t)^2] = \mathrm{E}\left[\int_{-\infty}^{\infty} g(u,t)z(u)du \int_{-\infty}^{\infty} g(v,t)z(v)dv\right] = \\ \int_{-\infty}^{\infty}\int_{-\infty}^{\infty} g(u,t)g(v,t)\mathrm{E}[z(u)z(v)]dudv = \\ \int_{-\infty}^{\infty}\int_{-\infty}^{\infty} g(u,t)g(v,t)R_i(u-v)dudv,\end{aligned} \tag{B.4}$$

where the subscripts i are removed for clarity from this point on. R is the autocovariance of $z(t)$. The autocovariance is a Fourier pair with the Power Spectral Density (PSD), so we can write:

$$R(u-v) = \int_{-\infty}^{\infty} S(j\omega)e^{-j\omega(u-v)}d\omega \tag{B.5}$$

where $S(j\omega)$ is the PSD of the error $z(t)$. Rewriting Equation (B.4) depending on the PSD leads to:

$$\begin{aligned}\sigma_x^2(t) = \int_{-\infty}^{\infty} \mathrm{S}(j\omega)\int_{-\infty}^{\infty} g(u,t)e^{-j\omega u}du\int_{-\infty}^{\infty} g(v,t)e^{j\omega v}dvdf = \\ \int_{-\infty}^{\infty} G(j\omega,t)G(-j\omega,t)S(j\omega)d\omega = \int_{-\infty}^{\infty} |G(j\omega,t)|^2 S(j\omega)d\omega\end{aligned} \tag{B.6}$$

where $G(j\omega,t)$ is the time dependent frequency response associated to the KF. Let us now make the distinction between true KF error variance $\sigma_x^2(t)$ and the KF estimated error variance $\hat{\sigma}_x^2(t)$, where we want to satisfy the following bounding criteria:

$$\hat{\sigma}_x^2(t) \geq \sigma_x^2(t). \tag{B.7}$$

Substituting Equation (B.6) into Equation (B.7) results in:

$$\int_{-\infty}^{\infty} |G(j\omega,t)|^2 \hat{S}(j\omega)d\omega \geq \int_{-\infty}^{\infty} |G(j\omega,t)|^2 S(j\omega)d\omega, \tag{B.8}$$

where $\hat{S}(\omega)$ is the modeled PSD associated with $\hat{\sigma}_x(t)^2$ and $S(\omega)$ is the actual PSD that would produce $\sigma_x(t)^2$. Since the transfer function is the same on both sides of Equation (B.8), it is clear that $\hat{\sigma}_x^2(t) \geq \sigma_x^2(t)$ if $\hat{S}(\omega) \geq S(\omega)$, $\forall\omega \in [-\infty,\infty]$.

B.2 Proof Frequency Domain Bounding in Discrete-Time

Section 5.1.1 established that in discrete-time the actual KF error can be bounded when designing each of the process and measurement error such their modeled autocovariance matrices bound in a positive semidefinite sense the actual process autocovariance matrix, i.e., $\hat{\mathbf{R}} \geq \mathbf{R}$. This appendix provides the proof in discrete time that the $\hat{\mathbf{R}} \geq \mathbf{R}$ criteria can be satisfied

for discrete-time systems if a similar criteria in the power spectral density domain is satisfied, i.e., $\hat{S}(\omega) \geq S(\omega)$ as introduced in Theorem 5.1.1.

The autocovariance matrix (ACM) of a stationary random process is a symmetric positive semidefinite matrix with Toeplitz structure of the form [99]:

$$\mathbf{R} = \begin{bmatrix} r[0] & r[1] & \cdots & r[i] & \cdots \\ r[1] & r[0] & r[1] & \cdots & r[i] \\ \cdots & r[1] & r[0] & r[1] & \cdots \\ r[i] & \cdots & r[1] & r[0] & r[1] \\ \cdots & r[i] & \cdots & r[1] & r[0] \end{bmatrix}, \tag{B.9}$$

where here i is a certain time lag. The information in a autocovariance matrix like Equation (B.9) can be therefore also summarized by a positive sequence $\{r_l\}$ of size l, generating an ACM of size $l \times l$. The condition $\hat{\mathbf{R}} \geq \mathbf{R}$, which can be alternatively written as the difference of both matrices being positive semidefinite (i.e., $\hat{\mathbf{R}} - \mathbf{R} \geq \mathbf{0}$), can be therefore equivalently expressed as $\{\hat{r}_l\} - \{r_l\} = \{\hat{r}_l - r_l\}$ being a positive sequence [118]. On the other hand, a sequence that is absolute summable (i.e.,: $\sum_l |r_l| \leq \infty$) is said to be positive if and only if its Fourier transform is a non-negative function [118]. The Fourier transform of the autocovariance sequence of a noise is its power spectral density, which can be obtained from the sequence as:

$$S(\omega) = \sum_{l=-\infty}^{\infty} r_l e^{-j\omega l} \geq 0, \ \ \forall \omega \in [0, \pi] \tag{B.10}$$

If $\{\hat{r}_l\} - \{r_l\} = \{\hat{r}_l - r_l\}$ is a positive sequence, then its Fourier transform must satisfy:

$$\sum_{l=-\infty}^{\infty} (\hat{r}_l - r_l) e^{-j\omega l} \geq 0, \ \ \forall \omega \in [0, \pi], \tag{B.11}$$

which can be developed as:

$$\sum_{l=-\infty}^{\infty} \hat{r}_l e^{-j\omega l} - \sum_{l=-\infty}^{\infty} r_l e^{-j\omega l} \geq 0, \ \ \forall \omega \in [0, \pi], \tag{B.12}$$

$$\hat{S}(\omega) - S(\omega) \geq 0, \ \ \forall \omega \in [0, \pi]. \tag{B.13}$$

This suggests that overbounding the power spectral density of the true process for all frequencies guarantees bounding conditions (positive semidefinite) at the autocovariance level. For the discussion of the effect of windowing on the autocovariance sequence the reader can consult [99].

C GNSS/INS Kalman Filter

C.1 Strapdown INS Algorithm

In order to compute attitude, velocity and position the mechanization differential expressions in Equation (2.19) must be implemented based on sampled inertial measurements (i.e., angular velocities and specific forces) over time. This implementation is known as *strapdown algorithm*.

Inertial Navigation Systems (INS) or Inertial Reference Systems (IRS) provide attitude, velocity and position over time with respect to an reference initial value of those magnitudes. The first step is therefore to initialize it. Avionics systems perform this initialization typically at the gate when the aircraft is static (or semi-static) [5]. This is done on one side by sensing the gravity vector in the accelerometers to determine roll and pitch angles. On the other side, the gyroscope can sense the Earth rotation to estimate the heading. Velocity can be easily initialized to zero in static conditions and position is typically obtained from other sensors, like GNSS [28]. Other types of initialization, for example, by transfer alignment are possible and are described in the literature. For lower grade sensors this initialization is normally followed by a fine alignment process with Kalman filtering while the vehicle is still static [28]. Based on an initialization of the INS system, the algorithm updates with new IMU measurements the attitude, velocity and position over time. The next sections provides the details of one strapdown reference algorithm.

C.1.1 Attitude

The attitude computer updates the direction cosine matrix (DCM) representing the rotation from the body to the navigation frame $\mathbf{C}_b^n$ by applying rotations representing the changes

suffered of each frames from time $k-1$ to time k:

$$\mathbf{C}_{b,k}^{n,k} = \mathbf{C}_{n,k-1}^{n,k}\mathbf{C}_{b,k-1}^{n,k-1}\mathbf{C}_{b,k-1}^{b,k}, \tag{C.1}$$

where the navigation and body time update rotations can be analytically computed with:

$$\mathbf{C}_{b,k-1}^{b,k} = \mathbf{I} + \frac{\sin(\|\boldsymbol{o}\|)}{\|\boldsymbol{o}\|}[\boldsymbol{o}\times] + \frac{1-\cos(\|\boldsymbol{o}\|)}{\|\boldsymbol{o}\|^2}[\|\boldsymbol{o}\|\times]^2, \tag{C.2}$$

$$\mathbf{C}_{n,k-1}^{n,k} = \mathbf{I} + \frac{\sin(\|\boldsymbol{\vartheta}\|)}{\|\boldsymbol{\vartheta}\|}[\boldsymbol{\vartheta}\times] + \frac{1-\cos(\|\boldsymbol{\vartheta}\|)}{\|\boldsymbol{\vartheta}\|^2}[\|\boldsymbol{\vartheta}\|\times]^2. \tag{C.3}$$

The sampled angular velocity $\boldsymbol{o} = \omega_{ib}^{b}\Delta t$ is taken from the gyroscope measurement and $\boldsymbol{\vartheta} = \omega_{in}^{n}\Delta t$ contains the sampled angular velocity due to Earth rotation and transport rate in the local navigation frame $\boldsymbol{\omega}_{in}^{n} = \boldsymbol{\omega}_{ie}^{n} + \boldsymbol{\omega}_{en}^{n}$. The angular velocity in the local frame due to Earth rotation is:

$$\boldsymbol{\omega}_{ie}^{n} = \begin{bmatrix} \omega_{ie}\cos(\varphi) \\ 0 \\ -\omega_{ie}\sin(\varphi) \end{bmatrix}. \tag{C.4}$$

The transport rate in the local navigation frame is:

$$\boldsymbol{\omega}_{en}^{n} = \begin{bmatrix} \frac{v_{\mathrm{E}}}{(\mathrm{R_E}+h)} \\ \frac{-v_{\mathrm{N}}}{(\mathrm{R_N}+h)} \\ \frac{-v_{\mathrm{E}}\tan(\varphi)}{(\mathrm{R_E}+h)} \end{bmatrix}. \tag{C.5}$$

C.1.2 Velocity

Velocity is updated at every time epoch is applied with:

$$\mathbf{v}_k^n \approx \mathbf{v}_{k-1}^n + \left[\mathbf{C}_{b,k}^{n,k}\mathbf{f}_k^b + \mathbf{g}_{k-1}^n + (2\boldsymbol{\Omega}_{ie,k-1}^n + \boldsymbol{\Omega}_{en,k-1}^n)\mathbf{v}_{k-1}^n\right]\Delta t, \tag{C.6}$$

where $\mathbf{f}^b$ is the specific force measurement in the body frame, and $\mathbf{g}_{k-1}^n \approx \begin{bmatrix} 0 & 0 & g(\varphi,h) \end{bmatrix}^{\mathrm{T}}$ removes the gravity acceleration in the local frame from the specific forces. Widely used gravity models for $g(\varphi,h)$ depending on latitude and altitude can be found in [27], [28]. For instance [27] models the gravity magnitude with:

$$g(\varphi,h) = g(0) + \frac{dg(0)}{dh}h, \tag{C.7}$$

where the gravity magnitude at the surface $g(0)$ in $[\mathrm{m\,s^{-2}}]$ is:

$$g(0) = 9.780318(1 + 5.3024\mathrm{E}-3\sin^2(\varphi) - 5.9\mathrm{E}-6\sin^2(2\varphi)), \tag{C.8}$$

and the variation with altitude in $[\mathrm{m/s^2/m}]$ is given by:

$$\frac{dg(0)}{dh} = -0.0000030877(1 - 1.39\mathrm{E}-3\sin^2(\varphi)). \tag{C.9}$$

The last term in the parentheses in Equation (C.6) accounts fro the Earth rotation and the change of local frame with velocity (known as transport rate). The matrix $\boldsymbol{\Omega}^n_{ie,k-1} = [\boldsymbol{\omega}^n_{ie}\times]$ is the skewsymmetric matrix of the Earth rotation in the local navigation frame. And the transport rate term is $\boldsymbol{\Omega}^n_{en,k-1} = [\boldsymbol{\omega}^n_{en}\times]$.

C.1.3 Position

The latitude (φ), longitude (λ) and altitude (h) curvilinear position can be updated in three steps in the following order:

$$h_k = h_{k-1} - \frac{v_{\mathrm{D},k} + v_{\mathrm{D},k-1}}{2}\Delta t \tag{C.10}$$

$$\varphi_k = \varphi_{k-1} + \left(\frac{v_{\mathrm{N},k}}{\mathrm{R}_{\mathrm{N},k} + h_k} + \frac{v_{\mathrm{N},k-1}}{\mathrm{R}_{\mathrm{N},k-1} + h_{k-1}}\right)\frac{\Delta t}{2} \tag{C.11}$$

$$\lambda_k = \lambda_{k-1} + \left(\frac{v_{\mathrm{E},k}}{\left(\mathrm{R}_{\mathrm{E},k} + h_k\right)\cos(\varphi_k)} + \frac{v_{\mathrm{E},k-1}}{\left(\mathrm{R}_{\mathrm{E},k-1} + h_{k-1}\right)\cos(\varphi_{k-1})}\right)\frac{\Delta t}{2} \tag{C.12}$$

A more precise integration can be achieved via Runge-kutta integration. For the purpose of this research and the simulations in Chapter 7 the trapezoidal rule here applied was sufficient.

C.2 Inertial-related KF matrices

This Appendix details the relevant inertial-related matrices in the GNSS/INS Kalman filter used in the design of Chapter 6. The prediction matrix $\mathbf{F}_{\mathrm{INS}}$ is modeled in the following way for a local level navigation frame:

$$\mathbf{F}^n_{\mathrm{INS}} = \begin{bmatrix} \mathbf{F}^n_{\psi\psi} & \mathbf{F}^n_{\psi v} & \mathbf{F}^n_{\psi p} & \mathbf{0} & \hat{\mathbf{C}}^n_b \\ \mathbf{F}^n_{v\psi} & \mathbf{F}^n_{vv} & \mathbf{F}^n_{vp} & \hat{\mathbf{C}}^n_b & \mathbf{0} \\ \mathbf{0} & \mathbf{F}^n_{pv} & \mathbf{F}^n_{pp} & \mathbf{0} & \mathbf{0} \\ \mathbf{0} & \mathbf{0} & \mathbf{0} & \mathbf{0} & \mathbf{0} \\ \mathbf{0} & \mathbf{0} & \mathbf{0} & \mathbf{0} & \mathbf{0} \end{bmatrix}. \tag{C.13}$$

For linearized KF and Extended Kalman filter, the discrete transition matrix is:

$$\boldsymbol{\Phi}^n_{\text{INS}} \approx \begin{bmatrix} \mathbf{I}+\mathbf{F}^n_{\psi\psi}\Delta t & \mathbf{F}^n_{\psi v}\Delta t & \mathbf{F}^n_{\psi p}\Delta t & \mathbf{0} & \hat{\mathbf{C}}^n_b\Delta t \\ \mathbf{F}^n_{v\psi}\Delta t & \mathbf{I}_3+\mathbf{F}^n_{vv}\Delta t & \mathbf{F}^n_{vp}\Delta t & \hat{\mathbf{C}}^n_b\Delta t & \mathbf{0} \\ \mathbf{0} & \mathbf{F}^n_{pv}\Delta t & \mathbf{I}+\mathbf{F}^n_{pp}\Delta t & \mathbf{0} & \mathbf{0} \\ \mathbf{0} & \mathbf{0} & \mathbf{0} & \mathbf{I}e^{-\frac{\Delta_t}{\tau_f}} & \mathbf{0} \\ \mathbf{0} & \mathbf{0} & \mathbf{0} & \mathbf{0} & \mathbf{I}e^{-\frac{\Delta_t}{\tau_\omega}} \end{bmatrix}. \tag{C.14}$$

The process noise projection matrix **G** is:

$$\mathbf{G} = \begin{bmatrix} \mathbf{0} & \hat{\mathbf{C}}^n_b & \mathbf{0} & \mathbf{0} \\ \hat{\mathbf{C}}^n_b & \mathbf{0} & \mathbf{0} & \mathbf{0} \\ \mathbf{0} & \mathbf{0} & \mathbf{0} & \mathbf{0} \\ \mathbf{0} & \mathbf{0} & \mathbf{I} & \mathbf{0} \\ \mathbf{0} & \mathbf{0} & \mathbf{0} & \mathbf{I} \end{bmatrix} \tag{C.15}$$

Each of the block matrices in Equation (C.13) are detailed in the following. Each of these matrices, named by $\mathbf{F}^n_{ij}$, represents how the error j propagates into the i one. These subscripts can be ψ (attitude error), v (velocity error) or p (position error).

$$\mathbf{F}^n_{\psi\psi} = -\left[\omega^n_{in}\times\right] \tag{C.16}$$

$$\mathbf{F}^n_{\psi v} = \begin{bmatrix} 0 & \frac{-1}{\mathrm{R_E}+h} & 0 \\ \frac{1}{\mathrm{R_N}+h} & 0 & 0 \\ 0 & \frac{\tan\varphi}{\mathrm{R_E}+h} & 0 \end{bmatrix} \tag{C.17}$$

$$\mathbf{F}^n_{\psi p} = \begin{bmatrix} \omega_{ie}\sin\varphi & 0 & \frac{v_{\mathrm{E}}}{(\mathrm{R_E}+h)^2} \\ 0 & 0 & \frac{-v_{\mathrm{N}}}{(\mathrm{R_N}+h)^2} \\ \omega_{ie}\cos\varphi + \frac{v_{\mathrm{E}}}{(\mathrm{R_E}+h)\cos^2\varphi} & 0 & \frac{-v_{\mathrm{E}}\tan\varphi}{(\mathrm{R_N}+h)^2} \end{bmatrix} \tag{C.18}$$

$$\mathbf{F}_{v\psi}^{n} = -\left[\left(\mathbf{C}_{b}^{n}\mathbf{f}^{b}\right)\times\right] \tag{C.19}$$

$$\mathbf{F}_{vv}^{n} = \begin{bmatrix} \dfrac{v_{\mathrm{D}}}{\mathrm{R_N}+h} & -\dfrac{2v_{\mathrm{E}}\tan\varphi}{\mathrm{R_E}+h} - 2\omega_{ie}\sin\varphi & \dfrac{v_{\mathrm{N}}}{\mathrm{R_N}+h} \\ \dfrac{v_{\mathrm{E}}\tan\varphi}{\mathrm{R_E}+h} + 2\omega_{ie}\sin\varphi & \dfrac{v_{\mathrm{N}}\tan\varphi + v_{\mathrm{D}}}{\mathrm{R_E}+h} & \dfrac{v_{\mathrm{E}}}{\mathrm{R_E}+h} + 2\omega_{ie}\cos\varphi \\ -\dfrac{2v_{\mathrm{N}}}{\mathrm{R_N}+h} & -\dfrac{2v_{\mathrm{E}}}{\mathrm{R_E}+h} - 2\omega_{ie}\cos\varphi & 0 \end{bmatrix} \tag{C.20}$$

$$\mathbf{F}_{vp}^{n} = \begin{bmatrix} -\dfrac{\left(v_{\mathrm{E}}\sec\varphi\right)^2}{\mathrm{R_E}+h} - 2v_{\mathrm{E}}\omega_{ie}\cos\varphi & 0 & \dfrac{(v_{\mathrm{E}})^2\tan\varphi}{(\mathrm{R_E}+h)^2} - \dfrac{v_{\mathrm{N}}v_{\mathrm{D}}}{(\mathrm{R_N}+h)^2} \\ \begin{pmatrix} \dfrac{v_{\mathrm{N}}v_{\mathrm{E}}\sec^2\varphi}{\mathrm{R_E}+h} + 2v_{\mathrm{N}}\omega_{ie}\cos\varphi \\ -2v_{\mathrm{D}}\omega_{ie}\sin\varphi \end{pmatrix} & 0 & -\dfrac{v_{\mathrm{N}}v_{\mathrm{E}}\tan\varphi + v_{\mathrm{E}}v_{\mathrm{D}}}{(\mathrm{R_E}+h)^2} \\ 2v_{\mathrm{D}}\omega_{ie}\sin\varphi & 0 & \dfrac{(v_{\mathrm{E}})^2}{(\mathrm{R_E}+h)^2} + \dfrac{(v_{\mathrm{N}})^2}{(\mathrm{R_N}+h)^2} - \dfrac{2g_0}{r_{e\mathrm{S}}^{e}} \end{bmatrix} \tag{C.21}$$

where $r_{e\mathrm{S}}^{e}$ is the geocentric radius at the surface, given by:

$$r_{e\mathrm{S}}^{e}(\varphi) = \mathrm{R_E}\sqrt{\cos^2\varphi + \left(1-e^2\right)^2\sin^2\varphi} \tag{C.22}$$

$$\mathbf{F}_{pv}^{n} = \mathbf{D} \text{ (See Equation (2.20))} \tag{C.23}$$

$$\mathbf{F}_{pp}^{n} = \begin{bmatrix} 0 & 0 & -\dfrac{v_{\mathrm{N}}}{(\mathrm{R_N}+h)^2} \\ \dfrac{v_{\mathrm{E}}\sin\varphi}{(\mathrm{R_E}+h)\cos^2\varphi} & 0 & -\dfrac{v_{\mathrm{E}}}{(\mathrm{R_E}+h)^2\cos\varphi} \\ 0 & 0 & 0 \end{bmatrix} \tag{C.24}$$

(C.25)

D Multiple Hypothesis Solution Separation Algorithm

This appendix details some aspects of the Multiple Hypothesis Solution Separation (MHSS) algorithm used for the ARAIM and GNSS/INS integrity monitoring design and evaluation in Chapter 6 and 7.

D.1 Determination of Monitored Fault Modes

The faults that need to be monitored have to be computed based on the information of the ISM message, in terms of the prior probabilities of satellites and constellation faults. This determination is performed such that the sum of the probabilities of the fault modes that are not monitored do not exceed a certain probability threshold (P_{THRES}), which is typically a residual portion of the total integrity budget. This can be expressed in terms of the probabilities of the monitored faults as [112]:

$$\sum_{h \text{ monitored}} P_{fault,h} \geq 1 - P_{THRES}, \tag{D.1}$$

where $P_{fault,h}$ is the probability of a certain fault hypothesis h. The fault modes subsets that need to be considered are determined by first calculating the maximum number of simultaneous faults (either satellite or constellation) that need to be monitored, this can be defined as:

$$N_{fault,max} = \underset{r \in 1,...,N_{sat}}{\arg\max}\ P_{multiple}\left(r+1, P_{event,1}, ..., P_{event,N_{sat}+N_{const}}\right). \tag{D.2}$$

Based on $N_{fault,max}$ the different subsets with different indexes can be formed for each of the fault hypothesis that need to be monitored.

D.2 Simulation Environment

The evaluations related to the baseline ARAIM MHSS algorithm has been carried out based on the MATLAB Algorithm Availability Simulation Tool (MAAST), developed by the Stanford University GPS Lab [109]. This tool has been adapted to accept specific trajectories that have been generated by the DLR multisensor simulator [110].

For the GNSS/INS and MHSS algorithm based on a bank of Kalman filters new code has been created for this research. In order to create comparative results with ARAIM, the same parameters configuration has been used as the baseline ARAIM algorithm. Some features and functions from MAAST have also been used or adapted. In particular for the computation of fault modes (`determine_subsets_v4.m`), and protection level calculation (`compute_protection_level_v4.m`).

List of Publications

Main Journal and Conference Papers

Some results have already been published or prepared for publication and are directly related to this thesis:

- ***O. Garcia Crespillo**, S. Langel and M. Joerger, "Tight Bounds for Uncertain Time-Correlated Errors with Gauss-Markov Structure in Kalman Filtering", unpublished.* [119]
  - This publication contains the main results and proofs of Chapter 4 and Chapter 5.
- *Langel, Steven and **Garcia Crespillo, Omar** and Joerger, Mathieu (2021) Overbounding the effect of uncertain Gauss-Markov noise in Kalman filtering. Navigation, Journal of the Institute of Navigation, pp. 1-18. Wiley. doi: 10.1002/navi.419. ISSN 0028-1522* [73]
  - This publication presents the basis for the problem statement and advanced sensitivity analysis of Chapter 4 and Chapter 5.
- ***O. Garcia Crespillo**, M. Joerger, and S. Langel, "Tight bounds for uncertain time-correlated errors with gauss-markov structure",arXiv, 2020.* [117]
  - This publication is a pre-print with the stationary GMP model parameter results of Chapter 4.
- ***Garcia Crespillo, Omar** and Joerger, Mathieu and Langel, Steve (2020) Overbounding GNSS/INS Integration with Uncertain GNSS Gauss-Markov Error Parameters. 2020 IEEE/ION Position, Location and Navigation Symposium (PLANS), Portland, OR, USA.* [105]
  - This publication sets the design presented in Chapter 6 and some initial partial results.
- *Langel, Steve and **Garcia Crespillo, Omar** and Joerger, Mathieu (2020) A New Approach for Modeling Correlated Gaussian Errors using Frequency Domain Overbounding. 2020 IEEE/ION Position, Location and Navigation Symposium (PLANS), Portland, OR, USA.* [99]

  - This publication formalizes the frequency domain bounding methodology that is used in Chapter 4 and Chapter 5.

- *Langel, Steve and **Garcia Crespillo, Omar** and Joerger, Mathieu (2019) Bounding Sequential Estimation Errors due to Gauss-Markov Noise with Uncertain Parameters. Proceedings of the 32nd International Technical Meeting of the Satellite Division of The Institute of Navigation (ION GNSS+ 2019), September 16 - 20, 2019, Miami, FL, USA.* [100]

  - This publication is the first version of the latter published journal containing the conservative bound in Chapter 4 and an early version of the sensitivity analysis methodology.

Other Related Publications

Other publications that have supported directly or indirectly the research of this thesis are:

- ***Garcia Crespillo, Omar** and Grosch, Anja and Belabbas, Boubeker and Rippl, Markus (2014) GNSS-aided INS Integrity Concept. ION GNSS+ 2014, Tampa, Florida (US)* [31]

- ***O. García Crespillo**, A. Grosch, J. Skaloud, and M. Meurer, Innovation vs Residual KF Based GNSS/INS Autonomous Integrity Monitoring in Single Fault Scenario", in ION GNSS+ 2017, Portland, OR, USA, Sep. 2017* [37]

- *A. Grosch, **O. G. Crespillo**, I. Martini, and C. Günther, Snapshot residual and kalman filter based fault detection and exclusion schemes for robust railway navigation", in 2017 European Navigation Conference (ENC), May 2017* [19]

- ***Garcia Crespillo, Omar** and Medina, Daniel and Skaloud, Jan and Meurer, Michael (2018) Tightly Coupled GNSS/INS Integration based on Robust M-Estimators. ION/IEEE PLANS 2018, Monterey, CA* [120]

- ***Garcia Crespillo, Omar** and Arias Medina, Daniel and Grosch, Anja and Skaloud, Jan and Meurer, Michael (2017) Robust Tightly Coupled GNSS/INS Estimation for Navigation in Challenging Scenarios. GPS World, 28 (8). GPS World* [121]

- ***Garcia Crespillo, Omar** and Grosch, Anja and Meurer, Michael (2017) Detection of DME Ranging Faults with INS Coupling. In: Integrated Communications, Navigation and Surveillance Conference, ICNS. 2017 Integrated Communication, Navigation and Surveillance Conference (ICNS), Herdon, VA, USA* [106]

- *Langel, Steven and **Garcia Crespillo, Omar** and Joerger, Mathieu (2020) Overbounding Sequential Estimation Errors Due to Non-Gaussian Correlated Noise. Proceedings of*

the 33rd International Technical Meeting of the Satellite Division of The Institute of Navigation (ION GNSS+ 2020), Virtual [116]

Supervised Master Thesis and Internships

- P. Abel, *Multisensor Navigation Simulator*, Karlsruhe Institute of Technology (KIT), *Internship*, 2016.
- S. Ciuban, *Autonomous Integrity Monitoring of Tightly Coupled PPP/INS*, Ecole Nationale de l'Aviation Civile (ENAC), *Master Thesis*, 2017.
- A. Andreetti, *Robust Estimators with Multi-Constellation for Positioning in Urban Scenarios*, Ecole Polytechnic Federal de Lausanne (EPFL), *Internship*, 2019
- M. Simonetti, *Modeling of Barometric Altimeter Measurements to Support Geodetic Altitude Navigation*, Technical University of Munich (TUM), *Master Thesis*, 2021.
- P. Mateos Ruiz, *Real-time INS/GNSS Integration of low-cost IMU and Multi-element Antenna Array Receiver*, University of Malaga, *Master Thesis*, 2021.
- J.C. Ruiz Sicilia, *A Machine Learning based NLOS Detector for Robust GNSS Positioning in Urban Environments*, University of Malaga, *Master Thesis*, 2021.

Bibliography

[1] ICAO SARPS, *Annex 10 to the Convention on International Civil Aviation: Aeronautical Telecommunications, Volume i: Radio Navigation Aids*, ICAO, Jul. 2006.

[2] *ICAO Doc 9613, performance based navigation manual, consoldated 4th edition, 2013*.

[3] GSA, "Report on Aviation User Needs and Requirements", European Global Navigation Satellite System Agency, Tech. Rep. GSA-MKD-AV-UREQ-250287, Dec. 2019.

[4] J. Blanch, T. Walker, P. Enge, *et al.*, "Baseline advanced raim user algorithm and possible improvements", *IEEE Transactions on Aerospace and Electronic Systems*, vol. 51, no. 1, pp. 713–732, 2015. DOI: 10.1109/TAES.2014.130739.

[5] RTCA, "Do-334: minimum operational performance standards (mops) for strapdown attitude and heading reference systems (ahrs)", Radio Technical Commission for Aeronautics, Tech. Rep., 2012.

[6] RTCA, "Minimum Operational Performance Standards for Global Positioning System/Aircraft Base Augmentation System", SC-159, Tech. Rep. DO-316, 2009.

[7] RTCA/SC-159, "RTCA/DO-229D Semi-Final: Minimum Operational Performance Standards for Global Positioning System/Wide Area Augmentation System Airborne Equipment", RTCA, Tech. Rep., 2006.

[8] RTCA, "DO-384 Minimum operational performance standards (MOPS) for GNSS aided inertial systems", Radio Technical Commission for Aeronautics, Tech. Rep. DO384, 2020.

[9] EUROCAE, "Ed-259 - minimum operational performance standard for galileo / global positioning system / satellite-based augmentation system airborne equipment", Tech. Rep., 2019.

[10] *Radio regulations. Chapter II - Frequencies, Article 5 Frequency allocation*, ITU.

[11] J. A. Klobuchar, "Ionospheric time-delay algorithm for single-frequency gps users", *IEEE Transactions on Aerospace and Electronic Systems*, vol. AES-23, no. 3, pp. 325–331, 1987. DOI: 10.1109/TAES.1987.310829.

[12] G. Di Giovanni and S. Radicella, "An analytical model of the electron density profile in the ionosphere", *Advances in Space Research*, vol. 10, no. 11, pp. 27–30, 1990.

[13] B. Arbesser-Rastburg, "The galileo single frequency ionospheric correction algorithm", *Third European Space Weather Week*, vol. 13, p. 17, 2006.

[14] J. S. Subirana, M. Hernandez-Pajares, and J. e Miguel Juan Zornoza, *GNSS Data Processing: Fundamentals and Algorithms*. European space agency, 2013.

[15] R. Hatch, "The synergism of gps code and carrier measurements", in *International geodetic symposium on satellite doppler positioning*, vol. 2, 1983, pp. 1213–1231.

[16] Parkinson and Spilker, *Global Positioning System: Theory and Applications*. American Institute of Aeronautics and Astronautics, 1996.

[17] T. Walter and P. Enge, "Weighted RAIM for Precision Approach", in *Proceedins of the ION GPS*, Institute of Navigation, 1995, pp. 1995–2004.

[18] RTCA/SC-159, "RTCA/DO-229C: Minimum Operational Performance Standards for Global Positioning System/Wide Area Augmenation System Airborne Equipment", RTCA, Tech. Rep., 2001.

[19] A. Grosch, O. G. Crespillo, I. Martini, and C. Günther, "Snapshot residual and kalman filter based fault detection and exclusion schemes for robust railway navigation", in *2017 European Navigation Conference (ENC)*, May 2017, pp. 36–47. DOI: 10.1109/EURONAV.2017.7954171.

[20] FAA, *World-wide availability*, https://www.nstb.tc.faa.gov/.

[21] Working Group C - ARAIM Subgroup, "Milestone 3 Report", EU/US Cooperation on Satellite Navigation, Tech. Rep., 2016.

[22] S. Perea, M. Meurer, M. Rippl, B. Belabbas, and M. Joerger, "Ura/sisa analysis for gps and galileo to support araim", *NAVIGATION, Journal of the Institute of Navigation*, vol. 64, no. 2, pp. 237–254, 2017.

[23] S. Perea, M. Meurer, and B. Pervan, "Design of an integrity support message for offline advanced raim", Ph.D. dissertation, PhD Dissertation, May, 2019.

[24] M. Simonetti and O. Garcia Crespillo, "Robust modeling of geodetic altitude from barometric altimeter and weather data", in *Proceedings of the 34th International Technical Meeting of the Satellite Division of The Institute of Navigation (ION GNSS+ 2021)*, 2021.

[25] P. G. Savage, "Strapdown Inertial Navigation System Integration Algorithm Design Part 1 - Attitude Algorithms", *AIAA Journal of Guidance, Control, and Dynamics*, vol. 21, pp. 19–28, Jan. 1998.

[26] P. G. Savage, "Strapdown Inertial Navigation System Integration Algorithm Design Part 2 - Velocity and Position Algorithms", *AIAA Journal of Guidance, Control, and Dynamics*, vol. 21, no. 2, pp. 208–221, Mar. 1998.

[27] D. Titterton and J. Weston, *Strapdown Inertial Navigation Technology, 2nd ed.* Institution of Electrical Engineers, 2004.

[28] P. D. Groves, *Principles of GNSS, Inertial, and Multisensor Integrated Navigation Systems*, Second. Artech House, 2013.

[29] O. Garcia Crespillo, E. Nossek, A. Winterstein, B. Belabbas, and M. Meurer, "Use of High Altitude Platform Systems to Augment Ground Based APNT Systems", in *Proceedings of the 34th Digital Avionics Systems Conference (DASC)*, Sep. 2015.

[30] I. Moir, A. Seabridge, and M. Jukes, *Civil Avionics Systems*, 2nd ed., J. C. Peter Belobaba and A. Seabridge, Eds. John Wiley & Sons, Ltd, 2013.

[31] O. Garcia Crespillo, A. Grosch, B. Belabbas, and M. Rippl, "GNSS-aided INS Integrity Concept", in *ION GNSS+*, Institute of Navigation (ION), Tampa, Florida (US), 2014.

[32] C. Call, M. Ibis, J. McDonald, and K. Vanderwerf, "Performance of Honeywell's Inertial/GPS Hybrid (HIGH) for RNP Operations", in *Position, Location, And Navigation Symposium (PLANS)*, IEEE/ION, Ed., 2006.

[33] A. Gelb and T. A. S. Corporation, *Applied Optimal Estimation*. The MIT Press, 1974, ISBN: 0262570483.

[34] V. Madyastha, V. Ravindra, S. Mallikarjunan, and A. Goyal, "Extended kalman filter vs. error state kalman filter for aircraft attitude estimation", in *AIAA Guidance, Navigation, and Control Conference*, 2011. DOI: 10.2514/6.2011-6615. eprint: https://arc.aiaa.org/doi/pdf/10.2514/6.2011-6615. [Online]. Available: https://arc.aiaa.org/doi/abs/10.2514/6.2011-6615.

[35] Ç. Tanıl, S. Khanafseh, M. Joerger, and B. Pervan, "An ins monitor to detect gnss spoofers capable of tracking vehicle position", *IEEE Transactions on Aerospace and Electronic Systems*, vol. 54, no. 1, pp. 131–143, 2018. DOI: 10.1109/TAES.2017.2739924.

[36] Ç. Tanıl, S. Khanafseh, M. Joerger, and B. Pervan, "Sequential Integrity Monitoring for Kalman Filter Innovations-based Detectors", in *Proceedings of the 31st International Technical Meeting of the Satellite Division of The Institute of Navigation (ION GNSS+ 2018)*, Sep. 2018.

[37] O. García Crespillo, A. Grosch, J. Skaloud, and M. Meurer, "Innovation vs Residual KF Based GNSS/INS Autonomous Integrity Monitoring in Single Fault Scenario", in *ION GNSS+ 2017*, Portland, OR, USA, Sep. 2017.

[38] U. Bhatti and W. Ochieng, "Detecting multiple failures in gps/ins integrated system: a novel architecture for integrity monitoring", *Journal of Global Positioning Systems*, vol. 8, pp. 26–42, Jun. 2009. DOI: 10.5081/jgps.8.1.26.

[39] M. Joerger and B. Pervan, "Kalman Filter-based Integrity Monitoring Against Sensor Faults", *Journal of Guidance, Control, and Dynamics*, vol. 36, no. 2, 2013.

[40] M. Brenner, "Integrated GPS/Inertial Fault Detection Availability", *NAVIGATION*, vol. 43, no. 2, pp. 111–130, 1996.

[41] R. S. Young and G. A. McGraw, "Fault Detection and Exclusion Using Normalized Solution Separation and Residual Monitoring Methods", *NAVIGATION*, vol. 50, no. 3, pp. 151–169, 2003.

[42] M. Orejas, Z. Kana, J. Dunik, J. Dvorska, and N. Kundak, "Multiconstellation gnss/ins to support lpv200 approaches and autolanding", in *Proceedings of the 25th International Technical Meeting of the Satellite Division of The Institute of Navigation (ION GNSS 2012)*, 2012, pp. 790–803.

[43] J. Diesel and S. Luu, "Gps/irs aime: calculation of thresholds and protection radius using chi-square methods", in *Proceedings of the 8th International Technical Meeting of the Satellite Division of the Institute of Navigation (ION GPS 1995)*, 1995, pp. 1959–1964.

[44] U. I. Bhatti, W. Y. Ochieng, and S. Feng, "Integrity of an integrated GPS/INS system in the presence of slowly growing errors. Part II: analysis", *GPS Solutions*, vol. 11, pp. 183–192, 2007.

[45] M. Brenner, "Implementation of a RAIM Monitor in a GPS Receiver and an Integrated GPS/IRS", *NAVIGATION*, pp. 397–414, Sep. 1990.

[46] K. Vanderwerf, "FDE Using Multiple Integrated GPS/Inertial Kalman Filters in the Presence of Temporally and Spatially Correlated Ionospheric Errors", in *Proceedings of the 14th International Technical Meeting of the Satellite Division of The Institute of Navigation (ION GPS 2001)*, Salt Lake City, UT, Sep. 2001.

[47] S. Hewitson and J. Wang, "Extended Receiver Autonomous Integrity Monitoring (eRAIM) for GNSS/INS integration", *Journal of Surveying Engineering*, vol. 136, no. 1, Feb. 2010.

[48] J. L. Farrel, "Full Integrity Testing for GPS/INS", *Navigation: Journal of the Institute of Navigation*, vol. 53, no. 1, 2006.

[49] R. B. Davies, "Algorithm as 155: the distribution of a linear combination of χ^2 random variables", *Journal of the Royal Statistical Society. Series C (Applied Statistics)*, vol. 29, no. 3, pp. 323–333, 1980, ISSN: 00359254, 14679876. [Online]. Available: http://www.jstor.org/stable/2346911.

[50] M.-S. Circiu, M. Felux, S. Caizzone, *et al.*, "Airborne multipath models for dual-constellation dual-frequency aviation applications", in *ION ITM 2020*, Jan. 2020.

[51] E. Gallon, M. Joerger, and B. Pervan, "Robust modeling of gnss tropospheric delay dynamics", *IEEE Transactions on Aerospace and Electronic Systems*, vol. 57, no. 5, pp. 2992–3003, 2021. DOI: 10.1109/TAES.2021.3068441.

[52] N. El-Sheimy, H. Hou, and X. Niu, "Analysis and modeling of inertial sensors using allan variance", *IEEE Transactions on Instrumentation and Measurement*, vol. 57, no. 1, pp. 140–149, 2008. DOI: 10.1109/TIM.2007.908635.

[53] R. G. Brown and P. Y. Hwang, *Introduction to random signals and applied Kalman filtering, 4th ed.* Wiley New York, 2012, vol. 3.

[54] IEEE, "IEEE standard specification format guide and test procedure for single-axis interferometric fiber optic gyros", Tech. Rep., Feb. 1998, pp. 1–84. DOI: 10.1109/IEEESTD.1998.86153.

[55] A. V. Oppenheim and G. C. Verghese, *Signals, systems and inference*. Pearson, 2015.

[56] D. W. Allan, "Statistics of atomic frequency standards", *Proceedings of the IEEE*, vol. 54, no. 2, pp. 221–230, 1966. DOI: 10.1109/PROC.1966.4634.

[57] C. A. Greenhall, "Spectral ambiguity of allan variance", *IEEE Transactions on Instrumentation and Measurement*, vol. 47, no. 3, pp. 623–627, 1998. DOI: 10.1109/19.744312.

[58] S. Guerrier, J. Skaloud, Y. Stebler, and M.-P. Victoria-Feser, "Wavelet-variance-based estimation for composite stochastic processes", *Journal of the American Statistical Association*, vol. 108, no. 503, pp. 1021–1030, 2013, PMID: 24174689. DOI: 10.1080/01621459.2013.799920. eprint: https://doi.org/10.1080/01621459.2013.799920. [Online]. Available: https://doi.org/10.1080/01621459.2013.799920.

[59] A. T. W. Donald B. Percival, *Wavelet Methods for Time Series Analysis*. Cambridge University Press, 2013.

[60] S. Guerrier, R. Molinari, and J. Skaloud, "Automatic identification and calibration of stochastic parameters in inertial sensors", *NAVIGATION, Journal of The Institute of Navigation*, vol. 62, no. 4, pp. 265–272, 2015. DOI: https://doi.org/10.1002/navi.119.

[61] Y. Stebler, S. Guerrier, J. Skaloud, and M.-P. Victoria-Feser, "Generalized method of wavelet moments for inertial navigation filter design", *IEEE Transactions on Aerospace and Electronic Systems*, vol. 50, no. 3, pp. 2269–2283, 2014. DOI: 10.1109/TAES.2014.120751.

[62] S. Khanafseh, S. Langel, and B. Pervan, "Overbounding position errors in the presence of carrier phase multipath error model uncertainty", in *Proceedings of IEEE/ION PLANS 2010*, 2010, pp. 575–584.

[63] B. Decleene, "Defining Pseudorange Integrity - Overbounding", in *Proceedings of the Institute of Navigation's ION-GPS 2000*, Jun. 2000, pp. 1916–1924.

[64] J. Lee, S. Pullen, and P. Enge, "Sigma overbounding using a position domain method for the local area augmentaion of gps", *IEEE Transactions on Aerospace and Electronic Systems*, vol. 45, no. 4, pp. 1262–1274, 2009.

[65] J. Rife and B. Pervan, "Overbounding revisited: discrete error-distribution modeling for safety-critical gps navigation", *IEEE Transactions on Aerospace and Electronic Systems*, vol. 48, no. 2, pp. 1537–1551, 2012.

[66] J. Rife, S. Pullen, P. Enge, and B. Pervan, "Paired overbounding for nonideal laas and waas error distributions", *IEEE Transactions on Aerospace and Electronic Systems*, vol. 42, no. 4, pp. 1386–1395, 2006.

[67] J. Blanch, T. Walter, and P. Enge, "Gaussian bounds of sample distributions for integrity analysis", *IEEE Transactions on Aerospace and Electronic Systems*, vol. 55, no. 4, pp. 1806–1815, 2019.

[68] M.-S. Circiu, "Integrity aspects for dual-frequency dual-constellation ground based augmentation system (GBAS)", Veröffentlicht auf dem Publikationsserver der RWTH Aachen University; Dissertation, Rheinisch-Westfälische Technische Hochschule Aachen, 2020, Dissertation, Rheinisch-Westfälische Technische Hochschule Aachen, Aachen, 2020, 1 Online–Ressource (xxviii, 252 Seiten) : Illustrationen, Diagramme. DOI: 10.18154/RWTH-2020-07268. [Online]. Available: https://publications.rwth-aachen.de/record/793914.

[69] J. Rife and D. Gebre-Egziabher, "Symmetric overbounding of correlated errors", *NAVIGATION*, vol. 54, no. 2, pp. 109–124, 2007. DOI: 10.1002/j.2161-4296.2007.tb00398.x.

[70] G. W. Pulford, "A Proof of the Spherically Symmetric Overbounding Theorem for Linear Systems", *Journal of the Institute of Navigation*, vol. 55, no. 4, pp. 283–292, 2008.

[71] Z. Xing and D. Gebre-Egziabher, "Paired Overbounding and Applications to GPS Augmentation", in *Proceedings of the IEEE/ION Position, Location and Navigation Symposium (PLANS) 2004*, May 2008.

[72] C. Amielh, A. Chabory, C. Macabiau, and L. Azoulai, "Gnss multipath error model for aircraft surface navigation based on canonical scenarios for class f airports", in *Proceedings of the 32nd International Technical Meeting of the Satellite Division of The Institute of Navigation (ION GNSS+ 2019)*, 2019, pp. 1418–1437.

[73] S. Langel, O. García Crespillo, and M. Joerger, "Overbounding the effect of uncertain gauss-markov noise in kalman filtering", *NAVIGATION*, vol. 68, no. 2, pp. 259–276, 2021. DOI: https://doi.org/10.1002/navi.419. eprint: https://onlinelibrary.wiley.com/doi/pdf/10.1002/navi.419. [Online]. Available: https://onlinelibrary.wiley.com/doi/abs/10.1002/navi.419.

[74] M. Anderson, N. Zhou, J. Pierre, and R. Wies, "Bootstrap-based confidence interval estimates for electromechanical modes from multiple output analysis of measured ambient data", *IEEE Transactions on Power Systems*, vol. 20, no. 2, pp. 943–950, 2005. DOI: 10.1109/TPWRS.2005.846125.

[75] L. Galleani, "The dynamic allan variance iii: confidence and detection surfaces", *IEEE Transactions on Ultrasonics, Ferroelectrics, and Frequency Control*, vol. 58, no. 8, pp. 1550–1558, 2011.

[76] J. Balamuta, R. Molinari, S. Guerrier, and J. Skaloud, "A computationally efficient platform for inertial sensor calibration", in *ION GNSS+*, Sep. 2015. [Online]. Available: https://www.ion.org/publications/abstract.cfm?articleID=12867.

[77] S. K. Jada and M. Joerger, "Gmp-overbound parameter determination for measurement error time correlation modeling", in *The International Technical Meeting of the The Institute of Navigation*, 2020.

[78] D. Racelis, S. Jada, and M. Joerger, "Sequential araim evaluation using time-domain versus frequency-domain error-correlation bounding methods", in *Proceedings of the 34th International Technical Meeting of the Satellite Division of The Institute of Navigation (ION GNSS+ 2021)*, 2021, pp. 1079–1091.

[79] S. Langel, "Bounding estimation integrity risk for linear systems with structured stochastic modeling uncertainty", Ph.D. dissertation, Illinois Institute of Technology, 2014.

[80] S. E. Langel, S. M. Khanafseh, and B. S. Pervan, "Bounding integrity risk for sequential state estimators with stochastic modeling uncertainty", *Journal of Guidance, Control, and Dynamics*, vol. 37, no. 1, pp. 36–46, 2014. DOI: 10.2514/1.62056. eprint: https://doi.org/10.2514/1.62056. [Online]. Available: https://doi.org/10.2514/1.62056.

[81] S. Langel, M. Joerger, S. Khanafseh, and B. Pervan, "Practical approach for kalman filtering with autocorrelated noise containing uncertain parameters", *Journal of Guidance, Control, and Dynamics*, vol. 43, no. 8, pp. 1550–1555, 2020.

[82] Lihua Xie, Yeng Chai Soh, and C. E. de Souza, "Robust kalman filtering for uncertain discrete-time systems", *IEEE Transactions on Automatic Control*, vol. 39, no. 6, pp. 1310–1314, 1994.

[83] I. R. Petersen and D. C. McFarlane, "Optimal guaranteed cost control and filtering for uncertain linear systems", *IEEE Transactions on Automatic Control*, vol. 39, no. 9, pp. 1971–1977, 1994.

[84] V. A. Tupysev, O. A. Stepanov, A. V. Loparev, and Y. A. Litvinenko, "Guaranteed estimation in the problems of navigation information processing", in *2009 IEEE Control Applications, (CCA) Intelligent Control, (ISIC)*, Jul. 2009, pp. 1672–1677. DOI: 10.1109/CCA.2009.5281081.

[85] E. Gallon, M. Joerger, S. Perea, and B. Pervan, "Error model development for araim exploiting satellite motion", in *Proceedings of the 32nd International Technical Meeting of the Satellite Division of The Institute of Navigation (ION GNSS+ 2019)*, Sep. 2019.

[86] M. G. Petovello, K. O'Keefe, G. Lachapelle, and M. E. Cannon, "Consideration of time-correlated errors in a kalman filter applicable to gnss", *Journal of Geodesy*, vol. 83, no. 1, pp. 51–56, 2009.

[87] B. P. Gibbs, *Advanced Kalman filtering, least-squares and modeling: a practical handbook*. John Wiley & Sons, 2011.

[88] S. Khanafseh, N. Roshan, S. Langel, F.-C. Chan, M. Joerger, and B. Pervan, "Gps spoofing detection using raim with ins coupling", in *2014 IEEE/ION Position, Location and Navigation Symposium - PLANS 2014*, 2014, pp. 1232–1239. DOI: 10.1109/PLANS.2014.6851498.

[89] D. Rouzaud and J. Skaloud, "Rigorous integration of inertial navigation with optical sensors by dynamic networks", *Navigation*, vol. 58, no. 2, pp. 141–152, 2011.

[90] D. A. Cucci, M. Rehak, and J. Skaloud, "Bundle adjustment with raw inertial observations in uav applications", *ISPRS Journal of Photogrammetry and Remote Sensing*, vol. 130, pp. 1–12, 2017, ISSN: 0924-2716. DOI: https://doi.org/10.1016/j.isprsjprs.2017.05.008. [Online]. Available: https://www.sciencedirect.com/science/article/pii/S0924271617301387.

[91] W. Wen, T. Pfeifer, X. Bai, and L.-T. Hsu, "Factor graph optimization for GNSS/INS integration: A comparison with the extended kalman filter", *NAVIGATION, Journal of the Institute of Navigation*, vol. 68, no. 2, pp. 315–331, 2021.

[92] K. Wang, Y. Li, and C. Rizos, "Practical approaches to kalman filtering with time-correlated measurement errors", *IEEE Transactions on Aerospace and Electronic Systems*, vol. 48, no. 2, pp. 1669–1681, Apr. 2012, ISSN: 2371-9877. DOI: 10.1109/TAES.2012.6178086.

[93] S. F. Schmidt, "Application of state-space methods to navigation problems", in *Advances in control systems*, vol. 3, Elsevier, 1966, pp. 293–340.

[94] A. Bryson Jr and L. Henrikson, "Estimation using sampled data containing sequentially correlated noise.", *Journal of Spacecraft and Rockets*, vol. 5, no. 6, pp. 662–665, 1968.

[95] C. B. Mehr and J. McFadden, "Certain properties of gaussian processes and their first-passage times", *Journal of the Royal Statistical Society: Series B (Methodological)*, vol. 27, no. 3, pp. 505–522, 1965.

[96] K. O'Keefe, M. Petovello, G. Lachapelle, and M. E. Cannon, "Assessing probability of correct ambiguity resolution in the presence of time-correlated errors", *NAVIGATION, Journal of the Institute of Navigation*, vol. 53, no. 4, pp. 269–282, 2006.

[97] P. Clausen, J. Skaloud, S. Orso, and S. Guerrier, "Construction of dynamically-dependent stochastic error models", in *2018 IEEE/ION Position, Location and Navigation Symposium (PLANS)*, 2018.

[98] D. Gebre-Egziabher, "Design and performance analysis of a low-cost aided dead reckoning navigator", Ph.D. dissertation, stanford university, 2002.

[99] S. Langel, O. García Crespillo, and M. Joerger, "A New Approach for Modeling Correlated Gaussian Errors using Frequency Domain Overbounding", in *Position, Navigation and Timing Symposium (PLANS)*, May 2020.

[100] S. Langel, O. García Crespillo, and M. Joerger, "Bounding Sequential Estimation Errors due to Gauss-Markov Noise with Uncertain Parameters", in *Proceedings of the 32nd International Technical Meeting of the Satellite Division of The Institute of Navigation (ION GNSS+ 2019)*, Sep. 2019.

[101] N. J. Kasdin, "Discrete simulation of colored noise and stochastic processes and 1/f/sup /spl alpha// power law noise generation", *Proceedings of the IEEE*, vol. 83, no. 5, pp. 802–827, 1995.

[102] M. Joerger and B. Pervan, "Exploiting satellite motion in araim: measurement error model refinement using experimental data", in *Proceedings of the 29th International Technical Meeting of The Satellite Division of the Institute of Navigation (ION GNSS+ 2016)*, Sep. 2016.

[103] M. Joerger and B. Pervan, "Multi-constellation ARAIM Exploiting Satellite Motion", English (US), *Navigation, Journal of the Institute of Navigation*, Jan. 2020.

[104] RTCA/DO-245A, "Minimum Aviation System Performance Standards for the Local Area Augmentation System (LAAS)", Radio Technical Commission for Aeronautics, Tech. Rep. 245A, 2004.

[105] O. García Crespillo, M. Joerger, and S. Langel, "Overbounding GNSS/INS integration with uncertain GNSS Gauss-Markov error parameters", in *Position, Navigation and Timing Symposium (PLANS)*, May 2020.

[106] O. García Crespillo, A. Grosch, and M. Meurer, "Detection of DME Ranging Faults with INS Coupling", in *2017 Integrated Communication, Navigation and Surveillance Conference (ICNS)*, 2017.

[107] R. S. Y. YOUNG and G. A. MCGRAW, "Fault detection and exclusion using normalized solution separation and residual monitoring methods", *NAVIGATION*, vol. 50, no. 3, pp. 151–169, 2003. DOI: https://doi.org/10.1002/j.2161-4296.2003.tb00326.x. eprint: https://onlinelibrary.wiley.com/doi/pdf/10.1002/j.2161-4296.2003.tb00326.x. [Online]. Available: https://onlinelibrary.wiley.com/doi/abs/10.1002/j.2161-4296.2003.tb00326.x.

[108] S. Thoelert, M. Vergara, M. Sgammini, *et al.*, "Characterization of nominal signal distortions and impact on receiver performance for gps (iif) l1/l5 and galileo (iov) e1/e5a signals", in *Proceedings of the 27th International Technical Meeting of the Satellite Division of The Institute of Navigation (ION GNSS+ 2014)*, 2014.

[109] Stanford University GPS Lab, *Matlab algorithm availability simulation tool for araim*, https://gps.stanford.edu/resources/software-tools/maast, Version 0.4.

[110] P. Abel and O. Garcia Crespillo, "Multisensor navigation simulator documentation", German Aerospace Center (DLR), Tech. Rep., 2016.

[111] I. C. A. O. (ICAO), "DOC 8168: procedures for air navigation services - aircraft operations (pans-ops)", ICAO, Tech. Rep., 2006.

[112] W. G. C, "Wg-c advanced raim technical subgroup reference airborne algorithm description document", Tech. Rep., 2019, Version 3.1.

[113] Y. Zhai, M. Joerger, and B. Pervan, "Continuity and availability in dual-frequency multi-constellation araim", in *Proceedings of the 28th International Technical Meeting of the Satellite Division of The Institute of Navigation (ION GNSS+ 2015)*, 2015, pp. 664–674.

[114] M. Joerger, D. Racelis, J. Blanch, and B. Pervan, "Continuity and availability evaluation in horizontal araim", in *Proceedings of the 34th International Technical Meeting of the Satellite Division of The Institute of Navigation (ION GNSS+ 2021)*, 2021, pp. 278–289.

[115] *Ourairports*, https://ourairports.com/data/.

[116] S. Langel, O. García Crespillo, and M. Joerger, "Overbounding sequential estimation errors due to non-Gaussian correlated noise", in *Proceedings of the 33rd International Technical Meeting of the Satellite Division of The Institute of Navigation (ION GNSS+ 2020)*, 2020.

[117] O. Garcia Crespillo, M. Joerger, and S. Langel, "Tight bounds for uncertain time-correlated errors with gauss-markov structure", *arXiv*, 2020. arXiv: 2009.09495 [eess.SP].

[118] J. Cadzow and Y. Sun, "Sequences with positive semidefinite fourier transforms", *IEEE Transactions on Acoustics, Speech, and Signal Processing*, vol. 34, no. 6, pp. 1502–1510, 1986. DOI: 10.1109/TASSP.1986.1164990.

[119] O. G. Crespillo, S. Langel, and M. Joerger, "Tight bounds for uncertain time-correlated errors with gauss-markov structure in kalman filtering".

[120] O. García Crespillo, D. Medina, J. Skaloud, and M. Meurer, "Tightly coupled GNSS/INS Integration based on Robust M-estimators", in *2018 IEEE/ION Position, Location and Navigation Symposium (PLANS)*, Monterey, CA: IEEE, Apr. 2018, pp. 1554–1561. (visited on 08/26/2019).

[121] O. García Crespillo, D. Medina, J. Skaloud, and M. Meurer, "Tightly coupled GNSS/INS Integration based on Robust M-estimators", *GPS World*, vol. 28, no. 8, 2017.